Czech Technical University in Prague
Faculty of Nuclear Sciences and Physical Engineering

Department of Physics

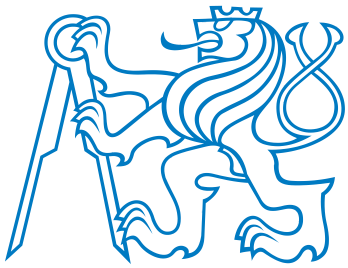

DOCTORAL THESIS

Study of b-quark Processes Using the ATLAS Detector

Prague, 2020

Ing. Radek Novotný

České vysoké učení technické v Praze

Fakulta jaderná a fyzikálně inženýrská

Katedra fyziky

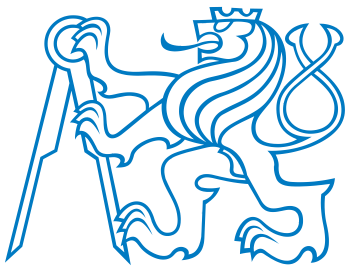

DISERTAČNÍ PRÁCE

Studium procesů s produkcí b-kvarků na experimentu ATLAS

Praha, 2020

Ing. Radek Novotný

Bibliographic Entry

Author	Ing. Radek Novotný Czech Technical University in Prague Faculty of Nuclear Sciences and Physical Engineering Department of Physics
Title	Study of b-quark Processes Using the ATLAS Detector
Degree Programme	Application of Natural Sciences
Field of study	Nuclear Engineering
Supervisor	prom. fyz. Václav Vrba, CSc. Czech Technical University in Prague Faculty of Nuclear Sciences and Physical Engineering Department of Physics
Supervisor specialist	Ing. Michal Marčišovský, Ph.D. Institute of Physics of the Czech Academy of Sciences
Academic Year	2019/2020
Number of Pages	161
Keywords	CP-violation, lifetime measurement, B-Physics, ATLAS, LHC

Bibliografický záznam

Autor	Ing. Radek Novotný České vysoké učení technické v Praze Fakulta jaderná a fyzikálně inženýrská Katedra fyziky
Název práce	Studium procesů s produkcí b-kvarků na experimentu ATLAS
Studijní program	Aplikace přírodních věd
Studijní obor	Jaderné inženýrství
Školitel	prom. fyz. Václav Vrba, CSc. České vysoké učení technické v Praze Fakulta jaderná a fyzikálně inženýrská Katedra fyziky
Školitel specialista	Ing. Michal Marčišovský, Ph.D. Fyzikální ústav AVČR, v.v.i.
Akademický rok	2019/2020
Počet stran	161
Klíčová slova	CP narušení, měření doby života, B-Fyzika, ATLAS, LHC

Abstract

This thesis focuses on three topics related to the CP-violation measurement in the $B_s^0 \to J/\psi(\mu^+\mu^-)\phi(K^+K^-)$ channel made by the B-Physics working group at the ATLAS experiment.

The first analysis is a measurement of the CP-violation phase ϕ_s in the $B_s^0 \to J/\psi\phi$ channel. This analysis was performed on the pp collisions at centre-of-mass energy $\sqrt{s} = 13\,\text{TeV}$ collected by the ATLAS experiment with integrated luminosity of $80.5\,\text{fb}^{-1}$. The obtained results are statistically combined with the previous ATLAS measurements at centre-of-mass energy 7 TeV and 8 TeV. The observed values of the most important CP-violation parameters are:

$$\begin{aligned}
\phi_s &= -0.087 \pm 0.037\,(\text{stat.}) \pm 0.019\,(\text{syst.})\,\text{rad} \\
\Delta\Gamma_s &= 0.064 \pm 0.004\,(\text{stat.}) \pm 0.002\,(\text{syst.})\,\text{ps}^{-1} \\
\Gamma_s &= 0.670 \pm 0.001\,(\text{stat.}) \pm 0.002\,(\text{syst.})\,\text{ps}^{-1}
\end{aligned}$$

All measurements agree with the Standard Model predictions.

The second analysis is a measurement of $B^\pm \to J/\psi K^\pm$ and $B_d^0 \to J/\psi K^{*0}$ lifetimes. This analysis serves as a benchmark measurement to validate the precision of the lifetime corrections applied on the B_s^0 events and the performance of the B-Physics triggers.

The last analysis is devoted to the search for a structure in the $B_s^0\pi^\pm$ invariant mass spectrum particularly the search for the resonance $X(5568)$ which is tetra-quark candidate. The upper limit on the number of signal events $N(X)$ and on its production rate relative to B_s^0 mesons ρ_X were measured since no statistically significant signal was observed. The measured limits are $N(X) < 382$ and $\rho_X < 0.015$ for $p_\text{T}(B_s^0) > 10\,\text{GeV}$ and $N(X) < 356$ and $\rho_X < 0.016$ for $p_\text{T}(B_s^0) > 15\,\text{GeV}$. The ATLAS result is consistent with the results from other LHC experiments.

Abstrakt

Tato dizertační práce je věnována třem analýzám jenž jsou blízké měření CP narušení v rozpadovém kanále $B_s^0 \to J/\psi(\mu^+\mu^-)\phi(K^+K^-)$ provedené B-Fyzikální skupinou experimentu ATLAS.

První analýza je věnována měření fáze CP narušení ϕ_s v rozpadovém kanále $B_s^0 \to J/\psi\phi$. Tato analýza byla provedena na pp srážkách s těžišťovou energií $\sqrt{s} = 13\,\text{TeV}$ měřených za pomocí detektoru ATLAS. Celková integrovaná luminozita datového vzorku je $80.5\,\text{fb}^{-1}$. Naměřené výsledky byly statisticky zkombinované s předešlým měřením experimentu ATLAS těžišťovou energií 7 TeV a 8 TeV. Naměřené hodnoty nejdůležitějších parametrů popisující CP narušení jsou:

$$\begin{aligned}
\phi_s &= -0.087 \pm 0.037\,(\text{stat.}) \pm 0.019\,(\text{syst.})\,\text{rad} \\
\Delta\Gamma_s &= 0.064 \pm 0.004\,(\text{stat.}) \pm 0.002\,(\text{syst.})\,\text{ps}^{-1} \\
\Gamma_s &= 0.670 \pm 0.001\,(\text{stat.}) \pm 0.002\,(\text{syst.})\,\text{ps}^{-1}
\end{aligned}$$

Všechny naměřené hodnoty jsou v souladu s teoretickou předpovědí Standardního modelu.

Druhou analýzou je měření doby života částic $B^\pm \to J/\psi K^\pm$ a $B_d^0 \to J/\psi K^{*0}$. Toto měření slouží pro ověření korekcí na dobu života použitých v analýze B_s^0 kandidátů a také pro určení kvality B-Fyzikálních triggerů.

Poslední analýzou je hledání struktury ve spektru invariantní hmoty $B_s^0\pi^\pm$ kandidátů konkrétně hledání rezonance $X(5568)$ jenž je kandidátem na první objevený tetra-kvark. Protože nebyl objeven statisticky významný signál, bylo provedeno měření horních limitů počtu kandidátů $N(X)$ a také relativní produkční poměr k B_s^0 mezonům ρ_X. Naměřené limity jsou $N(X) < 382$ a $\rho_X < 0.015$ pro $p_\text{T}(B_s^0) > 10\,\text{GeV}$ a $N(X) < 356$ a $\rho_X < 0.016$ pro $p_\text{T}(B_s^0) > 15\,\text{GeV}$. Výsledky naměřené na experimentu ATLAS jsou konzistentní s ostatními výsledky experimentů na urychlovači LHC.

Acknowledgment

Foremost, I would like to thank my supervisor Václav Vrba for the overall support of my work and that he provided me the opportunity to participate in this exciting research. I would also like to thank Michal Marčišovský for his professional guidance, willingness, and invaluable advice.

Furthermore, I would like to thank Mária Smižanská for the leadership of our analysis group, professional guidance and for pushing the analysis always forward.The great thanks belong to all members of the analysis team especially Adam Barton, James Walder, Pavel Řezníček, Andrew Wharton, Tomáš Jakoubek and Lukáš Novotný for their patience solving the problems that came across and for technical leadership and guidance.

The great thanks belong Maria Marčišovská for her carefully reading of the manuscript. I am also grateful to my CTU colleagues and friends for their academic support and to be a great group with which I spent wonderful years at the university. My greatest gratitude belongs to my family and friends for the continuous support they have given me during my studies.

Last but not least I would like to thank Kristýna Vračková for supporting me during my journey and to our son Čestmír for his smile that makes every day special.

Declaration

I hereby declare that this thesis is the result of my own work and all the sources I used are in the list of references.

I have no objection to usage of this work in compliance with the act §60 Law No. 121/2000 Coll. (Copyright Act), and with the rights connected with the copyright act including the changes in the act.

In Prague, 2020 Ing. Radek Novotný

Contents

CHAPTER 1

Introduction

The Standard Model of particle physics is currently the most successful theory describing fundamental interactions in the field of particle physics. It was well tested by many experiments during past decades; however, there are still several aspects missing that are not well covered by the SM theory. These include the large dominance of matter over antimatter in the universe, the existence of the dark matter or the quantum description of the gravitational force. Some of the aspects of the SM theory and the theories beyond the SM can be studied at the Large Hadron Collider (LHC) at CERN near Geneva [1].

The LHC has already finished its second period of data taking called Run 2, where over 139 fb^{-1} of proton-proton collisions at the centre-of-mass energy of $\sqrt{s} = 13\,\text{TeV}$ was delivered to the experiments. The largest of the experiments at the LHC is the ATLAS experiment [2]. The ATLAS detector is a multi-purpose detector designed primarily for high p_{T} physics. It has already proven its quality by observing the Higgs boson [3]. Even though this discovery of the Higgs boson is the best known result, ATLAS collaboration has an extensive scientific program studying fundamental properties of the Standard Model as well as searches for Beyond Standard Model physics, supersymetry or dark matter.

The B-Physics working group is one of several working groups at ATLAS experiment which focuses on the study of b and c physics of heavy quarkonia, and the physics of light mass states. The main range of operation of B-Physics is low p_{T} region, which is on the edge of the ATLAS kinematic acceptance region. This kinematic region brings many challenges for the ATLAS trigger system, event reconstruction framework and for the final physics analysis as well.

The primary objective of this doctoral thesis is to present the latest results of the CP-violation measurement in the $B_s^0 \to J/\psi(\mu^+\mu^-)\phi(K^+K^-)$ channel using data collected by the ATLAS detector at 13 TeV of pp collisions at the LHC with integrated luminosity

of $80.5\,\mathrm{fb}^{-1}$. The measured parameters include the CP-violating phase ϕ_s and the width difference $\Delta\Gamma_s$ between the B_s^0 meson mass eigenstates, which can be compared with the Standard Model prediction and other LHC experiments. Furthermore, the simpler benchmark analysis, such as lifetime measurement in the $B^\pm \to J/\psi K^\pm$ and $B_d \to J/\psi K^*$ channels, or search for a structure in the $B_s^0\pi^\pm$ invariant mass spectrum are presented to provide the insight to the trigger monitoring and validation processes in the B-Physics working group.

The following two chapters of this thesis give a short overview of the physics theories describing the CP-violation in $B_s^0 \to J/\psi(\mu^+\mu^-)\phi(K^+K^-)$ channel, Standard Model of particle interactions and decays of neutral B-mesons. Chapter four is devoted to the description of Large Hadron Collider, its parameters and performance. Chapter five introduces the ATLAS detector hardware and its detector sub-systems, while the ATLAS software and computing tools are described in chapter six. The general overview of the ATLAS B-Physics working group is given in chapter seven.

The eighth chapter describes the measurement of CP-violation parameters in the $B_s^0 \to J/\psi(\mu^+\mu^-)\phi(K^+K^-)$ channel, the candidate reconstruction and selection, the maximum-likelihood method, the flavour tagging, discussion of physics results and their combination with previous ATLAS measurements. The author of this thesis contributed significantly to the estimation of the lifetime corrections, to the measurement of conditional probability distributions, to the toy Monte Carlo method and to the main fitting procedure adapted from previous ATLAS measurements. The author was also responsible for the estimation of corresponding systematic effects related to these contributions.

The ninth chapter focuses on the lifetime measurement in the $B^\pm \to J/\psi K^\pm$ and $B_d \to J/\psi K^*$ channels, which are used for the trigger and lifetime error validation. The author developed the procedure of simultaneous mass-lifetime fits based on the framework used in the B-Physics working group for the trigger validation in Run 1. This framework was further improved for the precise lifetime measurement.

Chapter ten is devoted to the search for a structure in the $B_s^0\pi^\pm$ invariant mass spectrum. Since there is no statistically significant evidence for a structure in the spectrum, this measurement was used as a benchmark analysis for the LHC experiments to measure the sensitivity for such resonance. The authors contribution to this analysis was the development of the fitting procedure to extract the invariant mass spectrum, to develop the code for estimation of the upper limits and the systematic uncertainties estimation.

Chapter eleven summarizes all measured results and concludes the thesis.

CHAPTER 2

Theoretical Background

2.1 Standard Model

Particle physics is dealing with particles that are the constituents of what is usually referred to as matter and radiation. Many models were created to describe well known phenomena and physical laws. In the 1970s, the Standard Model (SM) of particles and their interactions was formed. This model is in the best agreement with experimental data. The SM assumes, that our world is made of 17 elementary particles and their corresponding antiparticles. The first group is called fermions and it has a half-integer spin. The second group is bosons and particles contained in it have integral spin. The particles interact via four known types of forces: electromagnetic, strong, weak and gravitational, of which the latter is not a part of the SM.

One of the current challenges in the particle physics is to improve the precision of the measured properties of known processes and particles to study any discrepancies between the measurements and the SM. Any significant deviation from the SM would imply existence of the processes that are not described by the SM and these physics phenomena are called Beyond Standard Model (BSM) physics. The measurement of neutrino mass suggested that the SM is incomplete, because according to theory neutrinos should be massless.

The complete list of elementary particles contained in the SM and some of their properties is shown in Figure 2.1.

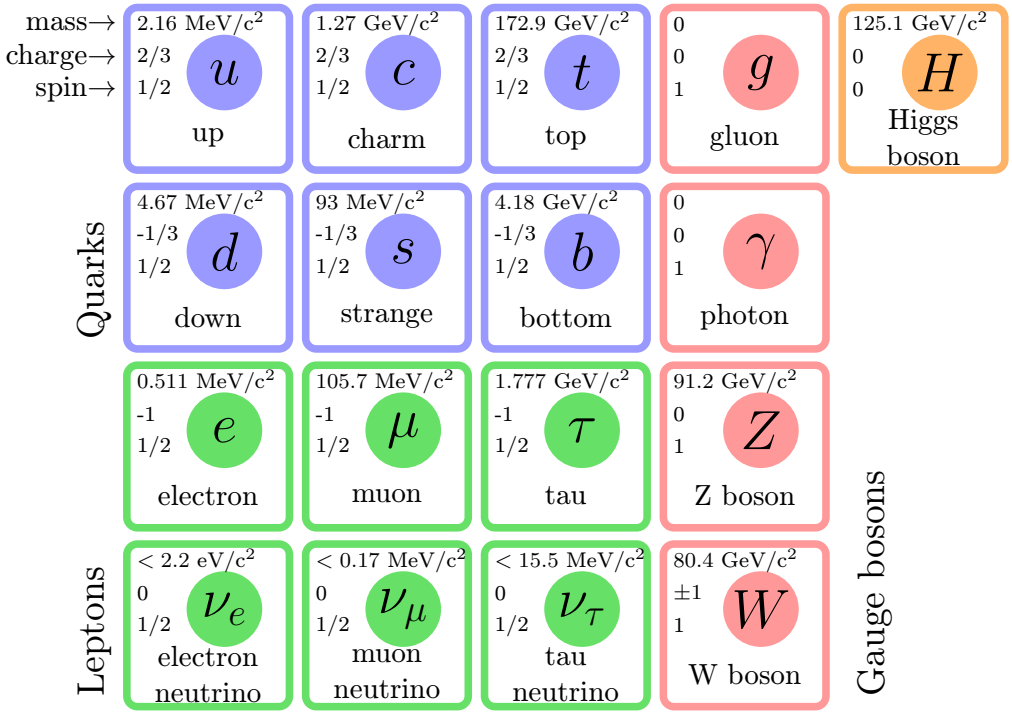

Figure 2.1: The list of particles in the Standard Model. The invariant mass, electric charge and spin is shown [4].

2.1.1 Fundamental Interactions

Interactions in the SM are realized as an exchange of mediating bosons, characteristic to the type of interaction between its constituents. The exchange particle transfers momentum and energy between the two objects, and are in effect mediating the interaction. Due to their character, they are frequently called exchange interactions.

Electromagnetic interaction acts between particles with non-zero electric charge and is mediated by a massless photon (γ). Electromagnetic interaction has an infinite range; however, the potential decreases with distance $\sim r^{-1}$. The theory describing the electromagnetic interaction is called quantum electrodynamics (QED) [5], which later laid the ground for the quantum field theory (QFT) [6], the framework which descriebs the rest of interactions in the SM.

Strong interaction binds quarks together in hadrons and is mediated by the exchange of massless gluons. Strong force is the strongest force compared to other forces; however, its range is limited to $\approx 1\,\text{fm}$. The theory describing strong interaction is called Quantum Chromodynamics (QCD) and will be described in section 2.4 in more detail.

Weak interaction account for large variety of physical processes: muon and tau decays, neutrino interactions, decays of lightest meson it is responsible for the relatively slow processes of β decay and is able to describe the quark mixing and CP-violation.. The mediators of this interaction are massive $W^{\pm}$ and Z^0 bosons. It is characterized by long lifetimes, extremely small distance and small cross-sections. The detailed description of weak interaction is given in section 2.3.

Gravitational interaction acts between all particles. Gravitational force is the weakest of all fundamental forces, and it is almost 10^{-38} times weaker than strong interaction. Due to this fact, gravitational interaction is neglected in the SM. In some particle theories, this interaction is mediated by a hypothetical graviton particle with spin 2.

2.1.2 Quarks

In the SM, quarks are structureless strongly interacting fermions with spin 1/2. The quark model was introduced by Murray Gell-Mann [7] and George Zweig [8] in early 1960s when they were trying to develop classification scheme for known hadrons. They independently postulated the existence of particles with fractional charge that are structural elements or other particles. At that time they thought that there exist only three quarks named: up (u), down (d) and strange (s). If we take the three quarks with nearly equivalent mass they can be represented by the $SU(3)$ symmetry and the antiquarks can be described by the complex conjugate representation $SU(\bar{3})$.

The combination of $SU(3)$ group elements lead to following two groups of particles:

Mesons are made by combining quark q and antiquark $\bar{q}$ in such way that

$$3 \otimes \bar{3} = 8 \oplus 1 \tag{2.1}$$

Baryons consist of three constituent quarks q.

$$3 \otimes 3 \otimes 3 = 10 \oplus 8 \oplus 8 \oplus 1 \tag{2.2}$$

After discovery of c and b quarks, additional quantum numbers (charm and beauty) were assigned to baryons which carry these quarks. Later was discovered the currently heaviest quark t named top. The first three quarks are referred to as light quarks q and the other three quarks are referred to as heavy quarks Q. All of the quarks, except top quark, bind to create hadrons. Because the mass of top quark is too large, it decays faster than it hadronizes and thus it can not be seen in any bound state. The fundamental properties of six quarks, grouped in three generations, can be seen in Figure 2.1.

2.1.3 Leptons

At present, six leptons are known, which are, similarly to quarks, categorized into three generations. There are three charged leptons and for each of them there is an electrically neutral neutrino. The masses (or upper mass limits) of leptons are given in Figure 2.1.

Neutrinos are specific with masses very small in comparison to their corresponding charged leptons. Although the neutrinos have mass, in the SM they are assumed to be massless. Another unique quality of neutrinos is that only negative projection of total angular momentum onto z axis was observed. This corresponds to a pure helicity * state $H = -1$ (left-handed). The latest measurement of the Planck experiment [10] provides the upper limit for the sum of neutrino masses m_{ν_i}

$$\sum_i m_{\nu_i} < 0.25 \text{ eV}. \tag{2.3}$$

The measurement of neutrino masses is based on the phenomenon called neutrino oscillation, where neutrinos with one flavour can convert to neutrinos of a different flavour. This process can not proceed with zero mass of the neutrino. Although the neutrino oscillation was predicted in 1957 by Bruno Pontecorvo [11], the first experimental observation was made in 1998 at SuperKamiokande detector [12].

2.1.4 Antiparticles

For every particle, there is a corresponding antiparticle with identical mass and lifetime, but with the opposite charge and magnetic moment.

The existence of antiparticles is a general property of both fermions and bosons. The first observed antiparticle was the antiparticle of an electron, which is referred to as positron. Due to the conservation laws, fermions must be created and destroyed in pairs. This mechanism is called pair-production and annihilation.

2.2 Symmetries and CPT Theorem

Symmetries and conservation laws play fundamental role in physics. The invariance of a system under a continuous symmetry transformation leads to a conservation law as described by Noether's theorem [13]. Besides these continuous symmetries, there exist discrete symmetries that play a very important role as well. In the particle physics following three discrete symmetries are a topic of high interest:

*Helicity is the projection of the spin $\vec{S}$ onto the direction of momentum $\vec{p}$ [9].

Charge conjugation, $\mathcal{C}$: transforms a particle into its antiparticle and vice versa by changing sign of all intrinsic charges. The motion and spin are left unchanged.

Parity inversion, $\mathcal{P}$: this transformation inverts all spatial coordinates by reflection through the origin ($\vec{r} \to -\vec{r}$). This transformation changes momentum sign but the spin is unaffected.

Time reversal, $\mathcal{T}$: changes time coordinate sign ($t \to -t$). This lead to change of sign of momentum and velocity as well as spin.

The QED as well as QCD are invariant under the $\mathcal{C}$ and $\mathcal{P}$ transformations; however, weak interaction violate both symmetries. It was long thought that composite $\mathcal{CP}$ symmetry is conserved in the electroweak sector, but the observation of decays of neutral kaons by James Cronin and Val Fitch in 1964 disprove this theory/prediction [14]. At present, only the CPT theorem, predicting invariance of all forces under the combination of $\mathcal{C}$, $\mathcal{P}$ and $\mathcal{T}$ transformations, seems to be valid.

2.3 Weak Interaction

The weak and the electromagnetic interaction in the SM are jointly described by the Glashow-Weinberg-Salam [15] theory of electroweak (EW) interactions based on $SU(2)_L \times U(1)_Y$ gauge symmetry. This interaction is mediated by gauge bosons $W^{\pm}$ and Z^0 for weak part and γ for the electromagnetic part. Since explicit mass terms in the Lagrangian would break gauge invariance, the mass terms of elementary particles in the SM are generated by spontaneous symmetry breaking of the electroweak sector proposed by the Peter Higgs [16] and François Englert [17], this phenomena is also called Higgs mechanism. Additionally, the scalar particle arising from the Higgs mechanism, the Higgs boson, unitarizes the electroweak gauge boson scattering at high energies. The Higgs sector furthermore allows the introduction of fermion masses into the SM by means of Yukawa interactions between the fermion fields and the scalar Higgs field in the ground state. Since these interactions give rise to the mixing of the three quark generations, parametrized in the CKM matrix, they introduce direct CP-violation into the SM.

2.3.1 CP-Violation

The CP-violation stands for the processes where the combined conservation laws associated with $\mathcal{C}$ and $\mathcal{P}$ are broken. The phenomenology of CP-violation for neutral flavoured mesons is particularly interesting, since many of the observables can be cleanly interpreted. In this section, the general formalism for and classification of CP-violation of

weakly decaying meson M is presented.

The first type of CP-violation is observed in the measurement of decay amplitudes for the processes $M \to f$ and $\bar{M} \to \bar{f}$. Experimentally, it manifests as the difference in the decay widths of the two charge conjugated states.

$$A_{CP} = \frac{\Gamma(M \to f) - \Gamma(\bar{M} \to \bar{f})}{\Gamma(M \to f) + \Gamma(\bar{M} \to \bar{f})} \tag{2.4}$$

If we find them different we establish **direct CP-violation** often called **CP-violation in decay**.

However, in decays to a common final state $M \to f$ and $\bar{M} \to f$ the meson anti-meson mixing occurs and the meson state is represented as a superposition of two mass eigenstates. The meson anti-meson mixing occurs mainly through box diagrams which is shown in the Figure 2.2.

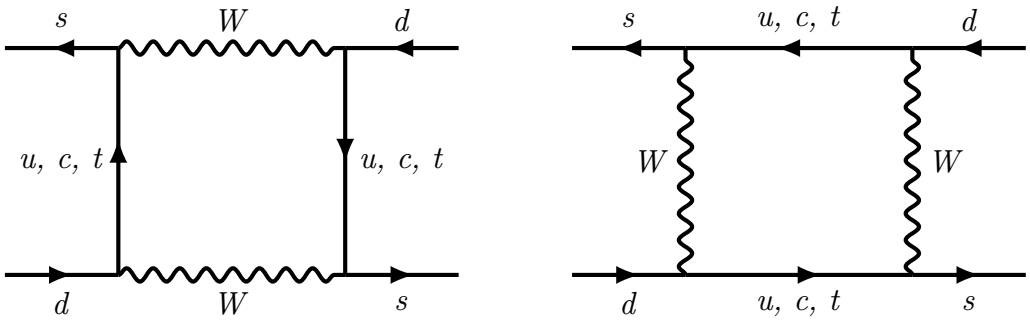

Figure 2.2: Ilustration of neutral meson mixing.

The key quantity to study CP-violation containing meson antimeson mixing is defined as follows:

$$\lambda_f = \frac{q}{p}\frac{\bar{A}_f}{A_f} = |\lambda_f| e^{i\phi_f}, \tag{2.5}$$

where A_f and $\bar{A}_f$ are the decay amplitudes and q/p is the relative phase from meson-antimeson mixing. In case of absence of direct CP-violation the $|A_f| = |\bar{A}_f|$, the CP-violation occurs if

$$\left|\frac{q}{p}\right| \neq 1. \tag{2.6}$$

This type of CP-violation is denoted as **CP-violation in mixing** of **indirect CP-violation**. Due to complex character of the equation 2.5, the CP-violation can occur if it meets following condition as well

$$\mathrm{Im}(\lambda_f) \neq 0. \tag{2.7}$$

This type of CP-violation measures the CP-violation in interference between a decay without mixing and decay with mixing usually denoted as **mixing-induced CP-violation**.

To measure an CP-violation for meson antimeson mixing the following time dependent asymmetry need to be studied

$$A_{CP} = \frac{\mathrm{d}\Gamma/\mathrm{d}t(M \to f) - \mathrm{d}\Gamma/\mathrm{d}t(\bar{M} \to f)}{\mathrm{d}\Gamma/\mathrm{d}t(M \to f) + \mathrm{d}\Gamma/\mathrm{d}t(\bar{M} \to f)} = \mathcal{S}_f \sin(\Delta m t) - \mathcal{C}_f \cos(\Delta m t), \tag{2.8}$$

where Δm is the mixing frequency, $\mathcal{S}_f$ mixing-induced CP-violation, and $\mathcal{C}_f$ is the direct CP-violation. The detailed description of CP-violation in the neutral B_s meson oscillation is given in chapter 3.

2.3.2 CKM Matrix

The meson states are also eigenstates of the strong and electromagnetic interactions. In the SM, all interaction vertices conserve flavour, except for the couplings of W bosons to fermions. The part of the SM lagrangian for the Yukawa coupling of the W boson to the quark fields is defined as follows

$$\mathcal{L}_W = \frac{g_w}{\sqrt{2}} \sum_{j,k=1,2,3} [V_{jk} \bar{u}_{jL} \gamma^\mu d_{kL} W_\mu^+] + [V_{jk}^* \bar{d}_{kL} \gamma^\mu u_{jL} W_\mu^-], \tag{2.9}$$

where the g_w is the weak coupling constant, $u = (u, c, t)$ and $d = (d, s, b)$ vectors that describe three quark generations and $V = V_{uL}^* V^{dL}$ is unitary Cabibbo-Kobayashi-Maskawa (CKM) [18, 19] matrix which take a form like

$$V = \begin{pmatrix} V_{ud} & V_{us} & V_{ub} \\ V_{cd} & V_{cs} & V_{cb} \\ V_{td} & V_{ts} & V_{tb} \end{pmatrix} \tag{2.10}$$

The CKM matrix induces flavour-changing transitions inside and between generations in the charged sector at tree level. Because the CKM matrix is complex and unitary, it can be parameterized by the three mixing angles and the CP-violating phase. The parametrization can by done in several ways where the values of mixing angles and

phase are different, but the standard choice has become

$$
\begin{aligned}
V &= \begin{pmatrix} 1 & 0 & 0 \\ 0 & c_{23} & s_{23} \\ 0 & -s_{23} & c_{23} \end{pmatrix} \begin{pmatrix} c_{13} & 0 & s_{13}e^{-i\delta} \\ 0 & 1 & 0 \\ -s_{13}e^{i\delta} & 0 & c_{13} \end{pmatrix} \begin{pmatrix} c_{12} & s_{12} & 0 \\ -s_{12} & c_{12} & 0 \\ 0 & 0 & 1 \end{pmatrix} \\
&= \begin{pmatrix} c_{12}c_{13} & s_{12}c_{13} & s_{13}e^{-i\delta} \\ -s_{12}c_{23} - c_{12}s_{23}s_{13}e^{i\delta} & c_{12}c_{23} - s_{12}s_{23}s_{13}e^{i\delta} & s_{23}c_{13} \\ s_{12}s_{23} & -c_{12}s_{23} - s_{12}c_{23}s_{13}e^{i\delta} & c_{23}c_{13} \end{pmatrix},
\end{aligned}
\tag{2.11}
$$

where the $s_{ij} = \sin\theta_{ij}$, $c_{ij} = \cos\theta_{ij}$ with θ_{ij} being angles rotating in flavour space and δ is the CP-violating phase. The real angles θ_{ij} may be chosen so that $0 \leq \theta_{ij} \leq \pi/2$, and the phase δ_{13} so that $-\pi < \delta_{13} \leq \pi$.

According to experimental evidence, there exist a hierarchy of $s_{13} \ll s_{23} \ll s_{12} \ll 1$. This hierarchy can be expressed by Wolfenstein parameterization [20] using the four phase convention–independent quantities defined as follows:

$$
\begin{gathered}
s_{12}^2 \equiv \lambda^2 = \frac{|V_{us}|^2}{|V_{ud}|^2 + |V_{us}|^2}, \quad s_{23}^2 \equiv A^2\lambda^4 = \frac{|V_{cb}|^2}{|V_{ud}|^2 + |V_{us}|^2}, \\
s_{13}e^{i\delta} \equiv A\lambda^3(\bar{\rho} + i\bar{\eta}) = -A\lambda^3 \frac{V_{ud}V_{ub}^*}{V_{cd}V_{cb}^*}.
\end{gathered}
\tag{2.12}
$$

The Wolfenstein parametrization is popular not only because it transparently reveals the hierarchy, but because the imaginary part is suppressed to third order of λ and the CKM matrix can be expanded in powers of the small parameter $\lambda \approx 0.22$. The expansion up to $\mathcal{O}(\lambda^4)$ yields the following parametrization of the CKM matrix:

$$
V_{CKM} = \begin{pmatrix} 1 - \lambda^2/2 & \lambda & A\lambda^3(\rho - i\eta) \\ -\lambda & 1 - \lambda^2/2 & A\lambda^2 \\ A\lambda^3(1 - \rho - i\eta) & -A\lambda^2 & 1 \end{pmatrix} + \mathcal{O}(\lambda^4). \tag{2.13}
$$

Because the CKM matrix is complex, CP-violation is allowed only if $\bar{\eta}$ differs from zero. Since CP-violation involves phases of CKM elements, many measurements of CP-violating observables can be used to constrain these angles and the $\bar{\rho}$, $\bar{\eta}$ parameters. The latest results on CKM parameters is given by the fit to all available measurements and imposing the SM constraints [4]. Using Wolfenstein parameters we can write following values:

$$
\begin{aligned}
\lambda &= 0.22453 \pm 0.00044, & A &= 0.836 \pm 0.015, \\
\bar{\rho} &= 0.122^{+0.018}_{-0.017}, & \bar{\eta} &= 0.355^{+0.012}_{-0.011}.
\end{aligned}
\tag{2.14}
$$

2.3.3 Unitarity Triangle

The unitarity condition of the CKM matrix can be expressed by following equations: $\sum_i V_{ij}V_{ik}^* = \delta_{jk}$ and $\sum_i V_{ji}V_{ki}^* = \delta_{jk}$. If we take off-diagonal terms, where the $j \neq k$ and the $\delta_{jk} = 0$, the relations can be represented by a triangle in the complex plane. The areas of all triangles are the same, half of the Jarlskog invariant (J) [21] which is a phase-convention-independent measure of CP-violation. The J is defined as follows

$$J = Im[V_{td}^* V_{tb} V_{ub}^* V_{ud}] = c_{12}c_{23}c_{21}s_{12}s_{23}s_{13}\sin\delta_{13} \simeq A^2\lambda^6\bar{\eta}. \tag{2.15}$$

The most commonly used unitarity triangle arises from the $(j,k) = (3,1)$ where the three sides are similar order of magnitude and triangle equation is rescaled dividing by a factor $V_{cd}V_{cb}^*$. The unitarity triangle equation then takes form

$$\frac{V_{ud}V_{ub}^*}{V_{cd}V_{cb}^*} + \frac{V_{td}V_{tb}^*}{V_{cd}V_{cb}^*} + 1 = 0. \tag{2.16}$$

The sides of the triangle are given by the following relations:

$$R_u = \left|\frac{V_{ud}V_{ub}^*}{V_{cd}V_{cb}^*}\right| = \sqrt{\bar{\rho}^2 + i\bar{\eta}^2}, \quad R_t = \left|\frac{V_{td}V_{tb}^*}{V_{cd}V_{cb}^*}\right| = \sqrt{(1-\bar{\rho})^2 + \bar{\eta}^2}. \tag{2.17}$$

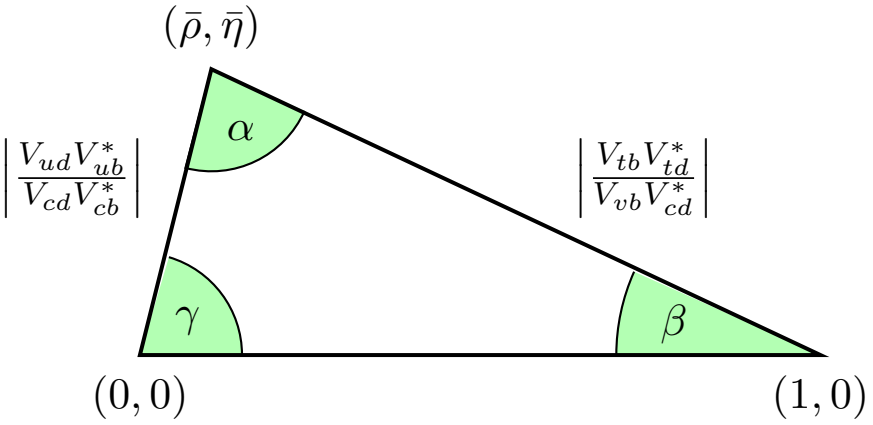

Figure 2.3: The unitarity triangle.

The CP-violation parameters are associated with three angles in the triangle which

are defined as follows:

$$\begin{aligned}
\alpha &= \arg\left(-\frac{V_{td}V_{tb}^*}{V_{ud}V_{ub}^*}\right) = \arg\left(-\frac{1-\bar{\rho}-i\bar{\eta}}{\bar{\rho}+i\bar{\eta}}\right), \\
\beta &= \arg\left(-\frac{V_{cd}V_{cb}^*}{V_{td}V_{tb}^*}\right) = \arg\left(-\frac{1}{1-\bar{\rho}-i\bar{\eta}}\right), \\
\gamma &= \arg\left(-\frac{V_{ud}V_{ub}^*}{V_{cd}V_{cb}^*}\right) = \arg(\bar{\rho}+i\bar{\eta}).
\end{aligned} \tag{2.18}$$

The triangle for the equation 2.16 with angles 2.18 and sides given by 2.17 is depicted in Figure 2.3.

The condition of non-vanishing $\bar{\eta}$ for the existence of CP-violation in the quark sector is represented as non-flat unitarity triangle. This graphical representation is commonly used to illustrates the constraints of CP-violation parameters on the $\bar{\rho}$, $\bar{\eta}$ plane from various measurements. The Figure 2.4 depicts unitarity triangle for the latest results from the CKM fitter group [22], where the shaded 95% Confidence Level (CL) regions all overlap consistently around the global fit region.

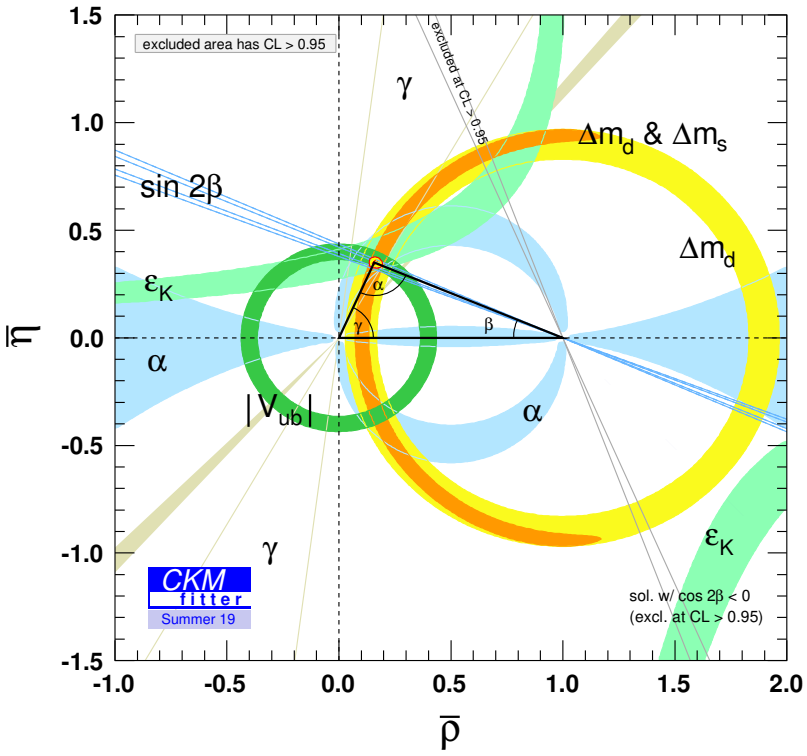

Figure 2.4: Constraints of CP-violation parameters on the $\bar{\rho}$, $\bar{\eta}$ plane [22].

2.4 Strong Interaction

2.4.1 Color

The color is an additional internal degree of freedom of quarks. This degree of freedom was introduced after the observation of Δ^{++} baryon, which is composed of three up quarks. This baryon would break the Pauli exclusion principle [23] without introduction of another degree of freedom, called color charge. There are three colors red, green and blue with their respective anticolors. As stated above, strong interaction is mediated by an exchange of massless gluons. These gluons carry color and anticolor charge and provide color interaction between two quarks as can be seen in Figure 2.5. With three colors and three anticolors, there is a colored gluon octet $3 + 3 = 8 \oplus 1$, with possible combinations taking the form of

$$r\bar{b},\ r\bar{g},\ b\bar{g},\ b\bar{r},\ g\bar{r},\ g\bar{b},\ \frac{1}{\sqrt{2}}(r\bar{r} - b\bar{b}),\ \frac{1}{\sqrt{6}}(r\bar{r} + b\bar{b} - 2g\bar{g}), \tag{2.19}$$

and a colorless gluon singlet $\frac{1}{\sqrt{3}}(r\bar{r} + b\bar{b} + g\bar{g})$.

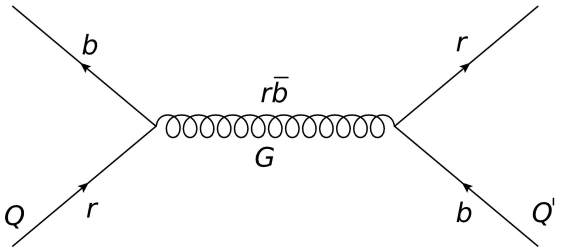

Figure 2.5: $\mathcal{Q}\mathcal{Q}'$ interaction via colored gluon exchange. The time runs from bottom to top.

The color charge of the strong interaction is analogous to the electric charge in the electromagnetic interaction. Both forces are mediated by massless vector particles, but compared to photons, gluons can interact with each other. This phenomenon is called gluon self coupling. Due to gluon self coupling, the color charge exhibits a particular behavior called antiscreening. It is the opposite to the screening of electric charge in QED as it is illustrated in Figure 2.6.

Both baryons and mesons must be colorless, thus quarks and gluons are confined inside hadrons. No free quarks were observed, with an exception of the top quark, which decays before it has a chance to hadronize.

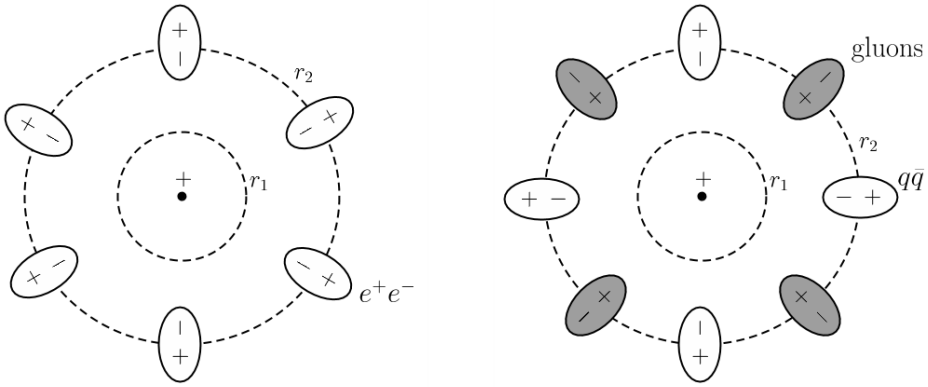

(a) (b)

Figure 2.6: Screening of electric charge in QED by virtual electron-positron pairs in (a) and antiscreening of the color charge by gluons and screening by quarks in (b) in QCD [24].

2.4.2 QCD

The theory describing the interactions between quarks and gluons based on a color exchange is called quantum chromodynamics (QCD) and it is a part of SM. The QCD is a non-Abelian theory represented by 3×3 matrices in the $SU(3)$ group. The non-Abelian behavior of the theory results in the self interaction of the gluons. The lagrangian of the QCD can be written as

$$\mathcal{L}_{QCD} = \sum_f \bar{\psi}_i^{(f)}(i\gamma_\mu D_{ij}^\mu - m_f\delta_{ij})\psi_j^{(f)} - \frac{1}{4}F_{\mu\nu}^a F_a^{\mu\nu}, \tag{2.20}$$

where the D_{ij}^μ is covariant derivative acting in color space, γ_μ are Dirac γ-matrices, ψ are quark field spinors, f correspond to the flavour of the quark and m corresponds to its mass. The covariant derivative in QCD has the following form

$$D_{ij}^\mu = \partial_\mu\delta_{ij} + ig_s t_{ij}^a A_a^\mu, \tag{2.21}$$

where A_a^μ represent gluon field, g_s is strong coupling and t_{ij}^a are the generators of the $SU(3)$ group. The field-strength tensor derived from A_a^μ can be formulated as

$$F_{\mu\nu}^a = \partial_\mu A_\nu^a - \partial_\nu A_\mu^a - g_s f_{abc} A_\mu^b A_\nu^c, \tag{2.22}$$

where f_{abc} are the structure constants of the $SU(3)$.

Despite photons and gluons being massless, the QCD potential takes a different form

due to the differences between those forces. The simplest potential model for mesons that describes strong interaction is called Cornell potential [25], which takes the form:

$$V_s(r) = -\frac{4}{3}\frac{\alpha_s}{r} + kr, \tag{2.23}$$

where α_s is the strong interaction coupling and k is a free parameter. The first part of the equation is similar to the Coulomb potential with a factor of $\frac{4}{3}$. This factor arises from eight color gluon states averaged over three quark colors. The factor is divided by 2 from the definition of α_s. The second, linear term is associated with color confinement at large r, where k is the tension of color flux tubes.

The Cornell potential can be extended by inclusion of the spin interaction between quarks. These spin-dependent potentials are assumed to be dominated by a one-gluon exchange and consist of spin-spin, tensor and spin-orbit terms. For a system of two quarks, the potential takes the following form [26]:

$$V_{q\bar{q}} = -\frac{4}{3}\frac{\alpha_s}{r} + \sigma r + \frac{32\pi\alpha_s}{9m_q^2}\delta(r)\mathbf{S}_q \cdot \mathbf{S}_{\bar{q}} + \frac{1}{m_q^2}\left[\left(\frac{2\alpha_s}{r^3} - \frac{b}{2r}\right)\mathbf{L}\cdot\mathbf{S} + \frac{4\alpha_s}{r^3}\mathbf{T}\right], \tag{2.24}$$

where the $\mathbf{L}$ is an orbital momentum, $\mathbf{S}_q$ is a spin momentum of a particular quark, $\mathbf{S} = \mathbf{S}_q + \mathbf{S}_{\bar{q}}$ and $\mathbf{T}$ is a tensor term.

These extended models give better results, but still they are not satisfactory. Thus, new interquark potential models are being developed and tested.

2.4.3 Running Coupling

Charge screening in QED (screening) and QCD (antiscreening) leads to the concept of a running coupling (the energy dependence of a strong coupling). In the QED, the coupling becomes large at (very) short distances and large energies, but its effect is small. In the QCD, the antiscreening effect causes the strong coupling to become small at a short distance (large momentum transfer). This causes the quarks inside hadrons to behave more or less like free particles. This property of the strong interaction is called asymptotic freedom.

On the other hand, at the increasing distance, the coupling becomes so strong that it is impossible to isolate a quark from a hadron. In addition, if the quark pair receives more energy than is necessary for the production of a new quark-antiquark pair, then it is energetically favourable to produce a new quark pair. This mechanism is called color confinement.

Using perturbative QCD (pQCD) calculations and experimental data, the coupling

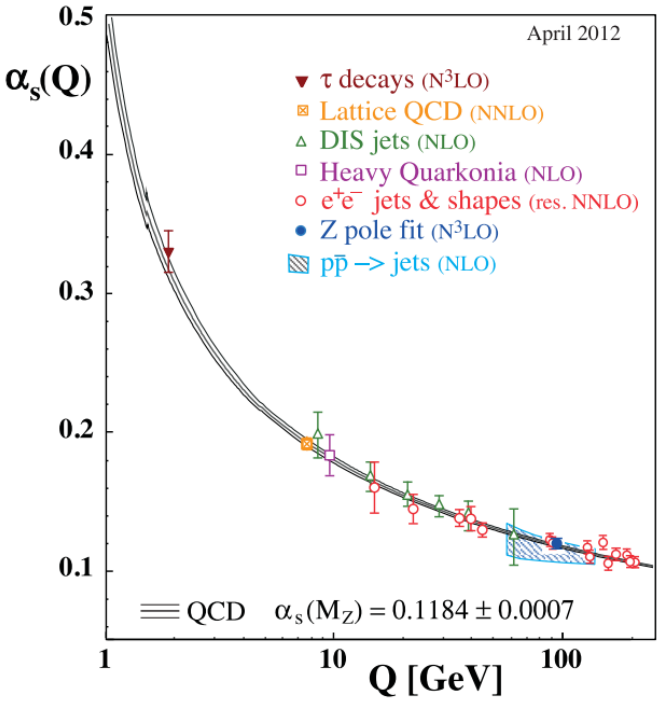

Figure 2.7: Summary of measurements of $\alpha_s(Q)$ as a function of the respective energy scale Q. The respective degree of the QCD perturbation theory used in the extraction of α_s is indicated in brackets (NLO: next-to-leading order; NNLO: next-to-next-to leading order; res. NNLO: NNLO matched with resumed next-to-leading logs; N^{3}LO: next-to-NNLO)[†][4].

constant of the QCD can be shown to have the following energy scale-dependence

$$\alpha_s(Q) = \frac{2\pi}{\beta_0 \ln \frac{Q}{\Lambda_{\mathrm{QCD}}}}, \tag{2.25}$$

where $\beta_0 = 11 - \frac{2}{3}n_f$, with n_f being the number of the active quark flavour, and Λ_{QCD} is the QCD scale [4]. The value of $\Lambda_{\mathrm{QCD}} = (0.339 \pm 0.010)$ GeV is determined by experiments. This dependence is valid only for $Q^2 \gg 2\Lambda^2$, where Q is the transferred momentum. The summary of measurements of $\alpha_s(Q)$ from multiple experiments is shown in Figure 2.7.

[†]NLO etc. are the levels of the perturbation QCD theory into which the Feynman diagrams are counted.

CHAPTER 3

Physics of the Neutral B-mesons

The neutral B_s^0 meson can oscillate into its antiparticle $\overline{B_s^0}$ and vice versa, as was previously discussed previously in section 2.3.1. This phenomenon is usually referred to as $B_s^0 - \overline{B}_s^0$ oscillation, which can be described in SM on the particle level by the box Feynman diagrams shown in Figure 3.1. The phenomenological aspects of the neutral B-mesons oscillation are taken from Refs. [4, 27, 28, 29].

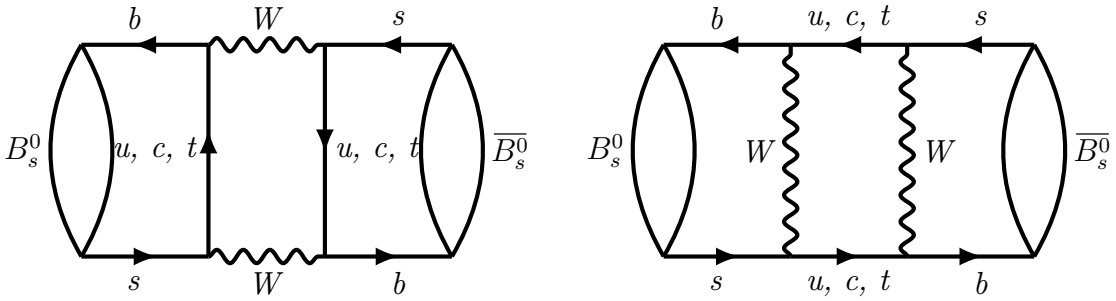

Figure 3.1: The box diagram of $B_s^0 - \overline{B_s^0}$ mixing.

The initial state of a $B_s^0 - \overline{B}_s^0$ system in a given time is a superposition of $|B_s^0\rangle$ and $|\overline{B}_s^0\rangle$ and can be written as:

$$|\psi(t)\rangle = a(t)\,|B_s^0\rangle + b(t)\,|\overline{B_s^0}\rangle\,, \tag{3.1}$$

where $a(t)$ and $b(t)$ are time evolution operators. The time evolution would produce components that describe all possible decay final states $\{f_1, f_2, ...\}$. However, because the main object of our interest are the values of $a(t)$ and $b(t)$, then the simplified formalism can be used. Using the simplified formalism, the evolution of initial state $|\psi(t)\rangle$ is given

by the Schrödinger equation:

$$i\hbar\frac{\partial}{\partial t}\psi(t) = H\psi(t), \tag{3.2}$$

where the H is the 2×2 effective Hamiltonian written in the rest frame of $B_s^0 - \overline{B}_s^0$ system that is not Hermitian. The complex matrix H can be decomposed and written in terms of two Hermitian matrices $M = M^\dagger$ and $\Gamma = \Gamma^\dagger$ written as

$$H = M - \frac{i}{2}\Gamma, \tag{3.3}$$

where the matrix M is related to the mass while matrix Γ is related to the exponential decay. The diagonal elements M_{11} and M_{22} are the masses of B_s^0 and $\overline{B_s^0}$ and are generated from the quark mass terms in $\mathcal{L}$ and from the binding energy of the strong interaction. The off-diagonal terms can be expressed as follows

$$M_{12} = \frac{H_{12} + H_{21}^*}{2}, \quad \frac{\Gamma_{12}}{2} = i\frac{H_{12} - H_{21}^*}{2}, \tag{3.4}$$

where the first equation is related to dispersive (off-shell) contribution to H_{12} and second equation to absorptive (on-shell) contribution to H_{12}.

Hamiltonian Diagonalization

Assuming the CPT symmetry is conserved, the Hamiltonian H can be simplified using $M_{11} = M_{22} = M$, $\Gamma_{11} = \Gamma_{22} = \Gamma$ and mass eigenstates can be calculated from diagonalization of the matrix H. The eigenvectors of H have well-defined masses and decay widths. To specify the components of the strong interaction eigenstates $|B_s^0\rangle$ and $|\overline{B_s^0}\rangle$ into the $|B_L\rangle$ and $|B_H\rangle$ mass eigenstates, where L and H stands for light and heavy, two complex parameters p and q need to be introduced. Then the mass eigenstates can be written as

$$\begin{aligned} |B_L\rangle &= p\,|B_s^0\rangle + q\,|\overline{B_s^0}\rangle \\ |B_H\rangle &= p\,|B_s^0\rangle - q\,|\overline{B_s^0}\rangle\,, \end{aligned} \tag{3.5}$$

with normalization of $|p|^2 + |q|^2 = 1$ and ϵ defined as follows

$$\frac{p}{q} = \frac{1-\bar{\epsilon}}{1+\bar{\epsilon}} = \sqrt{\frac{M_{12}^* - \frac{i}{2}\Gamma_{12}^*}{M_{12} - \frac{i}{2}\Gamma_{12}}}. \tag{3.6}$$

Standard notation to describe masses and decay widths of mass eigenstates $|B_{L,H}\rangle$ is given by $M_{L,H}$ and $\Gamma_{L,H}$, respectively, with eigenvalues

$$\sigma_{L,H} = M_{L,H} - i\frac{\Gamma_{L,H}}{2}. \tag{3.7}$$

The difference in mass and width between $|B_{L,H}\rangle$ and $|B_{L,H}\rangle$ are related to the off-diagonal elements of the mass and decay matrices, while the averages are related to the diagonal ones as follows:

$$\begin{aligned} m = \frac{M_H + M_L}{2} = M_{11}, \quad \Gamma = \frac{\Gamma_L + \Gamma_H}{2} = \Gamma_{11}, \\ \Delta m = M_H - M_L \simeq 2|M_{12}|, \quad \Delta\Gamma = \Gamma_L - \Gamma_H \simeq 2|\Gamma_{12}|\cos\phi, \end{aligned} \tag{3.8}$$

where the ϕ is CP-phase defined as

$$\phi = \arg\left(-\frac{M_{12}}{\Gamma_{12}}\right). \tag{3.9}$$

Three physical quantities of meson antimeson mixing are then $\Delta\Gamma$, Δm and ϕ. Here Δm is positive by definition, but the sign of $\Delta\Gamma$ must be experimentally determined.

The approximation of off-diagonal terms in equation 3.8 is given by comparison of real and imaginary part of secular equation solution for the eigenvalues of H:

$$\left(\Delta m + i\frac{\Delta\Gamma}{2}\right)^2 = 4\left(M_{12} - i\frac{\Gamma_{12}}{2}\right)\left(M_{12}^* - i\frac{\Gamma_{12}^*}{2}\right), \tag{3.10}$$

under condition that $|\Gamma_{12}| \ll |M_{12}|$ and $|\Delta\Gamma| \ll |\Delta m|$, which holds up to correction of order $|\Gamma_{12}/M_{12}|$ for the B_s^0 system.

Time Evolution

The time evolution of the mass eigenstates is governed by two eigenvalues $M_L - i\Gamma_L/2$ and $M_H - i\Gamma_H/2$:

$$|B_{L,H}(t)\rangle = e^{-(iM_{L,H}+\Gamma_{L,H}/2)t}\,|B_{L,H}\rangle\,, \tag{3.11}$$

where $|B_{L,H}\rangle$ denotes the mass eigenstates at time $t = 0$. The time evolution of initial $|B_s^0\rangle$ and $|\overline{B_s^0}\rangle$ can be then expressed as:

$$\begin{aligned} |B_s^0(t)\rangle &= \frac{1}{2p}\left[e^{-iM_Lt-\Gamma_Lt/2}\,|B_L\rangle + e^{-iM_Ht-\Gamma_Ht/2}\,|B_H\rangle\right], \\ |\overline{B_s^0}(t)\rangle &= \frac{1}{2p}\left[e^{-iM_Lt-\Gamma_Lt/2}\,|B_L\rangle - e^{-iM_Ht-\Gamma_Ht/2}\,|B_H\rangle\right]. \end{aligned} \tag{3.12}$$

Using equation 3.5 the mass eigenstates can be eliminated in favor of the flavour states giving following results

$$\begin{aligned} |B_s^0(t)\rangle &= g_+(t)\,|B_s^0\rangle + \frac{p}{q}g_-(t)\,|\overline{B_s^0}\rangle\,, \\ |\overline{B_s^0}(t)\rangle &= \frac{p}{q}g_-(t)\,|B_s^0\rangle + g_+(t)\,|\overline{B_s^0}\rangle\,, \end{aligned} \tag{3.13}$$

where

$$\begin{aligned} g_+(t) &= e^{imt}e^{-\Gamma t/2}\left[\cosh\frac{\Delta\Gamma t}{4}\cos\frac{\Delta m t}{2} - i\sinh\frac{\Delta\Gamma t}{4}\sin\frac{\Delta m t}{2}\right], \\ g_-(t) &= e^{imt}e^{-\Gamma t/2}\left[-\sinh\frac{\Delta\Gamma t}{4}\cos\frac{\Delta m t}{2} + i\cosh\frac{\Delta\Gamma t}{4}\sin\frac{\Delta m t}{2}\right]. \end{aligned} \tag{3.14}$$

The probability to find particle in final state B_s^0 or $\overline{B_s^0}$ which was initial produced as pure B_s^0 or $\overline{B_s^0}$ state is given by

$$\begin{aligned} |\langle B_s^0|B_s^0(t)\rangle| &= |g_+(t)|^2, \qquad |\langle B_s^0|\overline{B_s^0}(t)\rangle| = \left|\frac{p}{q}\right|^2 |g_-(t)|^2, \\ |\langle \overline{B_s^0}|B_s^0(t)\rangle| &= \left|\frac{q}{p}\right|^2 |g_-(t)|^2, \qquad |\langle \overline{B_s^0}|\overline{B_s^0}(t)\rangle| = |g_+(t)|^2, \end{aligned} \tag{3.15}$$

where the

$$\begin{aligned} |g_\pm(t)|^2 &= \frac{e^{-\Gamma t}}{2}\left[\cosh\frac{\Delta\Gamma t}{2} \pm \cos(\Delta m t)\right] \text{ and} \\ g_+^*(t)g_-(t) &= \frac{e^{-\Gamma t}}{2}\left[\sinh\frac{\Delta\Gamma t}{2} + i\sin(\Delta m t)\right]. \end{aligned} \tag{3.16}$$

Time-Dependent Decay Rates

With the dynamics of flavour oscillation established, the decay of the flavour states can be examined. The time-dependent decay rate $\Gamma(B_s^0(t) \to f)$ of an initially tagged B_s^0 flavour eigenstate into some final state f is given by

$$\Gamma(B_s^0(t) \to f) = \frac{1}{N_B}\frac{\mathrm{d}N(B_s^0 \to f)}{\mathrm{d}t}, \tag{3.17}$$

where $\mathrm{d}N(B_s^0 \to f)$ denotes the number of decays of a B-meson tagged as a B_s^0 at $t = 0$ into final state f occurring within the time interval between t and $t+\mathrm{d}t$. The total number of B_s^0 mesons produced at time $t = 0$ is denoted by N_B. The previous equation can be expressed in terms of decay amplitudes

$$\Gamma(B_s^0(t) \to f) = \mathcal{N}_f|\langle f|\mathcal{H}|B_s^0(t)\rangle|^2 = \mathcal{N}_f|A_f|^2, \tag{3.18}$$

where $\mathcal{N}_f$ is time-independent normalization factor and A_f is the decay amplitude. An analogous definition can be written for the $\Gamma(\overline{B_s^0}(t) \to f)$ defining decay amplitude $\overline{A_f}$. The important quantity connected to the decay amplitudes is λ_f defined in equation 2.5.

Using equation 3.13 and 3.14, the time dependent decay rates can be written as follows:

$$\begin{aligned}\Gamma(B_s^0(t)\to f) = \mathcal{N}_f|A_f|^2 e^{-\Gamma t}\Bigg\{&\frac{1+|\lambda_f|^2}{2}\cosh\frac{\Delta\Gamma t}{2} + \frac{1-|\lambda_f|^2}{2}\cos(\Delta m t)\\ &-\mathrm{Re}(\lambda_f)\sinh\frac{\Delta\Gamma t}{2} - \mathrm{Im}(\lambda_f)\sin(\Delta m t)\Bigg\},\\ \Gamma(\overline{B_s^0}(t)\to f) = \mathcal{N}_f|A_f|^2\left|\frac{p}{q}\right|^2 e^{-\Gamma t}\Bigg\{&\frac{1+|\lambda_f|^2}{2}\cosh\frac{\Delta\Gamma t}{2} - \frac{1-|\lambda_f|^2}{2}\cos(\Delta m t)\\ &-\mathrm{Re}(\lambda_f)\sinh\frac{\Delta\Gamma t}{2} + \mathrm{Im}(\lambda_f)\sin(\Delta m t)\Bigg\}.\end{aligned} \tag{3.19}$$

Time-Dependent Asymmetry

CP-violation in interference between the mixing and the decay amplitudes can be observed using the asymmetry of the neutral meson decays into final CP-eigenstate f_{CP}, which can be defined as follows

$$A_{f_{CP}}(t) = \frac{\Gamma(\overline{B_s^0}(t)\to f_{CP}) - \Gamma(B_s^0(t)\to f_{CP})}{\Gamma(\overline{B_s^0}(t)\to f_{CP}) + \Gamma(B_s^0(t)\to f_{CP})}. \tag{3.20}$$

Using equation 3.19 one can derive asymmetry in following form

$$A_{f_{CP}}(t) = \frac{A_{CP}^{mix}\sin(\Delta m t) - A_{CP}^{dir}\cos(\Delta m t)}{\cosh(\Delta\Gamma t/2) + A_{\Delta\Gamma}\sinh(\Delta\Gamma t/2)}, \tag{3.21}$$

where the asymmetries from direct CP-violation, mixing-induced CP-violation and untagged asymmetry are

$$A_{CP}^{dir} = \frac{1-|\lambda_f|^2}{1+|\lambda_f|^2}, \quad A_{CP}^{mix} = \frac{2\,\mathrm{Im}(\lambda_f)}{1+|\lambda_f|^2}, \quad A_{\Delta\Gamma} = -\frac{2\,\mathrm{Re}(\lambda_f)}{1+|\lambda_f|^2}, \tag{3.22}$$

and $|A_{CP}^{dir}|^2 + |A_{CP}^{mix}|^2 + |A_{\Delta\Gamma}|^2 = 1$. The decays where all contributing Feynman diagrams carry the same CP-violating phase are called golden modes. In the golden modes the decay amplitudes satisfy $|A_f| = |\overline{A_f}|$ which lead to $|\lambda_f| = 1$ and thus no direct CP-violation is observed, $A_{CP}^{dir} = 0$. The mixing-induced asymmetry is then simplified to

$$A_{CP}^{mix} = \mathrm{Im}(\lambda_f) \tag{3.23}$$

and can be directly related to the CKM matrix elements.

3.1 CP-Violation in the $B_s^0 \to J/\psi\phi$ Channel

The decay of B_s^0 into $J/\psi \to \mu^+\mu^-$ and $\phi \to K^+K^-$ is one of the golden modes for the measurement of the CP-violation phase. The CP-violation occurs due to interference between the mixing and the decay amplitudes, which leads to a time-dependent CP-violating asymmetry between the decay time distributions of B_s^0 and $\overline{B_s^0}$ mesons as described in previous section. The $B_s^0 \to J/\psi\phi$ decay proceeds via the quark transition $\bar{b} \to \bar{c}c\bar{s}$ with two contributing processes: tree level diagram (t_f) and penguin diagram (p_f^q), which are shown in Figure 3.2. The total decay amplitude including both effects is

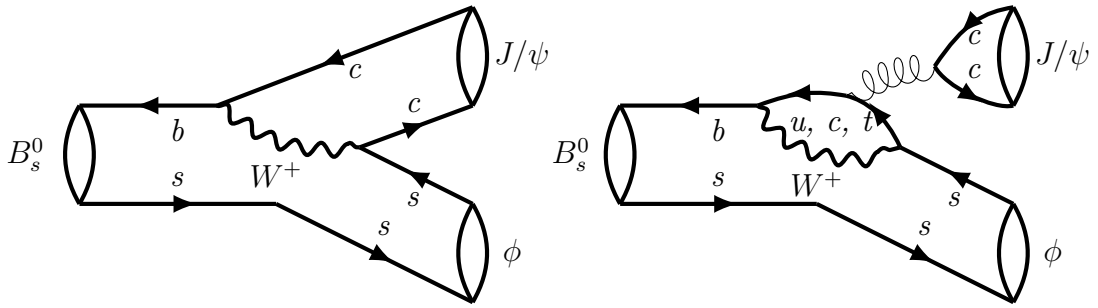

Figure 3.2: The Feynman diagrams describing the process of the $B_s^0 \to J/\psi\phi$ decay. The left diagram stands for the tree decay, while the right is describing Penguin diagram.

then given by

$$A_f = (V_{cb}^* V_{cs}) t_f + \sum_{q=u,c,t} (V_{qb}^* V_{qs}) p_f^q, \tag{3.24}$$

where f denotes the given final state. However, the penguin amplitudes are highly suppressed, therefore the decay process is dominated by a single CKM amplitude.

The prediction for the three physics variables of $B_s^0 - \overline{B_s^0}$ mixing the ϕ_s, $\Delta\Gamma_s$ and Δm_s are based on the Standard Model and the CKM matrix elements. For the CP-violating phase ϕ_s, the prediction is given with high precision:

$$\phi_s \simeq -2\beta_s = -2\arg\left(\frac{V_{ts}V_{tb}^\star}{V_{cs}V_{cb}^\star}\right) = (-0.0366 \pm 0.0020)\,\text{rad}, \tag{3.25}$$

so any significant measured excess would be a clear indication of New Physics entering the B_s^0 system. The Δm_s is sensitive to new physics as well; however, the theoretical predictions are calculated with high uncertainty. The $\Delta\Gamma_s$ is not sensitive to the New Physics; however, measurement is interesting to test a theoretical predictions. The latest theoretical predictions of the $\Delta\Gamma_s$ and Δm_s values are [30]

$$\Delta\Gamma_s = (0.085 \pm 0.015)\,\text{ps}^{-1}, \qquad \Delta m_s = (18.3 \pm 2.7)\,\text{ps}^{-1}. \tag{3.26}$$

The experimental measurement of the $B_s^0 - \overline{B_s^0}$ mixing parameters was previously done at CDF and DØ experiments at the Tevatron collider [31]. Since the LHC era began, the significant improvement in the statistical precision of the ϕ_s was achieved. The measured values of $B_s^0 - \overline{B_s^0}$ mixing parameters are summarized in Table 3.1.

	ϕ_s[rad]	$\Delta\Gamma_s$[ps^{-1}]
CDF [32]	$[-0.60, 0.12]$, 68 % CL	$0.068 \pm 0.026 \pm 0.009$
DØ [33]	$-0.55^{+0.38}_{-0.36}$	$0.163^{+0.065}_{-0.064}$
CMS [34]	$-0.075 \pm 0.097 \pm 0.031$	$0.095 \pm 0.013 \pm 0.007$
ATLAS [35]	$-0.087 \pm 0.037 \pm 0.019$	$0.0640 \pm 0.0042 \pm 0.0024$
LHCb [36]	-0.040 ± 0.025	0.0813 ± 0.0048

Table 3.1: The summary of experimental results of $B_s^0 - \overline{B_s^0}$ mixing parameters in $B_s^0 \to J/\psi(\mu^+\mu^-)\phi(K^+K^-)$ channel.

The combination of the experimental results, including combined ATLAS Run 1 and Run 2 measurement, was done by Heavy Flavour Combination Group (HFLAV) and is shown in Figure 3.3. As can be seen, the combination of results is consistent with the SM prediction, but in order to exclude any BSM physics, more precise measurements are needed.

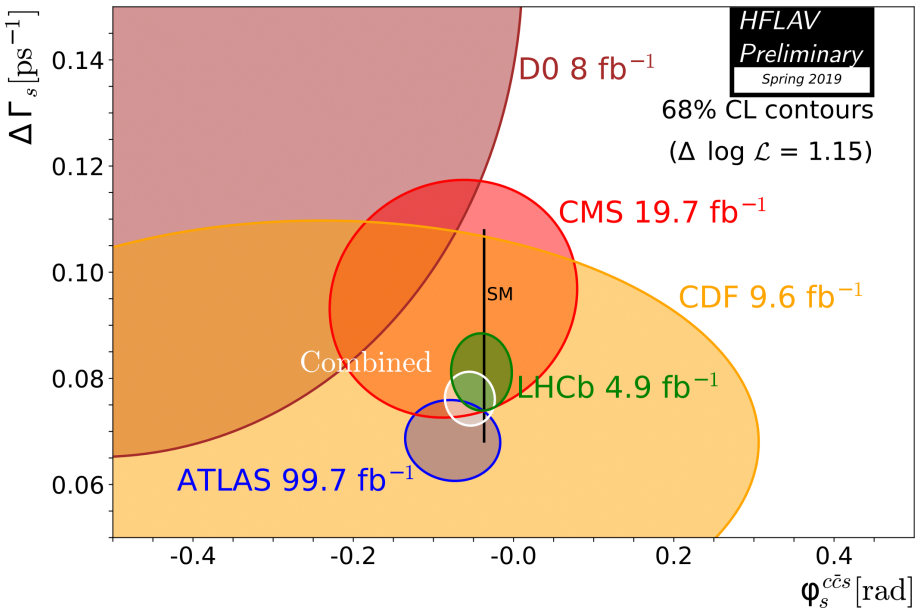

Figure 3.3: 68% CL contours in the (ϕ_s, $\Delta\Gamma_s$) plane, showing the measurements from CDF, DØ, ATLAS, CMS and LHCb along with their combination. The thin black rectangle represents the Standard Model predictions of ϕ_s and $\Delta\Gamma_s$ [37].

The experimental measurement of physics variables uses the fact that the final state particles of $B_s^0 \to J/\psi(\mu^+\mu^-)\phi(K^+K^-)$ decay are both vector mesons and thus the CP-odd (L=1) and CP-even (L=0,2) amplitudes can be statistically disentangled through a full time-dependent angular analysis. For the description of the angular distributions, the helicity and transversity formalism, described in following sections, is used.

3.2 The Helicity and Transversity Formalism

To describe the angular distribution of the two vector final state mathematically, the Helicity or Transversity formalism can be used.

The Helicity Basis

The helicity of a particle, denoted by the λ, is defined as being the component of the spin projected along the direction of its momentum. The possible values of helicity are $-1, 0, 1$. However, the final state helicities are constrained by initial particle orbital angular momentum

$$|\lambda_{J/\psi} - \lambda_\phi| = J(B_s^0). \tag{3.27}$$

Because $J(B_s^0) = 0$, the helicity of final state particles is constrained to $\lambda_{J/\psi} = \lambda_\phi$ and only three combinations are valid. The final state can be written as

$$|B_s^0\rangle = \sum_\lambda H_\lambda \, |f_\lambda\rangle \,, \tag{3.28}$$

with $\lambda = (+1, 0, 1)$ where the H_f are the helicity amplitudes for each helicity eigenstate.

The helicity formalism is commonly used; however, the disadvantage is that the helicity amplitudes are not eigenstates of CP.

The Transversity Basis

In the transversity basis, the spin of final particles is projected onto the rest frame defined by the other final particle. The decay amplitude can be decomposed into independent components, corresponding to the linear polarization states of the final state vector mesons. The polarization states can be longitudinal, A_0, or transverse to the direction of motion of final state vector mesons. In case of transverse polarization, the states can be parallel $A_\parallel$ or perpendicular $A_\perp$ to each other. The final state can be written as

$$|B_s^0\rangle = \sum_\lambda A_\lambda \, |f_\lambda\rangle \,, \quad \lambda = (\parallel, 0, \perp). \tag{3.29}$$

The relation between transversity and helicity amplitudes is given by

$$A_{\parallel} = \frac{H_{+1} + H_{-1}}{\sqrt{2}}, \quad A_{\perp} = \frac{H_{+1} - H_{-1}}{\sqrt{2}}, \quad A_0 = H_0. \tag{3.30}$$

The transversity eigenstates are aligned with CP-eigenstates, which allow cleaner extraction of the physics parameters and that is why the transversity basis is preferred by experiments.

3.3 Angular Analysis

The angles used to describe $B_s^0 \to J/\psi\phi$ final state in the transversity basis are denoted as $(\theta_T, \psi_T, \phi_T)$. These angles are defined in the rest frame of final particles with x-axis determined by the direction of ϕ meson in the J/ψ rest frame and the $x-y$ plane defined by the K^+K^- system with $p_y(K^+) > 0$. Within this coordinate system, θ_T and ϕ_T define the polar and azimuthal angles of the μ^+ in the rest frame of the J/ψ, while ψ_T defines the angle between momentum of $p(K^+)$ and $p(J/\psi)$ in the ϕ meson rest frame. The definition of transversity angles is schematically shown in Figure 3.4.

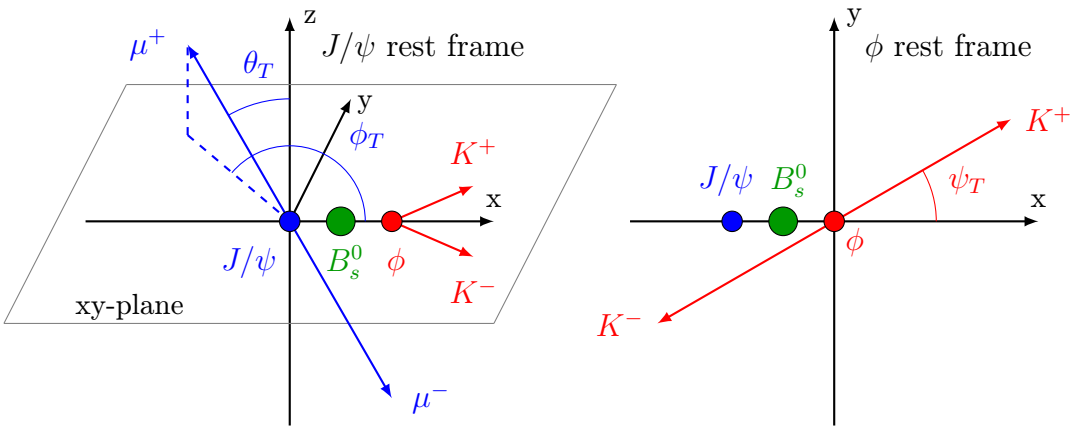

Figure 3.4: Illustration of the transversity angles between final state particles in the $B_s^0 \to J/\psi(\mu^+\mu^-)\phi(K^+K^-)$ decay.

For each of the transversity amplitudes, there is an associated phase $\delta_0 = \arg(A_0)$, $\delta_\perp = \arg(A_\perp)$ and $\delta_\parallel = \arg(A_\parallel)$. By convention, the phase $\delta_0 = 0$, since only phase differences between the amplitudes appear in the differential decay rate. These parameters are used for description of the resonant P-wave signal state; however, the primary signal is contaminated by other processes with the same finale state such as $B_s^0 \to J/\psi f_0$ ($f_0 \to K^+K^-$) or non resonant $B_s \to J/\psi K^+K^-$. These S-wave states have to be accounted for in the final description of the decay, using their own amplitude A_S and phase δ_S .

In general, the distribution of the time t and the transversity angles $\Omega(\theta_T, \psi_T, \phi_T)$ is given by the differential decay rate

$$\frac{\mathrm{d}^4\Gamma}{\mathrm{d}t\mathrm{d}\Omega} = \sum_{k=1}^{n} \mathcal{O}^{(k)}(t) g^{(k)}(\theta_T, \psi_T, \phi_T), \tag{3.31}$$

where $\mathcal{O}^{(k)}(t)$ are the time-dependent functions corresponding to the contributions of the four different amplitudes (A_0, $A_\parallel$, $A_\perp$, and A_S) and their interference terms and $g^{(k)}(\theta_T, \psi_T, \phi_T)$ are the angular functions.

Table 3.3 shows the final time dependent amplitudes and the additional S-wave terms. The amplitudes $k = (1 \to 6)$ correspond to the resonant P-wave states. Accounting for the S-wave contribution introduces an additional four amplitudes: the S-wave amplitude for $k = 7$ and interference terms between S-wave and P-wave decays for $k = (8 \to 10)$. To each amplitude $\mathcal{O}^{(k)}(t)$ corresponds an angular function $g^k(\theta_T, \psi_T, \phi_T)$. The summary of angular functions is shown in Table 3.2.

k	$g^k(\theta_T, \psi_T, \phi_T)$
1	$2\cos^2\psi_T(1-\sin^2\theta_T\cos^2\phi_T)$
2	$\sin^2\psi_T(1-\sin^2\theta_T\sin^2\phi_T)$
3	$\sin^2\psi_T\sin^2\theta_T$
4	$\frac{1}{\sqrt{2}}\sin 2\psi_T\sin^2\theta_T\sin 2\phi_T$
5	$-\sin^2\psi_T\sin 2\theta_T\sin\phi_T$
6	$\frac{1}{\sqrt{2}}\sin 2\psi_T\sin 2\theta_T\cos\phi_T$
7	$\frac{2}{3}\left(1-\sin^2\theta_T\cos^2\phi_T\right)$
8	$\frac{1}{3}\sqrt{6}\sin\psi_T\sin^2\theta_T\sin 2\phi_T$
9	$\frac{1}{3}\sqrt{6}\sin\psi_T\sin 2\theta_T\cos\phi_T$
10	$\frac{4}{3}\sqrt{3}\cos\psi_T\left(1-\sin^2\theta_T\cos^2\phi_T\right)$

Table 3.2: The angular functions $g^k(\theta_T, \psi_T, \phi_T)$ for $B_s^0 \to J/\psi\phi$ decay including S-wave contribution.

k	$\mathcal{O}^{(k)}(t)$
1	$\frac{1}{2}\lvert A_0(0)\rvert^2 \left[(1+\cos\phi_s)\,\mathrm{e}^{-\Gamma_{\mathrm{L}}^{(s)}t} + (1-\cos\phi_s)\,\mathrm{e}^{-\Gamma_{\mathrm{H}}^{(s)}t} \pm 2\mathrm{e}^{-\Gamma_s t}\sin(\Delta m_s t)\sin\phi_s\right]$
2	$\frac{1}{2}\lvert A_\parallel(0)\rvert^2 \left[(1+\cos\phi_s)\,\mathrm{e}^{-\Gamma_{\mathrm{L}}^{(s)}t} + (1-\cos\phi_s)\,\mathrm{e}^{-\Gamma_{\mathrm{H}}^{(s)}t} \pm 2\mathrm{e}^{-\Gamma_s t}\sin(\Delta m_s t)\sin\phi_s\right]$
3	$\frac{1}{2}\lvert A_\perp(0)\rvert^2 \left[(1-\cos\phi_s)\,\mathrm{e}^{-\Gamma_{\mathrm{L}}^{(s)}t} + (1+\cos\phi_s)\,\mathrm{e}^{-\Gamma_{\mathrm{H}}^{(s)}t} \mp 2\mathrm{e}^{-\Gamma_s t}\sin(\Delta m_s t)\sin\phi_s\right]$
4	$\frac{1}{2}\lvert A_0(0)\rvert\lvert A_\parallel(0)\rvert\cos\delta_\parallel \Big[(1+\cos\phi_s)\,\mathrm{e}^{-\Gamma_{\mathrm{L}}^{(s)}t} + (1-\cos\phi_s)\,\mathrm{e}^{-\Gamma_{\mathrm{H}}^{(s)}t} \pm 2\mathrm{e}^{-\Gamma_s t}\sin(\Delta m_s t)\sin\phi_s\Big]$
5	$\lvert A_\parallel(0)\rvert\lvert A_\perp(0)\rvert \Big[\frac{1}{2}(\mathrm{e}^{-\Gamma_{\mathrm{L}}^{(s)}t} - \mathrm{e}^{-\Gamma_{\mathrm{H}}^{(s)}t})\cos(\delta_\perp-\delta_\parallel)\sin\phi_s \pm \mathrm{e}^{-\Gamma_s t}(\sin(\delta_\perp-\delta_\parallel)\cos(\Delta m_s t) - \cos(\delta_\perp-\delta_\parallel)\cos\phi_s\sin(\Delta m_s t))\Big]$
6	$\lvert A_0(0)\rvert\lvert A_\perp(0)\rvert \Big[\frac{1}{2}(\mathrm{e}^{-\Gamma_{\mathrm{L}}^{(s)}t} - \mathrm{e}^{-\Gamma_{\mathrm{H}}^{(s)}t})\cos\delta_\perp\sin\phi_s \pm \mathrm{e}^{-\Gamma_s t}(\sin\delta_\perp\cos(\Delta m_s t) - \cos\delta_\perp\cos\phi_s\sin(\Delta m_s t))\Big]$
7	$\frac{1}{2}\lvert A_S(0)\rvert^2 \left[(1-\cos\phi_s)\,\mathrm{e}^{-\Gamma_{\mathrm{L}}^{(s)}t} + (1+\cos\phi_s)\,\mathrm{e}^{-\Gamma_{\mathrm{H}}^{(s)}t} \mp 2\mathrm{e}^{-\Gamma_s t}\sin(\Delta m_s t)\sin\phi_s\right]$
8	$\alpha\lvert A_S(0)\rvert\lvert A_\parallel(0)\rvert \Big[\frac{1}{2}(\mathrm{e}^{-\Gamma_{\mathrm{L}}^{(s)}t} - \mathrm{e}^{-\Gamma_{\mathrm{H}}^{(s)}t})\sin(\delta_\parallel-\delta_S)\sin\phi_s \pm \mathrm{e}^{-\Gamma_s t}(\cos(\delta_\parallel-\delta_S)\cos(\Delta m_s t) - \sin(\delta_\parallel-\delta_S)\cos\phi_s\sin(\Delta m_s t))\Big]$
9	$\frac{1}{2}\alpha\lvert A_S(0)\rvert\lvert A_\perp(0)\rvert\sin(\delta_\perp-\delta_S) \Big[(1-\cos\phi_s)\,\mathrm{e}^{-\Gamma_{\mathrm{L}}^{(s)}t} + (1+\cos\phi_s)\,\mathrm{e}^{-\Gamma_{\mathrm{H}}^{(s)}t} \mp 2\mathrm{e}^{-\Gamma_s t}\sin(\Delta m_s t)\sin\phi_s\Big]$
10	$\alpha\lvert A_0(0)\rvert\lvert A_S(0)\rvert \Big[\frac{1}{2}(\mathrm{e}^{-\Gamma_{\mathrm{H}}^{(s)}t} - \mathrm{e}^{-\Gamma_{\mathrm{L}}^{(s)}t})\sin\delta_S\sin\phi_s \pm \mathrm{e}^{-\Gamma_s t}(\cos\delta_S\cos(\Delta m_s t) + \sin\delta_S\cos\phi_s\sin(\Delta m_s t))\Big]$

Table 3.3: The time dependent amplitudes $\mathcal{O}^{(k)}(t)$ for $B_s^0 \to J/\psi\phi$ decay including S-wave contribution.

CHAPTER 4

The Large Hadron Collider

The LHC (Large Hadron Collider) [1] is the largest particle accelerator in the world. It is located in the CERN laboratory near Geneva, Switzerland. The LHC is designed as two-ring superconducting hadron collider installed in the 26.7 km long tunnel previously occupied by the LEP* collider. The tunnel lies between 45 m and 170 m under the surface and on a plane inclined at a 1.4% slope towards the Léman lake.

4.1 LHC Injection Chain

The LHC is the last step of the complex accelerating chain, which is shown in Figure 4.1. The proton beam starts in the duoplasmatron source, where the hydrogen atoms are ionized by the magnetic field. The resulting ions are injected in to the linear accelerator Linac2, where they are accelerated to 50 MeV The acceleration continues in the Proton Synchrotron Booster (PBS) which accelerates injected protons to 1.4 GeV. Next step in the acceleration chain is the Proton Synchrotron (PS) accelerator, where protons are accelerated to 26 GeV. The last acceleration step before the injection to the LHC is made in the Super Proton Synchrotron (SPS), where the particles are accelerated up to 450 GeV. The bunches of protons are then injected into the LHC ring separately into two counter-circulating beams, where they are accelerated to the final energy.

4.2 LHC Layout

The LHC layout consists of eight sections separated by eight interaction points (IPs). The two counter-circulating beams cross and collide in 4 interaction points, where the ex-

*Large Electron–Positron Collider - the largest electron-positron accelerator ever built.

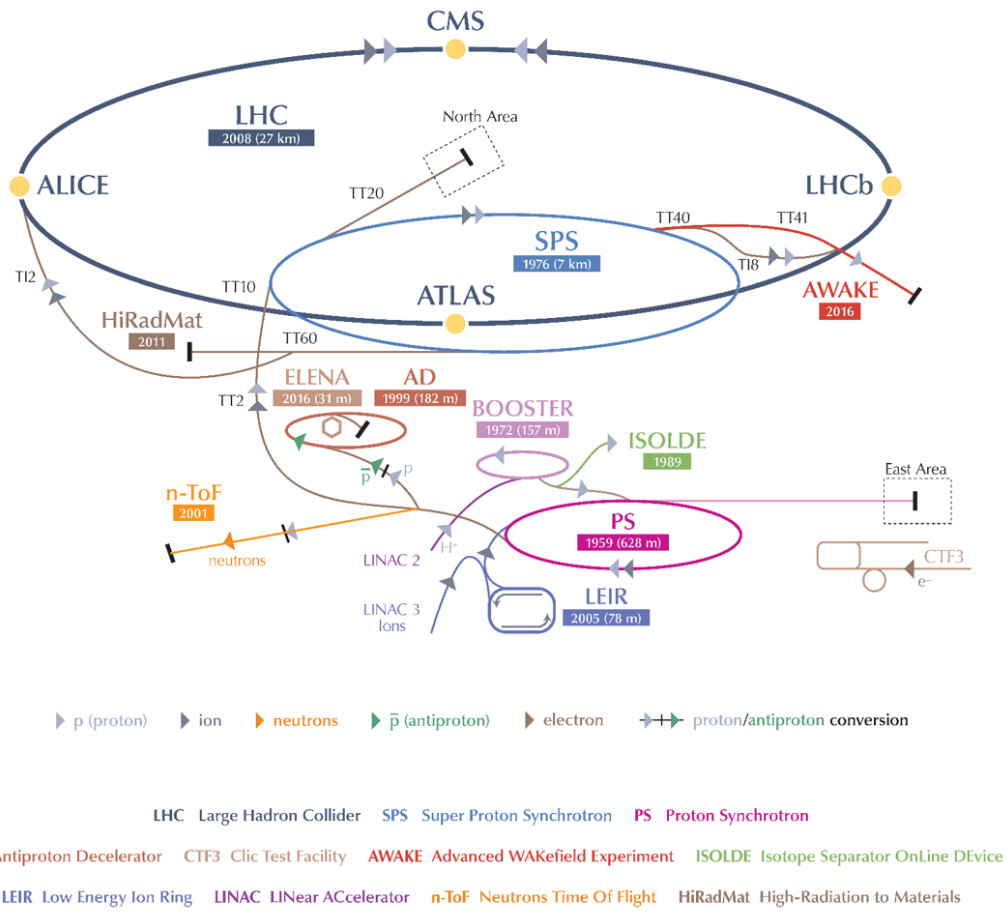

Figure 4.1: The LHC Complex. The complete injection chain is depicted including all pre-accelerators. Image adapted from [38, 39].

periments are located. The two high luminosity experiments, the ATLAS experiment at IP1 and the CMS experiment at IP5, are located at opposite side of the ring. The other two experimental IPs house the ALICE experiment at IP2 and the LHCb experiment at IP8 as well as the injection systems for Beam 1 and Beam 2, respectively. The remaining four IPs do not have beam crossings and house the accelerator equipment: beam collimation and cleaning system at IP3 and IP7, RF beam acceleration system at IP4 and beam dump at IP6, where the beam is extracted from the machine using "kicker" magnets. Figure 4.2 shows a schematic layout of the LHC.

The LHC is effectively a polygon consisting of 184 cells following focusing-defocusing (F0D0) structure. Each cell is 106.9 m long. The F0D0 cell is a magnet structure consisting alternately of focusing (FQ) and defocusing (DQ) quadrupole lenses. Between the focusing magnet elements, the dipole bending magnets (0) and any other machine elements such as

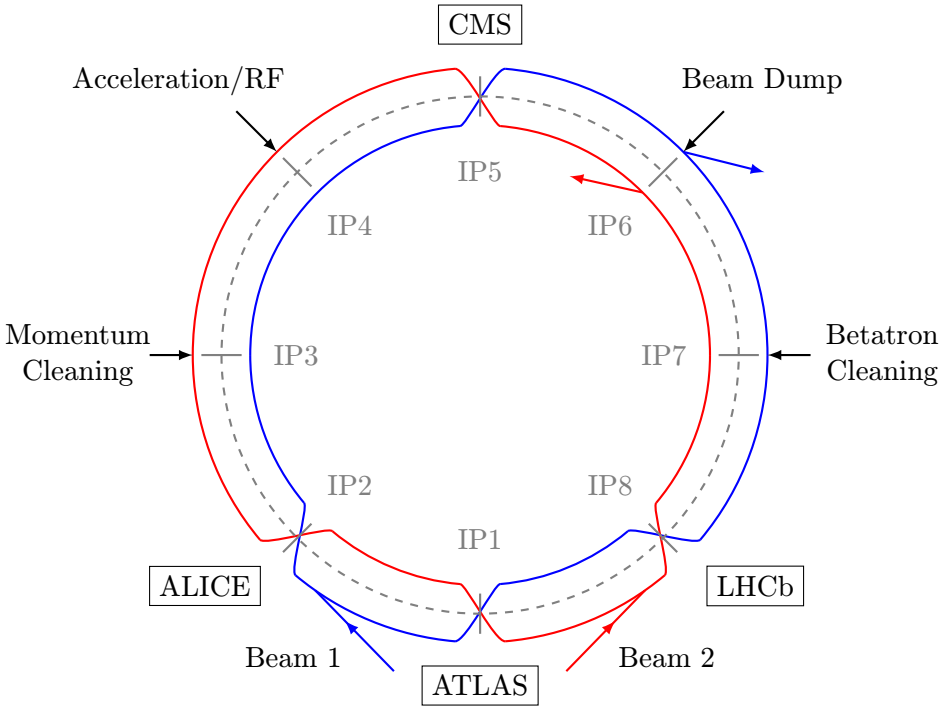

Figure 4.2: Schematic of the LHC layout with marked insertion regions.

orbit corrector dipoles, multipole correction coils and diagnostics elements are installed. Each type of magnet contributes to optimization of beam trajectory. In order to keep particles on the orbit, superconducting dipole magnets are providing 8.33 T field and operate at 1.9 K. The schematic layout of the LHC F0D0 cell is shown in Figure 4.3.

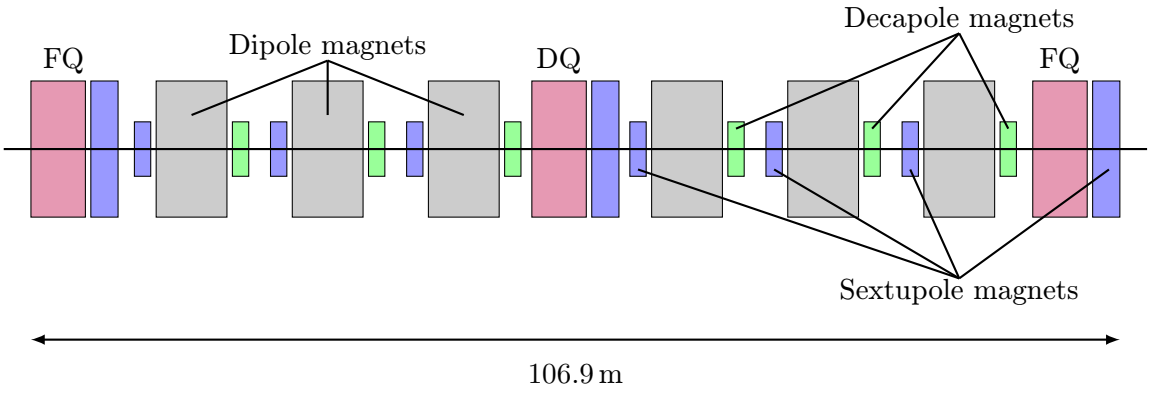

Figure 4.3: Schematic layout of the LHC cell.

4.3 Accelerator Parameters

The most important parameters commonly used to describe accelerator performance are briefly described in this section.

Emittance ϵ is the property of a particle beam that characterizes its spread in $p-x$ phase space. It is an area occupied by a particle beam in a phase space consisting of position and momentum. It is used to describe a beam because unlike the physical dimensions of the beam, which vary with location in an accelerator, emittance is invariant.

Amplitude function $\beta(z)$ is a beam optics quantity which is determined by the accelerator magnet configuration and powering. From the physics point of view, the most important is the value of the amplitude function at the interaction point usually referred to as β^*. The relation between $\beta(z)$ and β^* is defined as follows

$$\beta(z) = \beta^* + \frac{z^2}{\beta^*}, \tag{4.1}$$

where z is the distance along the nominal beam direction.

Crossing angle is the angle between two interacting bunches commonly referred to as θ_c.

4.3.1 Luminosity

Luminosity is a key parameter of each accelerator. This parameter provides the information about the number of collisions produced per second per surface area. In accelerator physics, the luminosity of two Gaussian beams with identical transverse profiles colliding head-on is defined as:

$$\mathcal{L} = \frac{N_1 N_2 f N_b}{4\pi\sigma_x\sigma_y}, \tag{4.2}$$

where the N_1 and N_2 are the numbers of the particles in each of two bunches, f is the collision rate, the N_b is number of bunches in each beam and $\sigma_{x,y}$ are the profiles of the Gaussian beam in vertical and horizontal directions. Luminosity can be expressed in the terms of the beam parameters:

$$\mathcal{L} = F\frac{N_1 N_2 f N_b \gamma}{4\pi\sqrt{\beta_x^*\epsilon_x\beta_y^*\epsilon_y}}, \tag{4.3}$$

where the γ is the relativistic factor, the $\epsilon_{x,y}$ is the emittance of the beam, the $\beta_{x,y}$ is the amplitude function and F is the geometric loss factor resulting from operating with a

crossing angle, θ_c.

Since the luminosity $\mathcal{L}$ is typically a function of time, the integrated luminosity defined as

$$L = \int \mathcal{L}(t)\mathrm{d}t \tag{4.4}$$

is useful to characterize the size of the recorded data sample. At the ATLAS experiment, several types of integrated luminosity can be recognized: **Delivered** luminosity is the luminosity delivered by the accelerator,

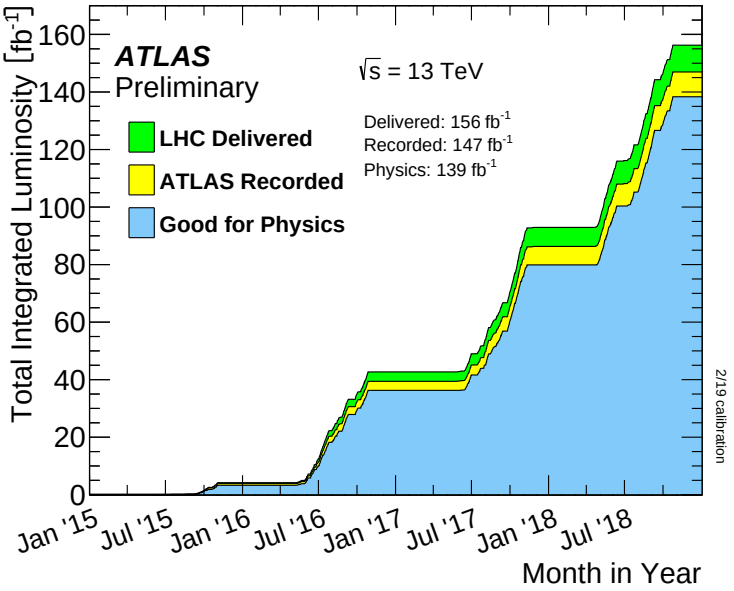

Figure 4.4: Cumulative luminosity versus time delivered to ATLAS (green), recorded by ATLAS (yellow), and certified to be good quality data (blue) during stable beams for pp collisions at 13 TeV centre-of-mass energy in 2015-2018 [40].

Recorded luminosity is the luminosity which was recorded by the experiment and finally the **Good for Physics** is called the luminosity when all reconstructed physics objects are assessed to be of good data quality. The overview of the cumulated luminosity in the LHC Run 2 at the ATLAS detector is shown in Figure 4.4.

4.3.2 Pile-Up

The Pile-Up is the phenomena when more than one pp collision occurs during bunch crossing. The pile-up interactions are independent from each other and the number of pile-up events is characterized by the Poisson distribution with mean μ. The overview of the luminosity-weighted distribution of the mean number of interactions per crossing is shown in Figure 4.5.

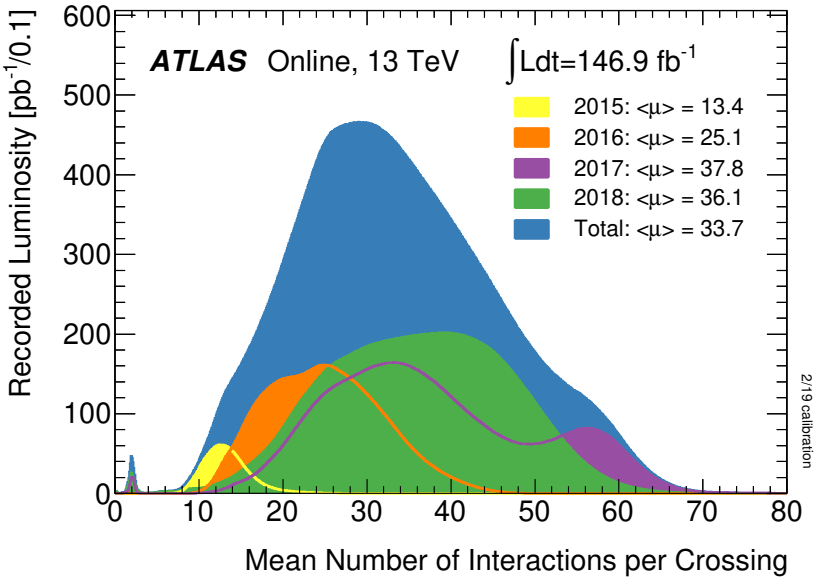

Figure 4.5: The luminosity-weighted distribution of the mean number of interactions per crossing for the pp collisions at 13 TeV centre-of-mass energy in 2015-2018 [40].

4.4 LHC Performance

The LHC is designed to provide proton-proton (pp) collisions with center-of-mass energy $\sqrt{s} = 14\,\text{TeV}$ with a design luminosity of $10^{34}\,\text{cm}^{-2}\,\text{s}^{-1}$ and bunch collision rate of 40 MHz. However, during the first run commissioning period, the LHC was operating at lower energy of $\sqrt{s} = 7\,\text{TeV}$ in 2011 and $\sqrt{s} = 8\,\text{TeV}$ in 2012. The achieved collision rate of 20 MHz, which corresponds to 50 ns bunch spacing was also lower than designed one.

During the first long shutdown in 2013 and 2014, the apparatus has undergone considerable improvements which enable higher energies and collision rate of 40 MHz. Because of slow progress with training of superconducting magnets it was decided that the LHC will run in Run 2 at $\sqrt{s} = 13\,\text{TeV}$, almost design energy. The LHC had to deal with several operational inconveniences and upgrades during Run 2 leading to change of the operation conditions. The first inconvenience was in 2016 due to a vacuum leak in the SPS beam dump, which limited the bunch-train to 144 bunches per injection. During 2016, a new type of the LHC beam was tested based on Bunch Compression Merging and Splitting (BCMS), which reduced the beam emittance for the same beam intensity. In the beginning of 2017, the BCMS beam was used; however, replacing a magnet during the winter stop caused abnormal background radiation and sudden beam losses. Therefore, alternative beam filling scheme 8b4e (later 8b4e-BCS) was introduced, reducing the probability of the beam loss. In 2018, almost all operation troubles were solved and LHC was running

without any major issues. The summary of the main physics parameters of the LHC during Run 1 and Run 2 operation can be found in the Table 4.1. In comparison with designed values, some parameters are above its design value which brings many challenges to the experiment reconstruction and trigger system.

	Beam type:	E_B TeV	B.S. ns	N_p 10^{11}	N_B -	$\mathcal{L}$ $10^{34}\,\mathrm{cm}^{-2}\,\mathrm{s}^{-1}$	$\langle\mu\rangle$ -	β^* m
Design	Std	7	25	1.15	2808	1	20	0.55
2011	Std	3.5	50	1.45	1380	0.37	17	1.5/1
2012	Std	4	50	1.7	1380	0.77	37	0.6
2015	Std	6.5	25	1.15	2244	0.55	15	0.8
2016	Std/BCMS	6.5	25	1.2	2040/2076	0.83/1.4	20/35	0.4
	BCMS	6.5	25	1.2	2556	1.74	45	0.4
2017	8b4e	6.5	25	1.2	1916	1.9	70/60	0.4/0.3
	8b4e-BCS	6.5	25	1.25	1868	2.06/1.5	80/60	0.3
2018	BCMS	6.5	25	1.1	2556	2.1	60	0.3/0.25

Table 4.1: Summary of the main LHC beam and machine parameters for Run 1 and Run 2 at IP1, where the B.S. denotes bunch spacing, $\langle\mu\rangle$ is mean number of multiple pp interactions per bunch crossing, β^* stands for the optical β function, N_B is total number of bunches, E_B is beam energy, N_p is number of protons per bunch and $\mathcal{L}$ is peak luminosity [41, 42, 43, 44].

The LHC produced $29\,\mathrm{fb}^{-1}$ of integrated luminosity at Run 1 and $156\,\mathrm{fb}^{-1}$ of integrated luminosity during Run 2 resulting in a total of $185\,\mathrm{fb}^{-1}$ of integrated luminosity of high energy pp collisions.

CHAPTER 5

ATLAS Detector

The ATLAS (A Toroidal LHC ApparatuS) detector [2], shown in Figure 5.1, is general-purpose detector designed to study pp collisions at the LHC. The main area of research is Standard Model measurement, dedicated top quark studies, precise study of electroweak theories, SUSY (supersymetry), and searches for any new physics.

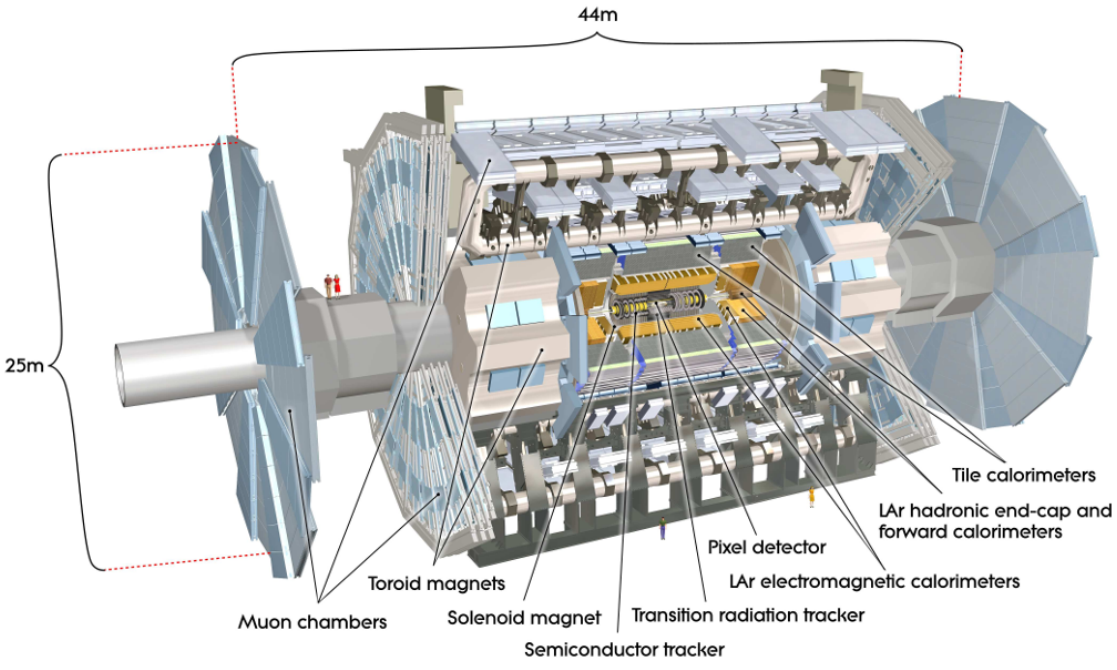

Figure 5.1: ATLAS detector cut-away view with its subdetectors highlighted [2].

In 2012, ATLAS and CMS collaborations announced the discovery of the Higgs boson with a mass of $(125.9 \pm 0.4)\,\text{GeV}$. The ATLAS subdetectors cover almost full solid

angle around the collision point and are symmetric in the forward-backward direction with respect to the interaction point. The subdetectors can be geometrically divided into barrel section, two end-caps and two forward regions. In the forward region there can be found ALFA, LUCID and ZDC sub-detectors which primary serve for luminosity measurement. The non-forward subdetectors can be divided into three sections: inner detector (ID), calorimetry systems and muon spectrometer (MS). The detectors are immersed in the magnetic field that bends charged particle trajectories and allows momentum measurement [2].

5.1 Coordinate System

The coordinate system describing the detector phase space is usually set up with the z-axis parallel to the beam direction and the x-y plane perpendicular to the beam direction. The variables measured in the transverse plane are denoted with a T subscript. The positive x-axis is defined as pointing from the interaction point to the center of the LHC ring, the positive y-axis is defined as pointing upwards. The positive direction of z-axis is defined so as to create the right-handed coordinate system.

For the track measurement, it is easier to determine the azimuthal angle Φ, which is measured around the beam axis, and the polar angle Θ, which is an angle between the beam axis and the measured point. Using this phase space description, the following terms are introduced.

The pseudorapidity is defined as

$$\eta = -\ln \tan \frac{\Theta}{2}. \tag{5.1}$$

In the case of massless nonrelativistic objects, the pseudorapidity is equal to the rapidity

$$y = \frac{1}{2} ln \frac{E + p_z}{E - p_z}. \tag{5.2}$$

The distance ΔR in the pseudorapidity-azimuthal angle space is defined as

$$\Delta R = \sqrt{\Delta\eta^2 + \Delta\Phi^2}. \tag{5.3}$$

5.2 Magnet System

The ATLAS magnet system is unique with respect to other experiments at the LHC and is necessary for the momentum measurement of charged particles. As shown in Figure 5.2, the ATLAS magnet system is composed of four parts: central solenoid, barrel toroid and

two end-cap toroids [45].

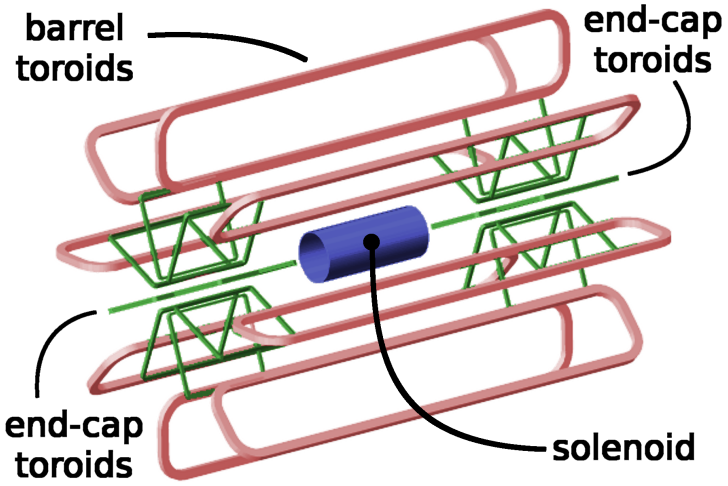

Figure 5.2: The schematic view of the ATLAS magnet system layout which consist of the central solenoid, barrel toroid and two end-cap toroids [46].

The central solenoid [47] is designed to provide 2 T magnetic field in central tracking region. To achieve that, the superconducting solenoid with radius 1.247 m and length of 5.283 m is used. In the nominal state, the coil is supplied with 7730 A and the whole solenoid is cooled down to 4.5 K using liquid helium as a coolant. To reduce the detector material budget, the central solenoid and the electromagnetic calorimeter share a common cryostat.

The barrel toroid, providing the magnetic field in the outer tracking region, consists of 8 flat superconducting race-track coils, each 25.3 m long and 5 m wide, grouped in a torus shape with inner bore of 9.4 m and outer diameter of 20.1 m. The nominal magnetic field for the muon detectors in the central region is 0.5 T, with peak field strength of 2.5 T in the bore. The supply current is 20.5 kA and the operation temperature is 4.7 K.

The end-caps toroids, positioned inside the barrel toroid at both ends of the central solenoid, provide the azimuthal magnetic field across a radial span of 1.5–5 m. The toroids generate the magnetic field required for optimizing the bending power in the end-cap regions of the muon spectrometer system. The nominal magnetic field for the muon detectors in the end-cap region is 1.0 T, with peak field strength of 3.5 T in the bore.

5.3 Inner Detector

The inner detector is designed to provide an excellent momentum resolution for charged particles and both primary and secondary vertex position measurements with high precision in the pseudorapidity range of $|\eta| < 2.5$. The ID has to withstand high-radiation environment as the innermost subsystem of the ATLAS detector.

The ID is contained within a cylindrical envelope of a length of $\pm 3512\,\text{mm}$ and with a radius of 1150 mm. It is immersed in a 2 T magnetic field generated by the central superconducting solenoid. The ID consists of a silicon pixel detector, a silicon strip detector (SCT) and a transition radiation tracker (TRT).

As can be seen in Figure 5.3, the detectors are arranged as concentric cylinders around the beam axis in the barrel region. In the end-cap regions, there are pixel modules located on disks perpendicular to the beam axis. All detectors are mounted on a support structure, which is made of carbon fibers to ensure good mechanical properties, thermal conduction and low material budget.

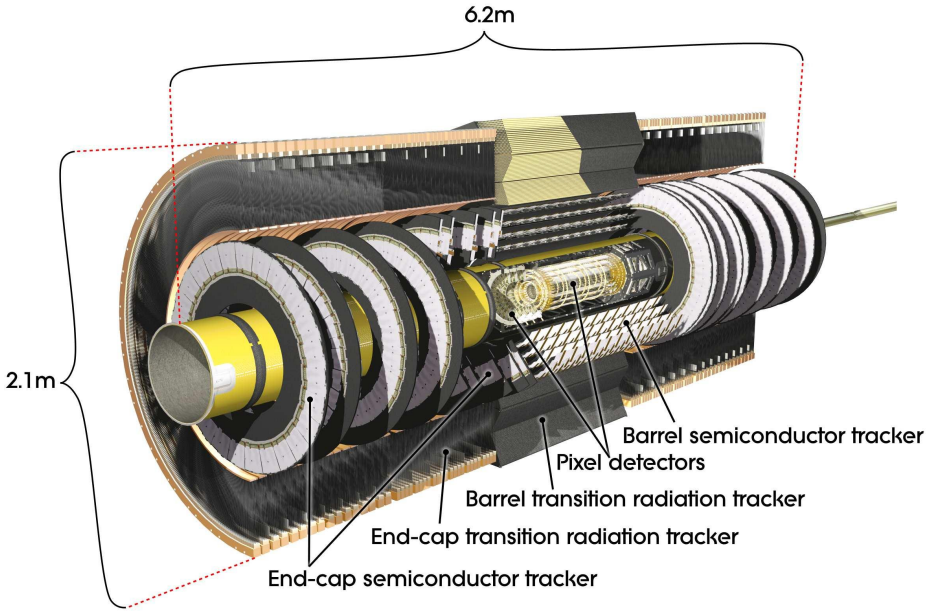

Figure 5.3: The schematic cut-away view of ATLAS inner detector [2].

5.3.1 Pixel Detector

The Pixel detector is the closest detector system to the interaction point and contains four layers of the pixel modules in the barrel region. The innermost layer was added during the first long shutdown (LS0), which occurred between years 2013 and 2015. This layer

is placed between new smaller beryllium beampipe with a radius of 25 mm and previous innermost layer called B-layer. This new layer is than referred as Insertable B-layer (IBL). Two end-caps regions are equipped with three disk layers each.

Pixel Sensors

The original layers (without IBL) are equipped with silicon pixel detectors using $n^+-\text{on}-n$ silicon with p-spray technology and a nominal pixel size of $50 \times 400\,\mu\text{m}^2$. The sensor thickness is approximately 250 µm. Silicon pixel sensors use planar technology with oxygenated n-type wafers and are read out on the n^+ -implanted side of the sensor. The opposite side of the electrodes is in contact with a p^+ layer. Each pixel sensor is bump-bonded through hole in the sensor passivation layer to the front-end readout chip FE-I3. The pixel detector provides approximately 80.4 million readout channels in total. Schematic view of a pixel module is shown in the Figure 5.4.

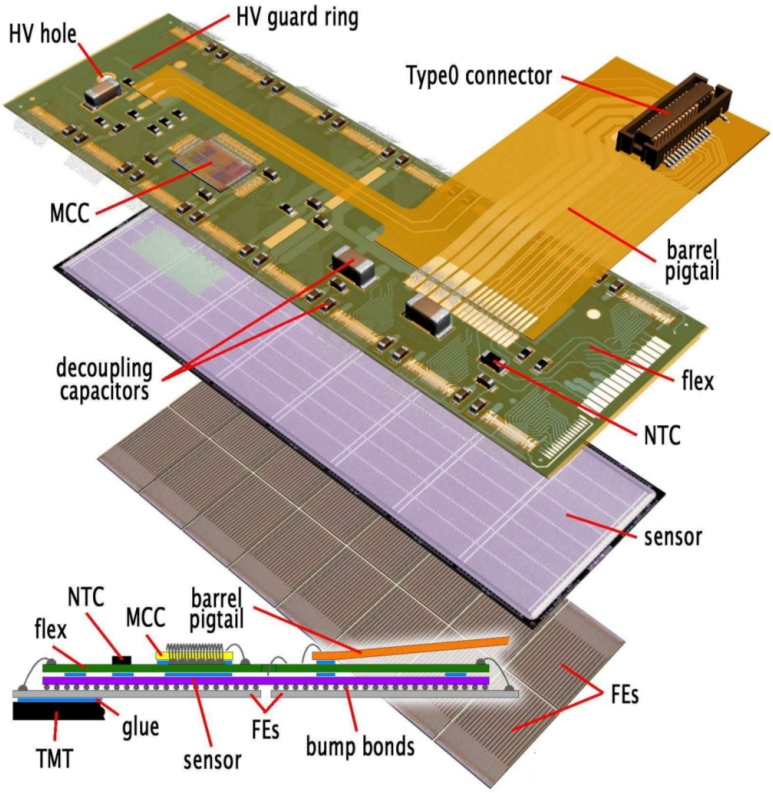

Figure 5.4: Schematic view of a barrel pixel module illustrating the major pixel hybrid and sensor elements, including the MCC (module-control chip), the front-end (FE) chips, the NTC thermistors, the high-voltage (HV) elements and the Type0 signal connector [2].

IBL Pixel Sensors

This IBL is equipped with new sensors using planar $n^+-\text{in}-n$ and 3D double-sided $n^+-\text{in}-p$ technology and in total it adds 12 million channels to the existing Pixel Detector. These sensors have finer granularity of $50 \times 250\,\mu\text{m}^2$ and besides higher radiation tolerance, new readout chip FE-I4 has lower noise and power consumption. The IBL will further improve tracking robustness, vertexing and b tagging performance. During Run 2 data taking with pp collisions at $\sqrt{s} = 13\,\text{TeV}$, the data measured by the IBL are in agreement with simulations and thus IBL proved its good performance [48]. The improvement of primary vertexing is most significant in the precision of transverse impact parameter $\sigma(d_0)$ (Figure 5.5) which improved almost twice compared to 8 TeV measured without IBL. The other property important for the B-Physics measurement is the time resolution σ_t. The significant improvement of time resolution with IBL can be seen in Figure 5.6, where the data are compared with planned inner tracker upgrade (ITk).

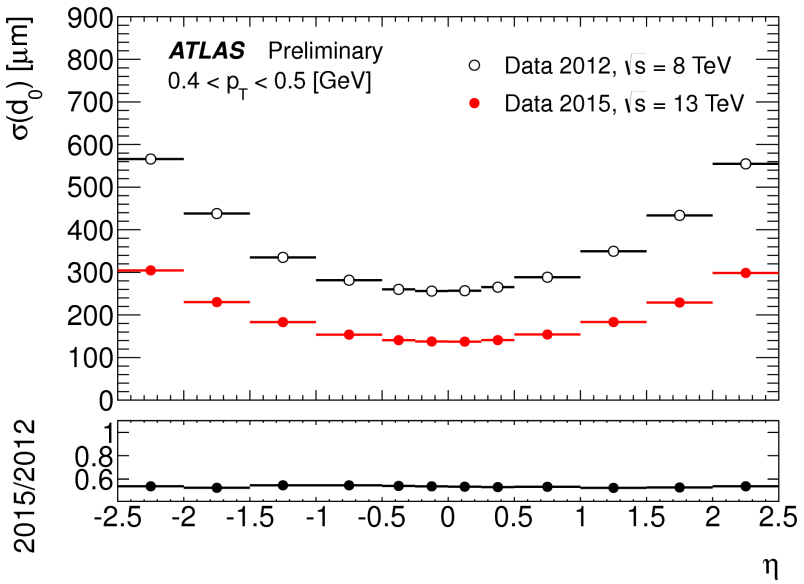

Figure 5.5: Unfolded transverse impact parameter resolution measured in 2015 at $\sqrt{s} = 13\,\text{TeV}$, with the Inner Detector including the IBL The plots are shown as a function of η, for values of $0.4 < p_\text{T} < 0.5\,\text{GeV}$ compared to that measured from data in 2012, $\sqrt{s} = 8\,\text{TeV}$ [49].

5.3.2 SCT Detector

SCT detector consist of four layers of double detectors in the barrel region and two endcap regions, each containing nine layers. Layers are equipped by modules which consist of 80 µm pitch micro-strip sensors with thickness $285 \pm 15\,\mu\text{m}$, providing $\text{R} - \Phi$ coordinates.

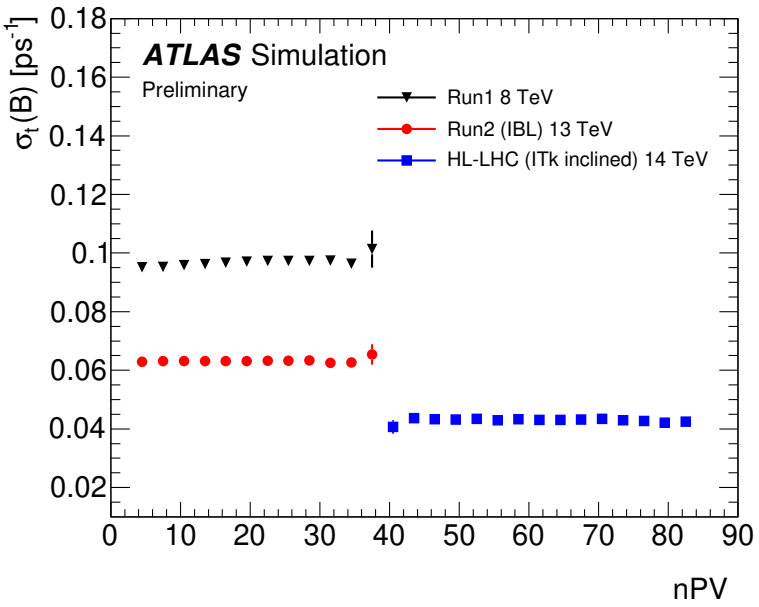

Figure 5.6: Stability of the B_s^0 proper decay time resolution σ_t against the number of reconstructed primary vertices (nPV) [50].

Every two sensor modules are glued together in the barrel region within a hybrid module. On one detector layer, there are 2 sensor layers rotated within their hybrids by ±20 mrad around the geometrical center of the sensor to measure both R − Φ × z coordinates. The 2D space-point resolution is 17 µm in $R - \phi$ plane and 580 µm in $z(r)$.

For reason of cost, reliability and milder radiation conditions, the sensors of SCT use classic single-sided p$^+$-in-n technology. The sensors are connected to a binary signal readout chips. In total, the SCT provides approximately 6.3 million readout channels.

5.3.3 Transition Radiation Tracker

Main purpose of TRT is to measure transition radiation of charged particles, in order to distinguish between light electrons and other heavier particles, in the pseudorapidity range of $|\eta| < 2.0$. The basic TRT detector elements are polyamide drift straw tubes with diameter of 4 mm filled by special gaseous mixture. The straw tube walls operates as cathodes, while the 31 µm thick tungsten wire plated with 0.5–0.7 µm layer of gold operates as anode.

The TRT consist of 73 layers of straws in the barrel region and 160 straw planes in end-cap. Typically, the TRT gives 36 hits per track, but it provides only R − Φ information. The total number of readout channels of TRT is approximately 351,000.

5.4 Calorimetry

Calorimetry system is designed to provide good energy resolution for measurement of electromagnetic and hadronic showers, and it must also limit punch-through into the muon system. Calorimetry system consist of two separate calorimeters using different designs suited to the widely varying requirements of the physics processes of interest, and it cover region up to $|\eta| < 4.9$. Over the η region matched to the inner detector, the fine granularity of the EM calorimeter is ideally suited for measurements of electrons and photons. There is coarser granularity in the rest of the detector, but calorimeters are precise enough to satisfy the physics requirements for jet reconstruction and E_T^{miss} measurement.

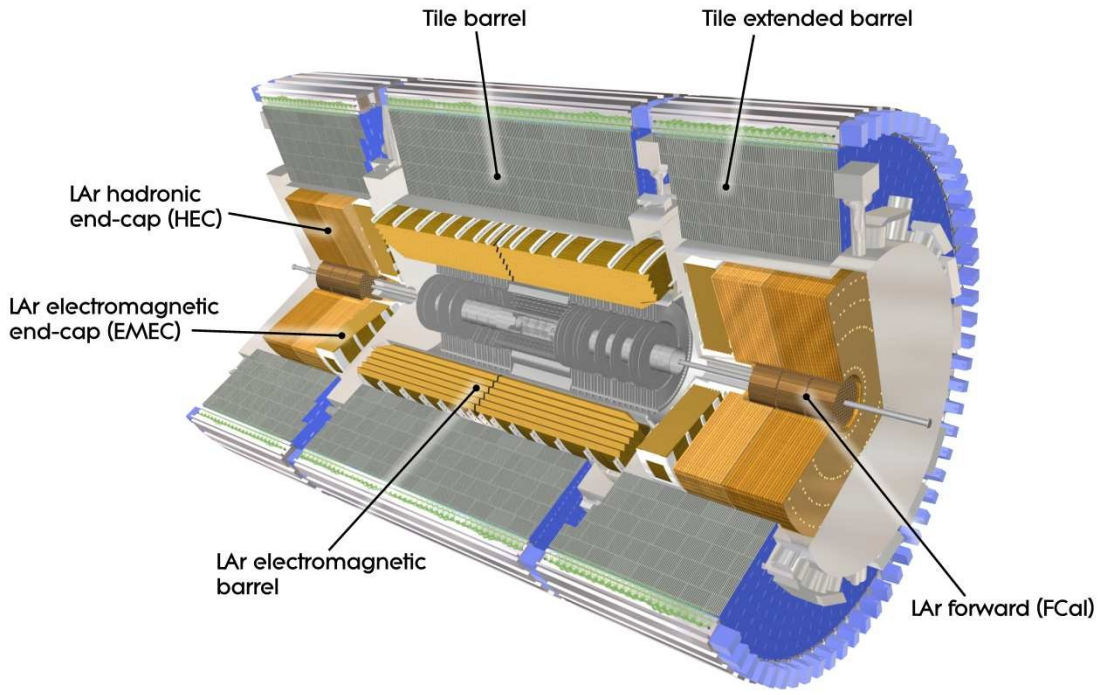

Figure 5.7: ATLAS calorimetry system cut-away view [2].

5.4.1 Electromagnetic Calorimeter

The Electromagnetic calorimeter (ECAL) at ATLAS is lead-liquid argon (LAr) detector with accordion-shaped kapton electrodes and lead absorber plates covering full ϕ range without azimuthal cracks. The ECAL is divided into a barrel part ($|\eta| < 1.475$) and two end-cap parts ($1.375 < |\eta| < 3.2$). The barrel calorimeter consists of two identical half-barrels, separated by a 4 mm gap at $z = 0$. Each end-cap calorimeter is mechanically divided into two coaxial wheels: an outer wheel covering the region $1.375 < |\eta| < 2.5$, and

an inner wheel covering the region $2.5 < |\eta| < 3.2$. The readout electrodes are located in the gaps between the absorbers and consist of three conductive copper layers separated by insulating polyamide sheets. The overal thickness of the ECAL is between 22 and 24 radiation lengths.

5.4.2 Hadronic Calorimeter

To ensure the proper reconstruction of hadronic showers and maximal phase-space coverage, the hadronic calorimeter is divided into three parts: tile calorimeter in barrel, LAr hadronic calorimeter in end-cap regions and LAr forward calorimeter.

Tile Calorimeter

The tile calorimeter is placed directly outside the EM calorimeter envelope as can be seen in Figure 5.7. It consist of barrel part covering the region $|\eta| < 1.0$ and two extended barrel parts covering the region $0.8 < |\eta| < 1.7$. Scintillator tile calorimeter (TileCal) is a sampling calorimeter using steel as the absorber and plastic scintillating tiles as the active material. Two sides of the scintillating tiles are read out by wavelength shifting fibers into two separate photomultiplier tubes. The overall thickness of the tile calorimeter is 9.7λ at $\eta = 0$.

LAr Hadronic End-Cap Calorimeter

The Hadronic End-cap Calorimeter (HEC) is located directly behind the end-cap electromagnetic calorimeter and covers the region of $1.5 < |\eta| < 3.2$. Each HEC consists of two independent wheels composed of copper-LAr calorimeters of flat-plate design with outer diameter of 2.03 m. The wheels closest to the interaction point are built from 25 mm parallel copper plates, while those further away use 50 mm copper plates. The copper plates are separated by 8.5 mm gaps filled with LAr, providing the active medium for this sampling calorimeter.

LAr Forward Calorimeter

The Forward Calorimeter (FCal) cover region of $3.1 < |\eta| < 4.9$ and is designed to provide both electromagnetic and hadronic calorimetry information. The FCal consists of three modules in each end-cap: the first, made of copper, is optimised for electromagnetic measurements, while the other two, made of tungsten, measure mainly the energy of hadronic interactions. The FCal modules consists of a metal matrix parallel to the beam axis consisting of concentric rods and tubes, where the LAr, filled in the gap between them, is the sensitive medium. The overall length of FCal is 10λ.

5.5 Muon Spectrometer

The muon system is designed to detect charged particles exiting the barrel and end-cap calorimeters, and to measure muon momentum in the pseudorapidity range of $|\eta| < 2.7$. It measures properties of muon tracks bent by the large superconducting air-core toroid magnets. Detectors are situated in the barrel, end-cap and also in the transition regions ($1.4 < |\eta| < 1.6$), where the tracks are bent by combination of barrel toroid and end-cap magnets. In the barrel region, tracks are measured in chambers arranged in three cylindrical layers around the beam axis, while in the transition and end-cap regions, the chambers are installed also in three layers in planes perpendicular to the beam axis. Over most of the η-range, a precision measurement of the track coordinates is provided by the Monitored Drift Tubes (MDT). At large pseudorapidities, the Cathode Strip Chambers (CSC) with higher granularity are used to withstand demanding rate and background conditions.

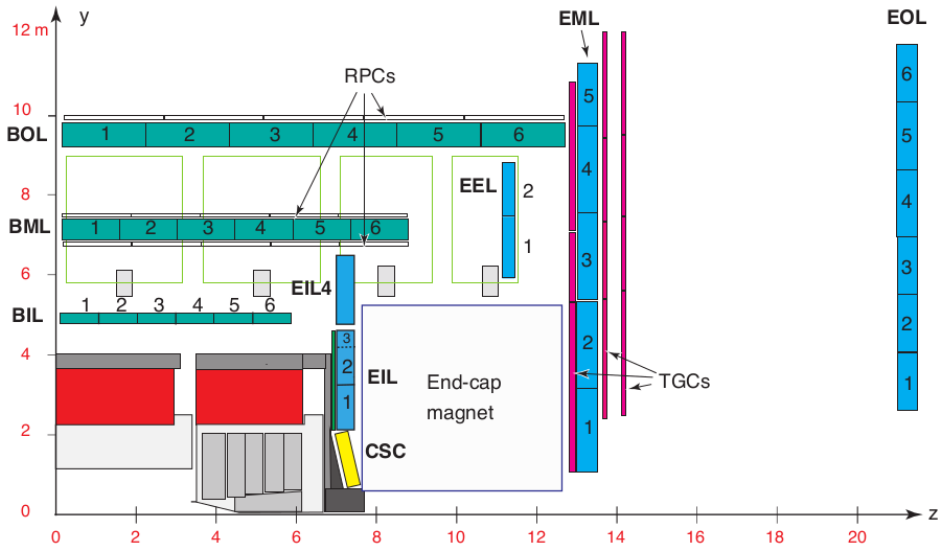

Figure 5.8: Cross-section of the quadrant of the muon system in a plane containing the beam axis. The MDT chambers in the barrel are arranged in three concentric cylindrical shells around the beam axis. In the end-cap region, muon chambers form large wheels, perpendicular to the z-axis. In the forward region, CSC is used in the innermost tracking layer. The RPC and TGC chambers are arranged in three layers (called stations) as indicated in the Figure [2].

The pseudorapidity range of $|\eta| < 2.4$ is covered by an additional muon chambers also serving as a trigger system which is equipped with Resistive Plate Chambers (RPC) in the barrel ($|\eta| < 1.05$) and Thin Gap Chambers (TGC) in end-cap ($1.05 < |\eta| < 2.4$)

regions, respectively. The main purpose is to provide fast track information for triggering purposes with a well-defined p_{T} thresholds. The cross-section of the quadrant of the muon system is shown in Figure 5.8.

5.5.1 Monitored Drift Tubes

The basic detection element of the MDT chamber is an aluminum drift tube with a diameter of 29.6 mm, pressurized with Ar/CO_2 (93/7%) gas at 3 bar. The central wire with a diameter of 50 µm, made of tungsten-rhenium alloy is used for the collection of electrons created by the ionization of the gas by incoming particles. The drift tube operates at 3080 V potential difference between wire and tube wall producing the field with a maximum drift time from the wall to the wire about 700 ns. The spatial hit resolution for the MDT tubes is about 60–80 µm.

The MDT chambers in the barrel are arranged in three concentric cylindrical shells around the beam axis covering the region $|\eta| < 1.4$. In the end-cap region, muon chambers form large wheels, perpendicular to the z-axis covering the range of $1.4 < |\eta| < 2.7$. All regular MDT chambers consist of two groups of tube layers, called multi-layers, separated by a mechanical spacer. The multi-layer consist of four tube layers in the innermost shell to enhance the pattern-recognition performance, while the middle and outer shell uses only three tube layers.

5.5.2 Cathode Strip Chambers

The CSC are the multi-wire proportional chambers with wires of 30 µm diameter oriented in the radial direction. The wire pitch is equal to the anode-cathode spacing of 2.5 mm and in the bending direction, the CSC reaches a resolution of 60 µm per CSC plane. The operating voltage of 1900 V provide the maximal electron drift time lower than 40 ns resulting in a timing resolution of about 7 ns per plane.

The CSC chambers are used in the forward region $2 < |\eta| < 2.7$, where the track occupancy is higher than safe operation limit of the MTD's. The CSCs combine high spatial, time and double track resolution with high-rate capability and low neutron sensitivity. The whole CSC system consists of two disks with eight chambers each. Each chamber contains four CSC planes resulting in four independent measurements in η and ϕ along each track.

5.5.3 Resistive Plate Chambers

The RPC is a gaseous parallel electrode-plate detector used to provide trigger information in the barrel region. The RPC module is made of two phenolic-melaminic plastic laminate

plates separated by 2 mm insulating polycarbonate spacers, and filled with the mixture of $C_2H_2F_2$/Iso$-$ C_4H_{10}/SF_6 (94.7/5/0.3%) gases. The potential difference between the plates of 4.9 kV mm^{-1} allows the detector to work in the avalanche mode. The signal is read out by the metallic strips, which are installed on the outer side of the resistive plates.

The RPC are in the barrel arranged in three concentric cylindrical layers around the beam axis covering the region $|\eta| < 1.05$. The two inner layers provide the information for low-p_{T} triggers using tracks in the range of 6–9 GeV, while the outer layer measures the high momentum tracks in the range of 9–35 GeV seeding the high-p_{T} triggers. Each RPC station is made of two detector layers and four readout strip panels, each measuring the track η and ϕ.

5.5.4 Thin Gap Chambers

The TGC's are multi-wire proportional chambers designed to provide muon trigger information in the end-cap region and the measurement of the azimuthal coordinate. The TGC's are characteristic that the wire-to-cathode distance of 1.4 mm is smaller than the wire-to-wire distance of 1.8 mm. The cathode plates are made of FR4 (Flame Resistant 4) with a graphite coating on the inside. The gap between two plates is filled with a highly quenching gas mixture of CO_2 and $\mathrm{n}-C_5H_{12}$. The nominal operation voltage is 2900 V which provides high electric field around the TGC wires and together with the small wire-to-wire distance leads to very good time resolution of 4 ns.

The TGCs detectors are mounted in two concentric rings, one in the innermost layer marked layer I and the rest in the middle layer marked TGC1-3. Each layer is divided into the outer ring covering the rapidity range of $1.05 < |\eta| < 1.92$, and the inner ring covering the rapidity range of $1.92 < |\eta| < 2.4$. The TGC units are grouped into triplet and doublet modules. The triplet module is build to cope with false coincidences from background hits, which are more likely in the end-cap region than in the barrel.

5.6 Forward Detectors

The forward detectors are placed at high pseudorapidies and their primary objective is to measure a beam luminosity for the ATLAS detector. Furthermore, in conjunction with the main ATLAS detector body they are used to study soft QCD and diffractive physics in the initial low luminosity phase of ATLAS running. All of these detectors use different techniques to detect fragments from the collisions. The location of the ATLAS forward detectors is shown in Figure 5.9.

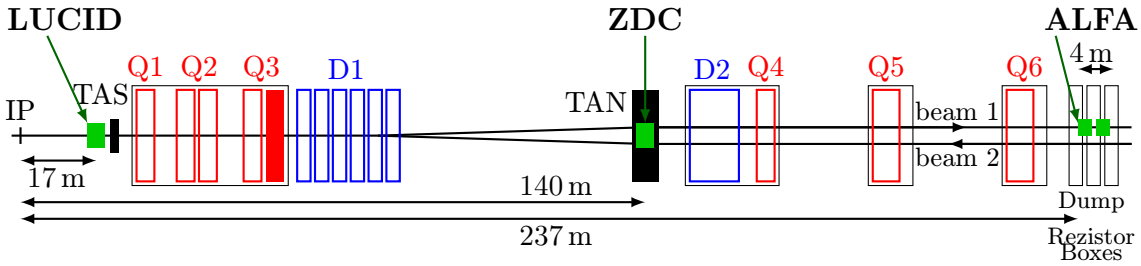

Figure 5.9: The placement of the ATLAS forward detectors with respect to IP1 [51].

5.6.1 LUCID-1 and LUCID-2 Detectors

The LUCID (Luminosity measurement using Čerenkov Integrating Detector) is composed of two modules located at $\pm 17\,\mathrm{m}$ from the interaction point that provide a coverage $5.5 < |\eta| < 5.9$ for charged particles. The main intent of LUCID is to measure ATLAS luminosity using the inelastic collision products with sufficient efficiency and low sensitivity to the background [52]. In the Run 1, the LUCID-1 was used for a luminosity measurement; however, the increased pile-up and reduced bunch spacing in Run 2 needed a faster and more radiation hard detector with sensors of smaller acceptance and, in general better stability. Thus for Run 2, the upgraded detector LUCID-2 was used.

At the LUCID-1, each arm was equipped with twenty projective aluminum tubes filled with C_4F_{10} gas at a constant pressure of 1.2–1.4 bar, providing a Čerenkov threshold of 2.8 GeV for pions and 10 MeV for electrons where the tubes surround the beam-pipe and point towards interaction point.

The LUCID-2 was installed during LS 1. It was decided to use gas-less system with 16 photo multipliers (PMs) at each arm. The PMs contain thin quartz windows as Čerenkov medium and a small amounts of radioactive ^{207}Bi source deposited on the windows for monitoring and calibration purpose. The precision of luminosity measurement in Run 2 with upgraded LUCID-2 detector is $\sim 2\%$ [53].

5.6.2 ZDC (Zero Degree Calorimeter)

The ZDC provides coverage of the region $|\eta| > 8.3$ for neutral particles and is placed at two symmetric arms at 140 m from the interaction point. The ZDC plays important role in the heavy ion physics program at the LHC. It is used for the centrality measurement, which is strongly correlated with the number of very forward neutrons.

The ZDC is a sampling calorimeter that uses Čerenkov light detection produced by the highly energetic charged particles in the shower. The active element is made of quartz rods and the light produced in the rods is detected by photo multiplier tubes. The tungsten

plates are used as an absorber. The time resolution of the ZDC is about 100 ps, which is sufficient to locate the interaction point to about 3 cm along the beam axis [54].

5.6.3 ALFA (Absolute Luminosity for ATLAS)

The ALFA is located at ±240 m from the interaction point on both sides of the ATLAS. It is designed to measure protons scattered at very small angles used for studies containing elastic and diffractive events, exclusive production and photon-induced interactions.

The whole detector is placed in the specialized retractable devices called Roman pots which allows to have the detector in the primary vacuum of the LHC and only a minimal amount of insensitive material towards the beam to avoid acceptance losses. The schematics view of the ALFA detector placed in the Roman pot is shown in Figure 5.10. At the beginning of the run, the ALFA detectors are in withdrawn position far from the beam and after the beam has stabilized, the detectors are moved back to within 1.5 mm of the beam.

The detector is based on staggered layers of square-shaped scintillating fibers, read out by Multi-Anode Photo-Multiplier Tubes (MAPMTs). These fibers are made of organic scintillators with fast decay time of 2.8 ns; however, they provides low radiation tolerance. The MAPMT technology allows to readout the relatively large number of scintillating fibers [55].

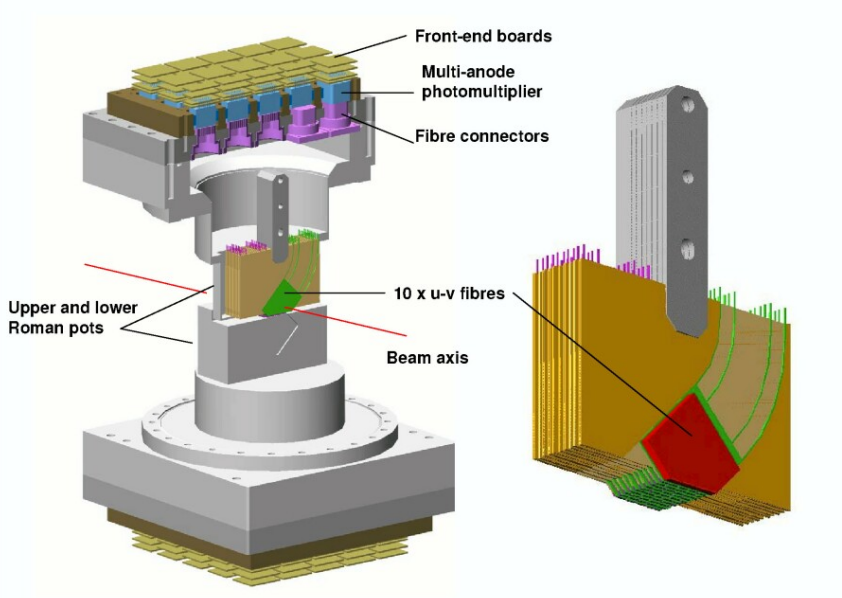

Figure 5.10: Schematics of ALFA detector and special retractable devices called Roman pots [56].

CHAPTER 6

ATLAS Software and Computing Tools

6.1 ATLAS Offline Software

The core of ATLAS offline software consist of the Athena [57] framework with libraries developed within the framework to support specific tasks of the analysis and event reconstruction. It contains over 2000 individual software packages and external dependencies, including over 100 additional software packages including HepMC or Geant4. The candidate reconstruction and event selection is done in the Athena producing the output data files processed by analysis software in following processing steps.

The analysis software is then implemented in C++, Python and ROOT [58] with usage of RooFit [59] and RooStats frameworks. In general, the ROOT and Athena framework are well connected, but they can be used independently.

6.1.1 Athena

Athena is the object oriented control framework, mainly written in C++ and Python, used by the ATLAS experiment, which is based on the Gaudi architecture. The Gaudi framework, originally developed by LHCb, is now also shared by ATLAS, GLAST, HARP and OPERA. It is used as a common framework for detector performance and physics studies. The main components of the Athena framework are: *Application Manager*, *Event Data Service*, *Algorithms*, *Helpers* and *Tools*. It provides functionality for the reconstruction, simulation, analysis tools and high level trigger (HLT) control.

The framework is designed to maintain a strict separation between transient and persis-

tent data. This allows individual components to be easily replaced as technologies evolve, which is essential for an experiment which will run for several decades.

6.1.2 ROOT

ROOT is an object oriented analysis tool for data processing developed at CERN and is available under the LGPL license. ROOT uses C++ syntax and provides an advanced statistical analysis and visualization tools. The ROOT framework provides containment for analysis processing and storage of analysis results in the proprietary ROOT tree structure. It also allows usage of parallel computing tools for effective processing of large data files. The analysis presented here is processed using the ROOT version 6.14/04.

RooFit packages provides a toolkit for modeling the expected distribution of events in a physics analysis. Models can be used to perform likelihood fits, produce plots, and generate "toy Monte Carlo"* samples for various studies. The RooFit tools are integrated with the object-oriented and interactive ROOT graphical environment. RooFit was originally developed for the BaBar collaboration, a particle physics experiment at the Stanford Linear Accelerator Center. The software is primarily designed as a particle physics data analysis tool, but it could be used as powerful tool for other types of data analysis.

RooStats is a package which provides statistical tools built on top of RooFit and distributed in ROOT. It is a joint project between the LHC experiments and the ROOT team used for the statistical evaluation of the hypothesis testing and other statistical evaluation.

6.2 ATLAS Event Data Model

The first data-taking run (Run 1) of the ATLAS experiment used complicated Event Data Model (EDM), and even though it was very successful, for the Run 2 the EDM underwent substantial changes. One of the large disadvantage of the EDM from Run 1 was that the event data could not be easily converted directly into ROOT format. Additionally, ATLAS needs some kind of robust, flexible data-reduction framework to reduce required disk space. To deal with this, ATLAS converted on output the complex transient data model to a simpler persistent data model which could be written to ROOT directly. This new ATLAS event data model for analysis is called the xAOD (Analysis Object Data) [60].

*Toy Monte Carlo is a method based on the random generators using simplified model used to reproduce the more complex physics problem.

When the RAW data are reconstructed by the Tier-0 using the Athena tool, the output is written into the new xAOD format. At this point, one can produce final analysis n-tuples, using both Athena and ROOT, or use derivation framework to produce skimmed/slimmed xAOD. The derivation framework is used to create the intermediate data products from the reconstruction output by removing and adding information while maintaining the structure of EDM used in the original AOD. The final component of the model is the analysis framework, which is used by physicists to read the derived data products, apply various combined performance tools and produce the final analysis n-tuple.

The physics analysis is usually performed on the final n-tuples producing plots and applying various statistical tools to extract physics parameters. The Figure 6.1 visualizes the flow of the data in the ATLAS Run 2 EDM.

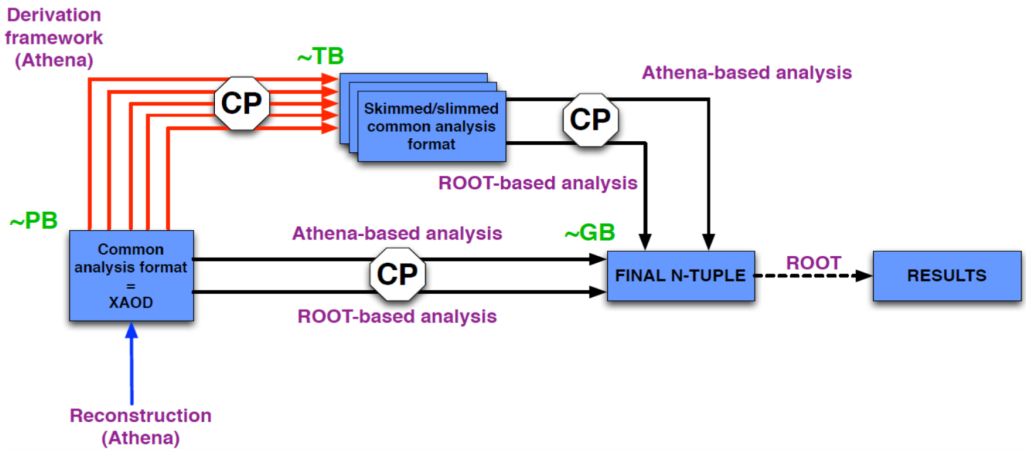

Figure 6.1: The ATLAS Run 2 analysis model consists of a new EDM (xAOD) and a centralized data-reduction framework (Derivation Framework)[60].

The BPhysics working group is extensively using the derivation framework where for each topology, stand-alone derivation is used. Under optimal condition each analysis is using only one derivation. The $B_s^0 \to J/\psi(\mu^+\mu^-)\phi(K^+K^-)$ and $B^\pm \to J/\psi(\mu^+\mu^-)K^\pm$ topologies are covered by the BPHY5 derivation. The main code implemented in the derivation framework is the cascade vertex fit. In the BPHY5 derivation, the vertex fit is looking for the vertex formed by two muons originating from the J/ψ decay and one or two additional kaon tracks.

6.3 Monte Carlo Simulation

Monte Carlo (MC) event generators are used extensively in collider physics. The application of the MC simulations is wide in all the phases of the experiment life-cycle. At the beginning it is used for the investigation of the physics reach of detector concepts and the design of facilities and detectors. The data reconstruction software is developed and optimized on the MC samples and any upgrade or change is validated with respect to the MC simulation. In the physics analysis it is useful tool for the studies of the detector response to the selected signal or background processes. In case of the MC, the whole simulation procedure has to proceed through a series of steps: *Event generation*, *Simulation* and *Digitization*.

6.3.1 Event Generation

The first step of MC simulation is the event generation. There is a variety of general and specialized event generators, but the ATLAS experiment uses two general purpose event generators: Pythia [61] and Herwig. Both, Pythia and Herwig, simulate the initial parton collision described by perturbative QCD. However, for some studies, specialized event generator need to be used. The ATLAS B-Physics analysis in general uses the the specialized tune of the Pythia called PythiaB and in some cases the standard Pythia decay process is replaced by EvtGen.

Pythia8 is one of the most commonly used generators, using the parton shower approach. The parton shower approach is based on the assumption that a $2 \to n$ process, with a complex final state can be achieved by starting from a simple $2 \to 2$ process. This is called parton shower approximation.

In order to generate the final state, Pythia has to perform several steps. First, two particles from the incoming beams are coming upon each other. Normally, each proton is characterized by a set of parton distribution functions, which define the partonic substructure of proton. After that, one shower initiator parton from each beam starts off a sequence of branchings, such as $q \to qg$, which build up an initial-state shower. One incoming parton from each of the two showers enters the hard process. These hard processes described by QCD are calculated using perturbation theory, most commonly in leading order. In the next step, the generation of all subsequent activity on the partonic level follows, involving final-state radiation, multiple parton–parton interactions and the structure of beam remnants. In the final step, hadronisation of this final parton configuration, followed by the decays of unstable particles [61].

PythiaB provides an interface to Pythia and brings additional functionality needed for the BPhysics monte carlo event generation [62]. The first advantage is the speed-up of the BPhysics events simulation. In standard Pythia simulation, the events containing b-quark are generated through one of the following mechanism: flavour creation ($gg \to b\bar{b}, qq \to b\bar{b}$), flavour excitation ($gb \to gb$) and gluon splitting ($g \to b\bar{b}$). However, using standard approach, only 1% of events is expected to contain b and $\bar{b}$-quark. In order to speed up the simulation in PythiaB, the simulation is interrupted after the parton development and the check for the presence of $b\bar{b}$ quarks is performed. Only the events passing the user defined cuts are used for the hadronisation.

PythiaB also provides an option to simulate only wanted decay channels by forcing the b-quark to decay into the channel of interest while the opposite $\bar{b}$-quark can decay by standard rules. It also provide an option to define b-production parameters, such as multiple particle interaction model, structure function, factorization scale or gluon probabilities.

To increase the number of BPhysics events and improve CPU efficiency, the repeated hadronisation tool was implemented in PythiaB. This tool uses generated b-quarks and hadronisation n-times as an independent events. To avoid large amount of duplicite events and ensure optimal performance, the control algorithm checks the cloning factor which is the number of accepted signal events per set of hadronisation loops. The optimal settings give the cloning factor close to unity.

EvtGen simulates the decays of heavy flavour particles, primarily B and D mesons. EvtGen uses spin algebra and complex decay amplitudes to generate each branch of a given full decay tree, taking into account angular and time-dependent correlations which allow for the simulation of CP-violating processes such as $B_s^0 \to J/\psi(\mu^+\mu^-)\phi(K^+K^-)$.

6.3.2 Detector Simulation and Digitization

To obtain full detector simulation of these events, the Geant4 [63] toolkit is used. In general, the Geant4 is a framework for simulation of the passage of particles through material budget, in this case the ATLAS detector. It integrates a complete range of functionality including tracking particles in magnetic field, creation of a geometrical model with a possibly of large number of components of different shapes and materials. It provides a comprehensive set of physics processes to model the behavior of particle physics models and detector hit generation. It is used by a large number of experiments and projects in a variety of application domains, including high energy physics, astrophysics and space science, medical physics and radiation protection.

The ATLAS Geant4 simulation is provided by the Athena service called GeoModel

and contains over the million volumes including the active and inactive material which describe the ATLAS geometry. The Geant4 simulates the passage of the generated particles through each detector element and stores the energies deposited in the sensitive portions of the detector. The interaction in the sensitive media called hits contain the total energy deposition, position and time. These informations are written to a simulation output file, called a hit file.

The hit file is then processed though detector specific digitization software simulating the electronic response to a given signal from active media. The output after digitization process is identical to output produced during recording real data events and thus can be reconstructed with the same algorithms that are used to process the data from the detector.

6.4 The Grid

The ATLAS simulation, reconstruction and analysis tools require extensive computing resources and storage capacities. For this purpose the Worldwide LHC Computing Grid (WLCG) is used. The WLCG, composed of four levels called tiers, is a global collaboration of around 170 computing centres in more than 42 countries, linking up national and international grid infrastructures providing about 900 000 computer cores. The processed data are stored at CERN Advanced Storage system (CASTOR), which relies on a tape-based backend for permanent data archiving, and reached 330 PB of data.

Tier-0 is a data center located at CERN with extended computing center in Budapest, Hungary. It provides the computing and storage resources for the primary events reconstruction of RAW data. After initial processing, data are distributed to a series of Tier-1 centres which are connected directly to Tier-0 by a dedicated fiber optics links.

Tier-1 sites serve as backup for the Tier-0 data storing the proportional share of raw and reconstructed data and provide the computing capacity for the central production tasks such as large scale reprocessing and simulation jobs. Tier-1 provide the sources for the further distribution of data between the sites of the WLGC.

Tier-2 sites are typically hosted at universities and other scientific institutes that can store sufficient data and provide adequate computing power for specific analyses tasks. They are mainly used for the individual physics analysis and proportional share of the production and reconstruction of simulated events.

Tier-3 is last layer of the WLGC, which serves as individual local computing resource and can consist of local clusters in a university department or even an individual PCs.

The computing resources are organised in 13 clouds, where each cloud contain single Tier-1 center. To each cloud is assigned a number of Tier-2 centers in proximate geographical area. This arrangement seves for managing purposes, since the grid nodes are located around the world.

6.5 The Trigger and Data Acquisition

The trigger system is designed to reduce the event rate from the design bunch-crossing rate of 40 MHz to an average recording rate of ~ 1 kHz. The trigger system evaluates collected events according to certain predefined physics signatures and defines which collision events should be saved to disk for further analysis. At the conditions which prevail at the LHC, the trigger system has to be sophisticated enough to select only the events which are physically interesting, such as events with high p_{T}, objects with high missing E_{T} or events with certain particles in the final state.

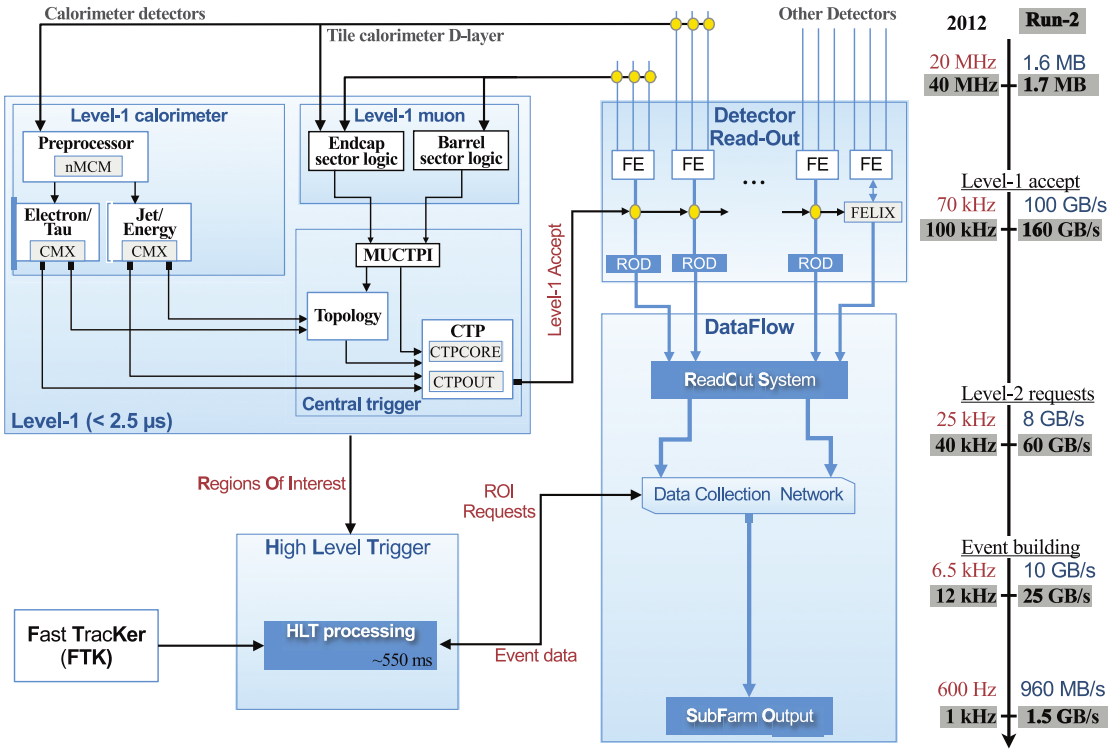

Figure 6.2: Schematic overview of the Run 2 configuration of the Trigger and DAQ system [64].

The ATLAS detector was using a three-level trigger system in Run 1; however, for Run 2 a different trigger scheme was devised. The new trigger system consists of a hardware Level-1 (L1) and a software-based HLT. This new trigger system is faster than the previous

one and saves computing resources. The Figure 6.2 shows the data flow in ATLAS trigger and acquisition system.

Level-1 Trigger

The L1 trigger is hardware based trigger using fast custom-made electronics and runs with a fixed latency of 2.5 µs. The L1 uses information from the fast detectors such as RPCs or TGCs for muon system and LAr ECAL and TileCal for calorimeteric cluster information. The L1 trigger operates with rough detector position (ϕ, θ) information in a so-called regions of interest (RoIs)[†] and decides if the event will be investigated by the higher trigger level. There is no tracking information extracted from the ID, because the readout system is not fast enough to acquire required information.

The L1 trigger decision is formed by the Central Trigger Processor (CTP). L1 reduces the event rate from the LHC interaction rate of 40 MHz to 100 kHz. In Run 2, new L1Topo trigger was commissioned, which performs selections based on geometric or kinematic association between trigger objects received from L1Calo or L1Muon.

HLT Trigger

Events accepted by L1 are processed by the HLT. HLT is based on algorithms implemented in data acquisition software which must further reduce the number of events recorded to disk to an average rate of about 1 kHz within a few seconds. The HLT employs offline-like reconstruction algorithms using data with full granularity within the RoI provided by the L1 and combines information from all detectors, including ID. The HLT is using dedicated computers farm with $\approx$ 40000 processor cores. The events fulfilling the HLT decision are written into different data streams according to the trigger menu settings.

6.5.1 Trigger Menu

The ATLAS detector employs many different types of triggers. Each trigger is developed for a specific purpose. The list of trigger algorithms used for data-taking is called trigger menu. The triggers in the trigger menu can be divided into following categories: primary triggers (also called physics triggers), supporting triggers used for efficiency and performance measurements or monitoring, alternative triggers, backup triggers and calibration triggers. The output from the trigger algorithms is organized into streams. Physics analysis streams require full detector information, while monitoring and calibration streams focus on a specific data subset or detector region.

[†]RoIs are detector areas, where the L1 trigger sees the interesting detector signature and tags them for further processing.

On top of the trigger menu, prescale factors for L1 items and HLT triggers can be applied. Prescale factors are used to reduce the amount of events accepted by a certain L1 item or HLT chain. For a prescale factor of N, only one event out of N events which pass the trigger requirement is accepted. The trigger rates in 2018 for Physics streams is shown in the Figure 6.3.

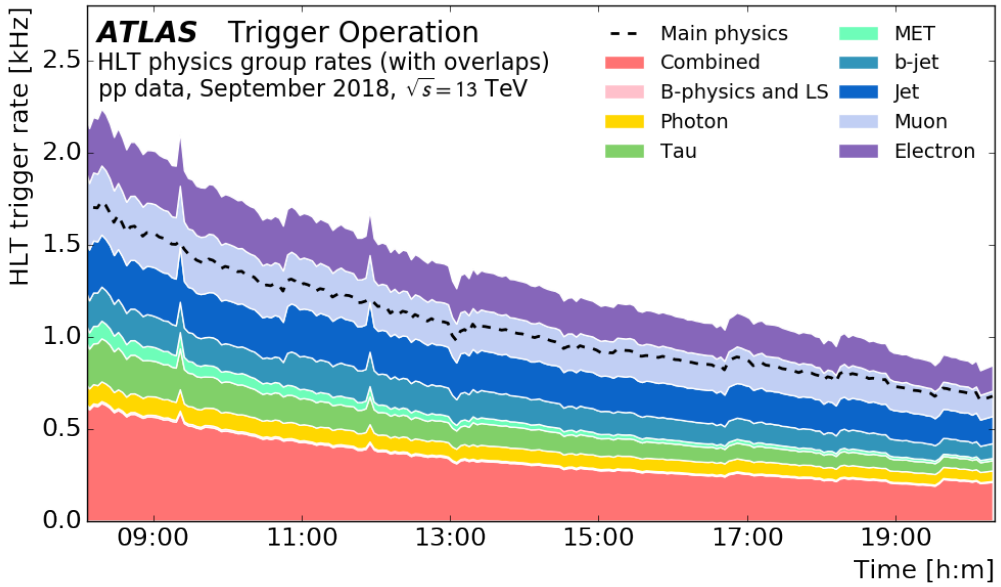

Figure 6.3: Physics trigger group rates at the High Level Trigger as a function of the time in a fill taken in September 2018 with a peak luminosity of $\mathcal{L} = 2.0 \times 10^{34}\,\mathrm{cm}^{-2}\,\mathrm{s}^{-1}$ and an average pile up of $\langle\mu\rangle = 56$ [65].

6.5.2 B-Physics Trigger

Trigger selection of events for physics studies of B-meson decays (B-Physics triggers) is mostly based on identification of B-hadrons through their decay chains with a muon pair in the final state. The di-muon triggers require two muons at L1 with p_{T} larger than 4 GeV, 6 GeV or 11 GeV and pseudorapidity $|\eta| < 2.5$.

The primary L1 items in Run 2 became the topological triggers based on two muon tracks with p_{T} larger than 6 GeV and with additional kinematic selection. The topological cut of $0.2 < \Delta R < 1.5$ between the two L1 MU6 muons reduces the 2MU6 rate about a factor of three and keep efficiency above 85%.

Additional primary and supporting triggers are also implemented. Triggers are based on the single L1 muon RoIs with an additional track found at the HLT. These triggers do not suffer with similar opening angle issues, but due to high rate they need to be highly prescaled.

If the event passes the L1 trigger, the muons are reconstructed using identical HLT algorithms as in the muon-trigger items, with the additional requirements that the two muons should form a good vertex within a certain invariant mass window [66]. The Figure 6.4 shows the invariant mass distribution of di-muon tracks collected by the B-Physics triggers in 2018.

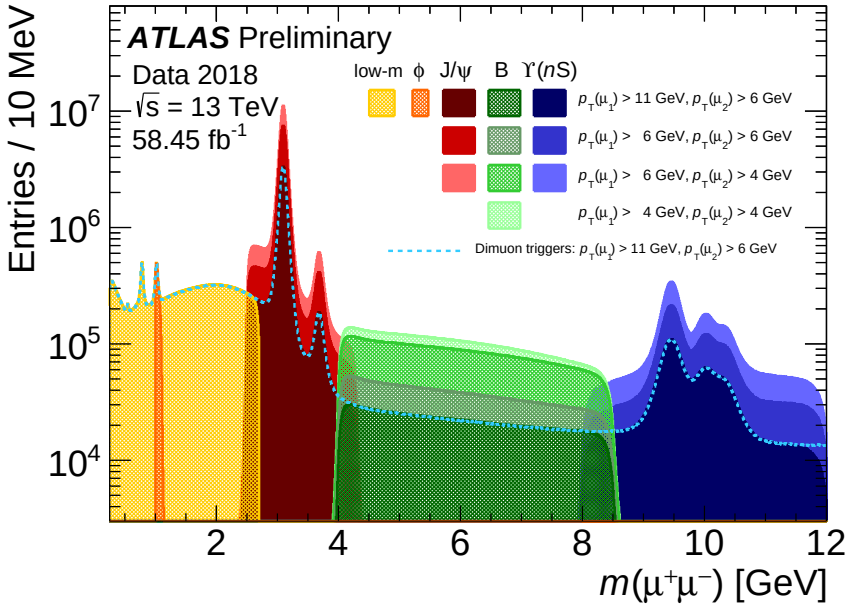

Figure 6.4: Invariant mass distributions for oppositely charged muon candidate pairs that pass various triggers [67].

CHAPTER 7

Beauty Physics at ATLAS

The Beauty Physics (also called B-Physics) is the part of particle physics which is dealing with interactions containing at least one b-quark. Because the b-quark is the third heaviest particle in the Standard Model, its coupling can be large to the possible new particles predicted by the Beyond Standard Model. Due to large b-quark production cross-section at the LHC, relatively long lifetimes and large masses of B-hadrons, this channel will allow sensitive tests of possible new physics contributions. The ATLAS B-Physics program includes SM measurements and new physics searches, such as measurement of the CP-violating phase ϕ_s of the B_s^0 system, searching for anomalous rates of the rare B-decay channel: $B_s^0 \rightarrow \mu^+\mu^-$, as well as precise tests of QCD by studying the production mechanisms of $b\bar{b}$ pairs, beauty baryon polarization, and lifetime measurement.

The ATLAS B-Physics and Light States Working group is organized into three sub-groups: Rare decays, Onia production and $b\bar{b}$ cross-section, and Physics with $B \rightarrow J/\psi X$. Following section presents an overview of the selected analyses.

7.1 Search for $\tau \rightarrow 3\mu$

The observation of neutrino oscillations was the first evidence of lepton flavour violation (LFV). As a consequence, the introduction of mass terms for neutrinos in the SM implies that LFV exists also in the charged sector (cLFV). Many BSM theories predict enhanced LFV in τ^- decays with respect to μ^- decays, with branching fractions within experimental reach. From SM prediction, these branching fractions are negligible, but in the BSM physics these branching fractions could be significantly enhanced. The one of the most promising channel is $\tau \rightarrow 3\mu$ with SM branching fraction of $\mathrm{Br}(\tau \rightarrow 3\mu) < 10^{-14}$, while a number of models beyond the SM predict it to be of the order of 10^{-8}–10^{-10}.

The ATLAS performed a measurement of $\tau \to 3\mu$ on the Run 1 data sample of 20.3 fb^{-1} of pp collision data at a centre-of-mass energy of 8 TeV [68]. The expected number of background events in performed analysis was $0.193 \pm 0.131(\text{syst.}) \pm 0.037(\text{stat.})$. Since no significant enhancement was observed in the signal region for the final selection, as can be seen in Figure 7.1, the upper limit of $3.76 \times 10^{-7}(3.94 \times 10^{-7})$ on $\text{Br}(\tau \to 3\mu)$ at 90% CL was established.

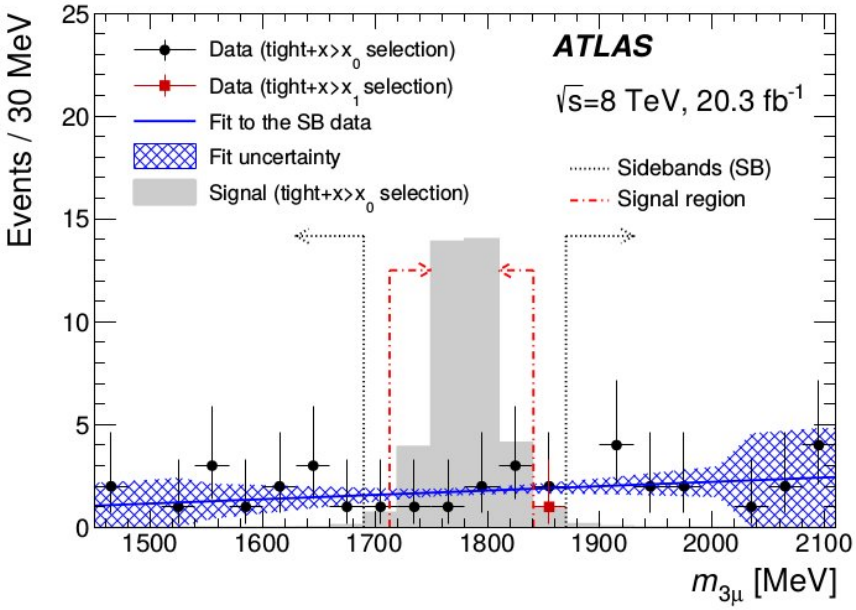

Figure 7.1: The three-muon mass distribution in the range [1450,2110] MeV shown for the $tight + x > x_0$ selection by solid black circles and for the $tight + x > x_1$ selection by the solid red square. The sideband and signal regions are indicated by the arrows. The $tight + x > x_0$ data are fit in the two sidebands simultaneously, excluding the events in the blinded region. The hatched area shows the uncertainty in the fit due to the SB range definition, the x_0 cut location and the fit function choice. The solid gray area shows the signal shape (obtained from MC simulation), normalized to the area of the data for the $tight + x > x_0$ selection [68].

7.2 Study of the Rare Decay $B_s^0 \to \mu^+\mu^-$

Flavour changing neutral current processes are highly suppressed in the SM and, therefore, their study is of particular interest in the search for new physics. The SM predicts the branching fraction for the decay $B_s^0 \to \mu^+\mu^-$ to be extremely small: $(3.23 \pm 0.27) \times 10^{-9}$. The previous theoretical prediction for the cross-section should be increased by 9% to take into account the time evolution of the initial state, but the theories beyond the SM (re-

ferred to as new physics, or NP), especially those with an extended Higgs sector, can significantly enhance these branching fractions by non-SM heavy particles in the loop diagrams contributing to the amplitude. Figure 7.2 shows one of the possible Feynman diagram for the $B_s^0 \to \mu^+\mu^-$ decay.

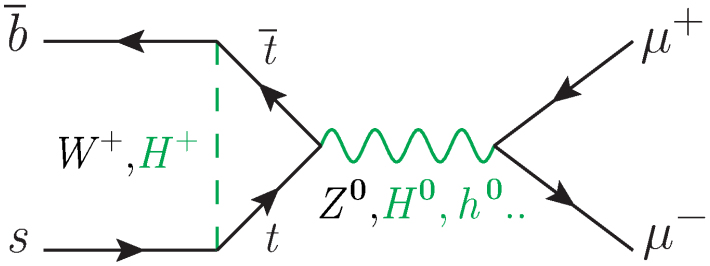

Figure 7.2: One possible Feynman diagram of the decay $B_s^0 \to \mu^+\mu^-$. In addition to the diagram with Standard Model particles (in black), possible diagrams with particles from models beyond the Standard Model (in green) are displayed.

The latest ATLAS measurement was performed on the 26.3 fb^{-1} of 13 TeV LHC pp collisions data, measuring the branching fraction $\mathrm{Br}(B_s^0 \to \mu^+\mu^-) = (3.2^{+1.1}_{-1.0}) \times 10^{-9}$ and an upper limit $\mathrm{Br}(B^0 \to \mu^+\mu^-) < 4.3 \times 10^{-10}$ at 95% confidence level [69]. The likelihood contours of the fitted result compared with SM prediction is depicted in the Figure 7.3.

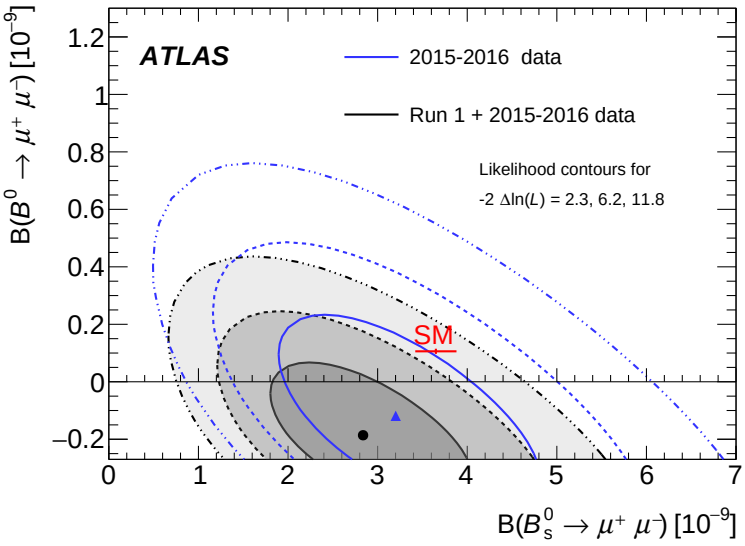

Figure 7.3: Likelihood contours for the combination of the Run 1 and 2015-2016 Run 2 results (shaded areas). The contours are obtained from the combined likelihoods of the two analyses, for values of $-2\Delta \ln(L)$ equal to 2.3, 6.2 and 11.8. The empty contours represent the results from 2015-2016 Run 2 data alone. The SM prediction with uncertainties is indicated [69].

7.3 Observation of an Excited $B_c^{\pm}$ Meson State

The $B_c^{\pm}$ meson was first observed by the CDF experiment in the semileptonic decay mode [70] and since then several searches for its excited state were performed. Since the spectrum and properties of the $B_c^{\pm}$ family are predicted by nonrelativistic potential models, perturbative QCD and lattice calculations, any measurement of its excited state would provide tests of the predictions of these models and give useful information on the strong interaction potential.

The search for excited states of the $B_c^{\pm}$ with the ATLAS detector was performed through its hadronic transition to the ground state, with the latter detected in the decay $B_c^{\pm} \to J/\psi\pi^{\pm}$ [71]. The second S-wave state, $B_c^{\pm}(2S)$, was predicted to have a mass in the range of 6835–6917 MeV and to have pseudoscalar (0^-) and vector (1^-) spin states that differ in mass by about 20–50 MeV.

The ATLAS measurement uses pp collision data with $\sqrt{s} = 7$ TeV collected in 2011 and $\sqrt{s} = 8$ TeV collected in 2012 with integral luminosity of $4.9\,\text{fb}^{-1}$ and $19.2\,\text{fb}^{-1}$, respectively. After the reconstruction and proper candidate selection optimized separately for 7 and 8 TeV data using the corresponding MC samples, the maximum likelihood fit was performed using variable $Q = m(B_c^{\pm}\pi\pi) - m(B_c^{\pm}) - 2m(\pi^{\pm})$, where $m(B_c^{\pm})$ and $m(B_c^{\pm}\pi\pi)$ are the offline reconstructed invariant masses of selected candidates and the $m(\pi^{\pm})$ is the mass of a charged pion. The resulting mass difference distribution is shown in Figure 7.4.

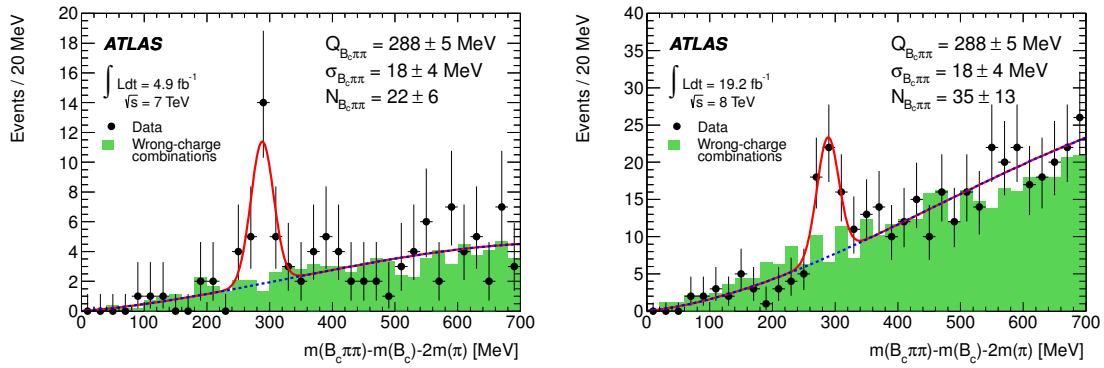

Figure 7.4: The distribution for the right-charge combinations (points with error bars) and for the same (wrong) pion charge combinations (shaded histogram) in 7 TeV data (left) and in 8 TeV data (right). The wrong-charge combinations are normalized to the same yield as the right-charge background. The solid line is the projection of the results of the unbinned maximum likelihood fit to all candidates in the range 0–700 MeV. The dashed line is the projection of the background component of the same fit [71].

The significance of the observation is $5.2\,\sigma$ with the look elsewhere effect taken into account, and the local significance is $5.4\,\sigma$. The mass of observed structure is consistent

with the predicted mass of the $B_c^{\pm}(2S)$ with no $B_c^*(2S)$ hypothesis. The observation of an excited $B_c^{\pm}$ meson state was confirmed by the CMS [72] experiment; however, the LHCb [73] reported no significant signal in the region of interest.

7.4 B^+ Cross-section and Lifetime

Measurements of the B-hadron production cross-section in pp collisions at the LHC provide sensitive tests of calculations based on QCD. Thanks to the extended coverage and excellent performance of the LHC detectors, heavy-quark production at higher centre-of-mass energies and in wider transverse momentum (p_{T}) and rapidity (y) ranges can be measured. In the NLO and FONLL perturbative calculations, the theoretical predictions have large uncertainties arising from the choice of the renormalization and factorization scales and the b-quark mass. Accurate measurements provide tests of the validity of the different production models.

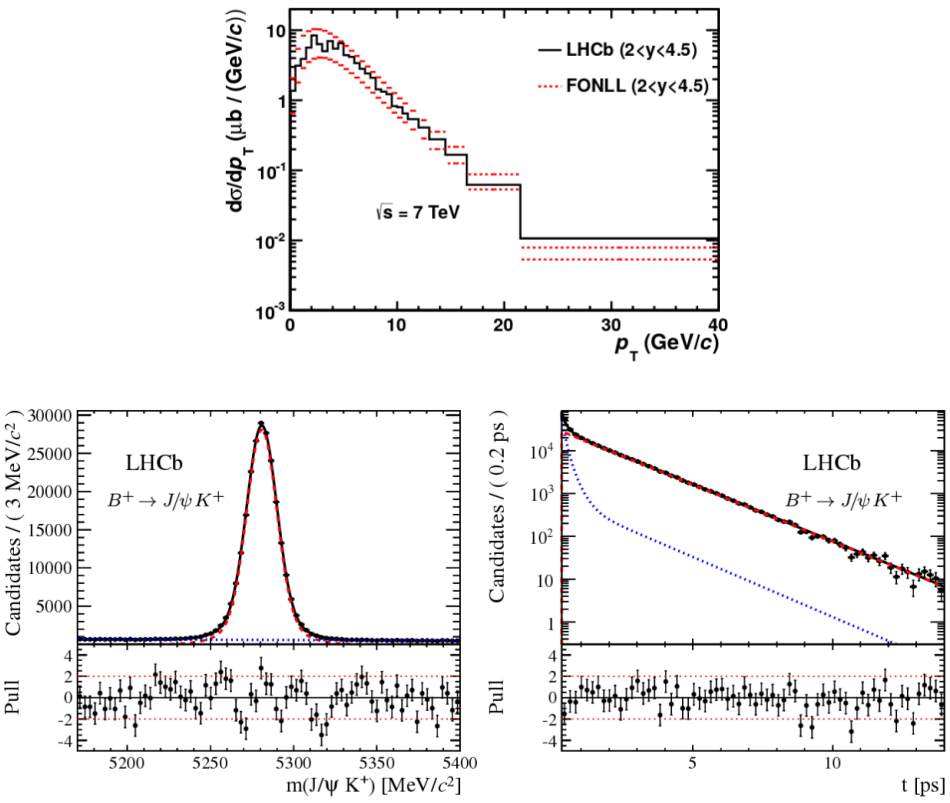

Figure 7.5: Differential production cross-section as a function of the B^+ transverse momentum measured by LHCb experiment at $\sqrt{s} = 7\,\mathrm{TeV}$ compared with FNLLO calculation (Top). Distributions of the mass (bottom-left) and decay time (bottom-right) of $B^+ \to J/\psi K^+$ candidates and their associated residual uncertainties [74, 75].

In addition, many searches for BSM physics often rely on the ability to accurately predict the production rates of b-quarks that can form backgrounds in combination with other high energy processes. In addition, knowledge of the b-quark yield is essential for calculating the sensitivity of experiments testing the SM by measuring CP-violating and rare decay processes.

CHAPTER 8

CP-Violation in $B_s^0 \to J/\psi\phi$ Decay

The main objective of this thesis is the measurement of CP-violating parameters in $B_s^0 \to J/\psi\phi$ decay based on the data collected between years 2015 and 2017 with $80.5\,\text{fb}^{-1}$ of pp collisions at a centre-of-mass energy of 13 TeV by the ATLAS experiment. The measured parameters include the CP-violating phase Φ_s, the width difference $\Delta\Gamma_s$ between the B_s^0 meson mass eigenstates and the average decay width Γ_s. The values measured for the physical parameters are combined with those from $19.2\,\text{fb}^{-1}$ of 7 TeV and 8 TeV data.

The analysis was submitted to the EPJC journal as [35]. At the end of this chapter, the outlook of improvements planned for the full Run 2 measurement, including the 2018 dataset, is presented.

8.1 Data and MC Samples

As mentioned above, this analysis uses data from several periods of pp collision at 13 TeV namely: $3.2\,\text{fb}^{-1}$ collected in year 2015, $33.0\,\text{fb}^{-1}$ collected in year 2016 and $44.3\,\text{fb}^{-1}$ collected in year 2017. The combined luminosity is therefore $80.5\,\text{fb}^{-1}$ with an uncertainty of 2.0% estimated based on LUCID-2 detector.

In addition to the real data, this analysis uses MC samples of $B_s^0 \to J/\psi\phi$, $B^\pm \to J/\psi K^\pm$, $B_d^0 \to J/\psi K^{*0}$ and $\Lambda_b \to J/\psi p K^-$. These MC samples are used for background modeling, detector response studies, acceptances and systematic uncertainty evaluation.

8.2 Reconstruction and Candidate Selection

The data were collected during a period of increasing instantaneous luminosity, and the trigger conditions varied over this time period. The triggers used to select events

for this analysis are based on the identification of a $J/\psi \to \mu^+\mu^-$ decay, with transverse momentum (p_{T}) thresholds of either 4 GeV or 6 GeV for the candidate muons. The careful trigger selection was performed to avoid any lifetime bias, since this measurement is extremely sensitive to the lifetime estimation.

Only the data passing the Good Run List (GRL) selection are used in the analysis. The GRL selects only the events where the LHC beam was operating under stable conditions and the ID and the MS both operating correctly. In addition, each event must contain at least one reconstructed primary vertex, formed from at least four ID tracks and at least one pair of oppositely charged muon candidates that are reconstructed using information from the MS and the ID.

$J/\psi \to \mu^+\mu^-$ Reconstruction

The muon tracks used in the analysis are required to meet the *Tight* or *Low-*p_{T} working point identification criteria defined by the ATLAS Muon Combined Performance Working Group [76] and must pass through the following selection cuts:

- The reconstructed tracks are required to have at least one hit in the Pixel detector and at least five hits in the SCT.
- The reconstructed tracks are required to have fewer than three Pixel or SCT holes, where hole is defined as an active sensor traversed by the track but containing no hits.
- In the region of full TRT acceptance, $0.1 < |\eta(\mu)| < 1.9$, it requires that at least 10% of the TRT hits originally assigned to the track are included in the final track fit.

The muon track parameters are determined from the ID measurement alone, since the precision of the measured track parameters is dominated by the ID track reconstruction in the p_{T} range of interest for this analysis. Pairs of oppositely charged muon tracks are refitted to a common vertex and the pair is accepted for further consideration if the quality of the vertex fit meets the requirement $\chi^2/\mathrm{d.o.f.} < 10$. The invariant mass of the muon pair is calculated from the refitted track parameters. In order to account for varying mass resolution in different parts of the detector, the J/ψ candidates are divided into three subsets according to the pseudorapidity η of the muons. A maximum-likelihood fit is used to extract the J/ψ mass and the corresponding mass resolution for these three subsets, and define J/ψ invariant mass signal region to retain 99.8% of the J/ψ candidates. The three subsets of J/ψ candidates are defined as follows:

- If both muons have $|\eta| < 1.05$, the di-muon invariant mass must fall in the range 2.959–3.229 GeV to be accepted as a J/ψ candidate.

- If one muon has $1.05 < |\eta| < 2.5$ and the other muon $|\eta| < 1.05$, the corresponding signal region is 2.913–3.273 GeV.

- If both muons have $1.05 < |\eta| < 2.5$, the signal region is 2.852–3.332 GeV.

The reconstructed J/ψ invariant mass distribution after candidate selection cuts from all three subsets together is shown in the Figure 8.1.

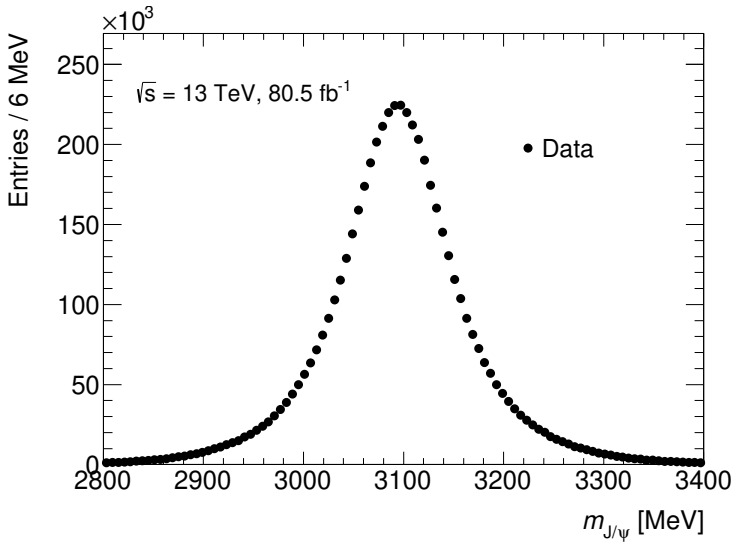

Figure 8.1: The reconstructed J/ψ invariant mass distribution after candidate selection cuts.

$\phi \to K^+K^-$ Reconstruction

The candidates for the $\phi \to K^+K^-$ decay are reconstructed from all pairs of oppositely charged ID tracks that are not identified as muons. Each track must pass following selection criteria:

- $p_{\mathrm{T}} > 1\,\mathrm{GeV}$,

- $|\eta| < 2.5$,

- at least one pixel hit,

- at least five SCT hits.

The invariant mass of the reconstructed candidates from two hadronic tracks is calculated using PDG mass hypothesis of $\phi \to K^+K^-$, $K^{0*} \to K^-\pi^+$ and $\overline{K^{0*}} \to K^+\pi^-$. The reconstructed Φ invariant mass distribution after candidate selection cuts is shown in the Figure 8.2.

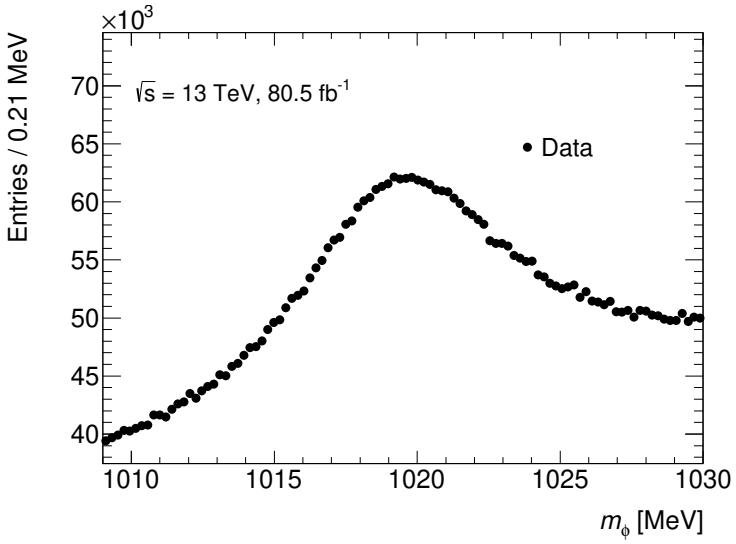

Figure 8.2: The reconstructed Φ invariant mass distribution after candidate selection cuts.

$B_s^0 \to J/\psi(\mu^+\mu^-)\phi(K^+K^-)$ Reconstruction

Candidate events for $B_s^0 \to J/\psi(\mu^+\mu^-)\phi(K^+K^-)$ decays are selected by fitting the tracks for each combination of $J/\psi \to \mu^+\mu^-$ and $\phi \to K^+K^-$ to a common vertex. The fit is constrained by fixing the invariant mass calculated from the two muon tracks to the J/ψ mass [4]. A quadruplet of tracks is accepted for further analysis if the vertex fit passes the following criteria:

- invariant mass of the hadron track pairs (assuming that they are kaons) falls within the interval 1.0085 GeV $< m(K^+K^-) <$ 1.0305 GeV,
- χ^2/d.o.f. < 3,
- $p_{\mathrm{T}} > 10\,\mathrm{GeV}$,
- If there is more than one accepted candidate in the event, the candidate with the lowest χ^2/d.o.f. is selected.

In total, 2,977,526 B_s^0 candidates are collected within a mass range of 5.150–5.650 GeV.

8.2.1 Proper Decay Time Calculation

For each B_s^0 meson candidate, the proper decay time t is estimated using the expression:

$$t = \frac{L_{xy}\ m_{_B}}{p_{\mathrm{T}_B}},$$

where p_{T_B} is the reconstructed transverse momentum of the B_s^0 meson candidate and $m_{_B}$ denotes the mass of the B_s^0 meson, taken from [4]. The transverse decay length, L_{xy}, is the displacement in the transverse plane of the B_s^0 meson decay vertex with respect to the primary vertex, projected onto the direction of the B_s^0 transverse momentum. The position of the primary vertex used to calculate this quantity is determined from a refit following the removal of the tracks used to reconstruct the B_s^0 meson candidate.

For the selected events, the average number of pile-up proton–proton interactions is 21, necessitating a choice of the best candidate for the primary vertex at which the B_s^0 meson is produced. The variable used is the three-dimensional impact parameter a_0, which is calculated as the distance between the line extrapolated from the reconstructed B_s^0 meson vertex in the direction of the B_s^0 momentum, and each primary vertex candidate. The chosen primary vertex is the one with the smallest d_0.

A study made using a MC simulated dataset has shown that the precision of the reconstructed B_s^0 proper decay time remains stable over the range of pile-up encountered during Run 2 data-taking. No B_s^0 meson decay-time cut is applied in this analysis.

8.3 Maximum Likelihood Fit

In order to extract physical parameters, the unbinned maximum likelihood fit to the selected B_s^0 candidates is performed. Due to the complex nature of the model simultaneously describing mass-lifetime and angles, this analysis uses a custom designed likelihood function, which is minimized using the minuit package [77]. The principles and properties of the Maximum Likelihood method are reviewed in subsection 8.3.1, while the overall model used to fit to data is described in subsection 8.3.2.

8.3.1 Maximum Likelihood Method

The Maximum Likelihood (ML) method is a technique used to estimate the values of the parameters given a finite sample of data. The important part of the likelihood method is to define the Probability Density Function (PDF) used to describe the shape of the continuous random variable x. The general form of the PDF is given as

$$P(x;\vec{\theta}), \tag{8.1}$$

where the $\vec{\theta} = (\theta_1, \ldots, \theta_N)$ are parameters which are to be estimated. The important PDF property is that it is normalized to unity over the range of the parameter x for any value of $\vec{\theta}$.

The likelihood function is the probability density of the data, viewed as a function of the parameters $\vec{\theta}$ defined by $\mathcal{L}(\vec{\theta}) = P(x;\vec{\theta})$. The likelihood function assesses the chance of observing a particular sample x when the parameters are equal to $\vec{\theta}$. The likelihood of the independent and identically distributed random variables x_i is given by following equation:

$$\mathcal{L}(\vec{\theta}) = \prod_{i=0}^{N} P(x_i;\vec{\theta}). \tag{8.2}$$

The maximum likelihood estimate (MLE) of the parameters $\vec{\theta}$ are the values of $\vec{\theta'}$ that maximize the likelihood function given by 8.2. It is often more convenient to use the negative log-likelihood function and maximize the sum of each component rather than maximizing the product as given in function 8.2.

To evaluate the statistical uncertainty of the estimate, the variance of the MLE must be calculated. Since the analytical solution might not exist, the estimation based on Rao-Cramer-Frechet (RCF) bound is commonly used [78]. The formula for the inverse of the covariance matrix $V_{ij} = cov[\theta_i, \theta_j]$ is given as:

$$(\widehat{V_{ij}})^{-1} = -\frac{\partial^2 \log \mathcal{L}}{\partial\theta_i \partial\theta_j}. \tag{8.3}$$

Maximum likelihood estimators are important because they are asymptotically unbiased, efficient and have Gaussian errors.

8.3.2 Likelihood Fit of $B_s^0 \to J/\psi\phi$ Analysis

The maximum likelihood function of the $B_s^0 \to J/\psi\phi$ analysis is defined as a combination of the signal and background probability density functions in following observables: invariant mass m_i, proper decay time t_i, three transversity angles $\Omega_i = (\theta_i, \psi_i, \phi_i)$, mass error uncertainty σ_{m_i}, proper decay time uncertainty σ_{t_i}, transverse momentum p_{T_i} of B_s^0 candidate and tagging probability $P(B|Q_x)$ described in section 8.4. The signal contribution is contaminated not only by the combinatorial background, but also due to the wrong mass assignment to the tracks, $B_d \to J/\psi K^{0*}$ and $\Lambda_b \to J/\psi p K^-$ contribute to the signal region. Each of these components need to be accommodated in the likelihood function by its own probability density function, $\mathcal{F}_x$, to extract physics parameters correctly. The overall

likelihood function used in this analysis takes the following form

$$\begin{aligned}\ln\ \mathcal{L} = \sum_{i=1}^{N} w_i \cdot \ln[& f_{\rm s} \cdot \mathcal{F}_{\rm s}(m_i, t_i, \sigma_{m_i}, \sigma_{t_i}, \Omega_i, P_i(B|Q_x), p_{{\rm T}_i}) \\ & + f_{\rm s} \cdot f_{B_s^0} \cdot \mathcal{F}_{B_s^0}(m_i, t_i, \sigma_{m_i}, \sigma_{t_i}, \Omega_i, P_i(B|Q_x), p_{{\rm T}_i}) \\ & + f_{\rm s} \cdot f_{\Lambda_b} \cdot \mathcal{F}_{\Lambda_b}(m_i, t_i, \sigma_{m_i}, \sigma_{t_i}, \Omega_i, P_i(B|Q_x), p_{{\rm T}_i}) \\ & + (1 - f_{\rm s} \cdot (1 + f_{B_s^0} + f_{\Lambda_b}))\mathcal{F}_{\rm bkg}(m_i, t_i, \sigma_{m_i}, \sigma_{t_i}, \Omega_i, P_i(B|Q_x), p_{{\rm T}_i})],\end{aligned} \tag{8.4}$$

where N is the number of B_s^0 candidates, w_i is a weighting factor to account for the trigger efficiency and lifetime corrections (section 8.3.6), f_s is the fraction of signal component $\mathcal{F}_{\rm s}$ (section 8.3.3), $f_{B_d^0}$ and f_{Λ_b} are the relative fractions of dedicated B_d^0 and Λ_b backgrounds (section 8.3.5), $\mathcal{F}_{\rm bkg}$ accounts for the combinatorial background (section 8.3.4).

8.3.3 Signal PDF

The PDF used to describe the signal events, $\mathcal{F}_{\rm s}$, has the following composition:

$$\begin{aligned}\mathcal{F}_{\rm s}(m_i, t_i, \sigma_{m_i}, \sigma_{t_i}, \Omega_i, P_i(B|Q_x), p_{{\rm T}_i}) = & P_{\rm s}(m_i|\sigma_{m_i}) \cdot P_{\rm s}(t_i, \Omega_i|\sigma_{t_i}, P_i(B|Q_x)) \\ & \cdot P_{\rm s}(\sigma_{m_i}|p_{{\rm T}_i}) \cdot P_{\rm s}(\sigma_{t_i}|p_{{\rm T}_i}) \cdot P_{\rm s}(P_i(B|Q_x)) \\ & \cdot A(\Omega_i, p_{{\rm T}_i}) \cdot P_{\rm s}(p_{{\rm T}_i}).\end{aligned} \tag{8.5}$$

The signal PDF accounts for the mass, time-angular density functions as well as the detector acceptance and conditional probability density functions for the mass error, time error, transverse momentum and tagging probability.

The probability terms $P_{\rm s}(\sigma_{m_i}|p_{{\rm T}_i})$, $P_{\rm s}(\sigma_{t_i}|p_{{\rm T}_i})$ and $P_{\rm s}(p_{{\rm T}i})$ appear in the Likelihood function to account for the effect when the signal and background distributions are different and it is not possible to factorize them out from the PDFs. These conditional probabilities are also called Punzi terms and are described in the standalone section 8.3.7 together with background component. The tagging probability term for signal $P_{\rm s}(P(B|Q_x))$ is described in section 8.4.4.

Signal Time-Angular PDF

The term $P_{\rm s}(t_i, \Omega_i|\sigma_{t_i}, P_i(B|Q_x))$ is a joint PDF for the decay time t and the transversity angles Ω for the $B_s^0 \to J/\psi(\mu^+\mu^-)\phi(K^+K^-)$ decay. It is formed from the differential decay rate given in section 3.3. The joint PDF of proper decay time and decay angles includes the main physics parameters of interest:

- the CP-violating phase ϕ_s,
- the average decay width Γ_s and the decay width difference $\Delta\Gamma_s$,
- the size of the CP-state amplitudes at $t = 0$: $|A_\parallel(0)|^2$, $|A_0(0)|^2$ and their corresponding strong phases $\delta_\perp$ and $\delta_\parallel$,
- the size of the S-wave amplitude at $t = 0$: $|A_S(0)|^2$ and corresponding strong phase δ_S.

The size of the remaining amplitude $|A_\perp(0)|^2$ is constrained by the normalisation condition, phase δ_0 is set to zero and Δm_s is fixed to the world average value $\Delta m_s = (17.757 \pm 0.021)\,\mathrm{ps}^{-1}$ [4].

To take into account the limited lifetime resolution of the detector, each time element is smeared with a Gaussian resolution function

$$R_\mathrm{s}(t_i|\sigma_{t_i}) \equiv \frac{1}{\sqrt{2\pi}S_t\sigma_{t_i}} \cdot \exp^{-\left(\frac{t_i}{\sqrt{2}S_t\sigma_{t_i}}\right)^2}. \tag{8.6}$$

This smearing is performed numerically on an event-by-event basis where the width of the Gaussian function is the proper decay time uncertainty σ_{t_i} multiplied by a scale factor, S_t, to account for any mis-measurements. The mean of the Gaussian function is set to zero.

The proper decay time uncertainty distribution for the data, including the fits to the background and the signal contributions is shown in Figure 8.3. The average value of this uncertainty for signal events is 69 fs.

Signal Mass PDF

The first term $P_\mathrm{s}(m_i)$ in maximum likelihood function corresponds to the mass PDF which is modeled by a single Gaussian function smeared with per candidate mass error resolution σ_{m_i} and a single correction factor S_m, also called scale factor. The scale factor accounts for general misidentification of the measured mass error. The function takes the following form

$$P_\mathrm{s}(m_i|\sigma_{m_i}) \equiv \frac{1}{\sqrt{2\pi}S_m\sigma_{m_i}} \cdot \exp^{-\left(\frac{m_i - m_{B_s}}{\sqrt{2}S_m\sigma_{m_i}}\right)^2}, \tag{8.7}$$

where the mean value m_{B_s} is the B_s^0 meson mass, which is a fit parameter and the width of the Gaussian function is the product of $S_m \cdot \sigma_{m_i}$, were the mass error σ_{m_i} is calculated for each $J/\psi\phi$ candidate from the covariance matrix associated with the 4-track vertex

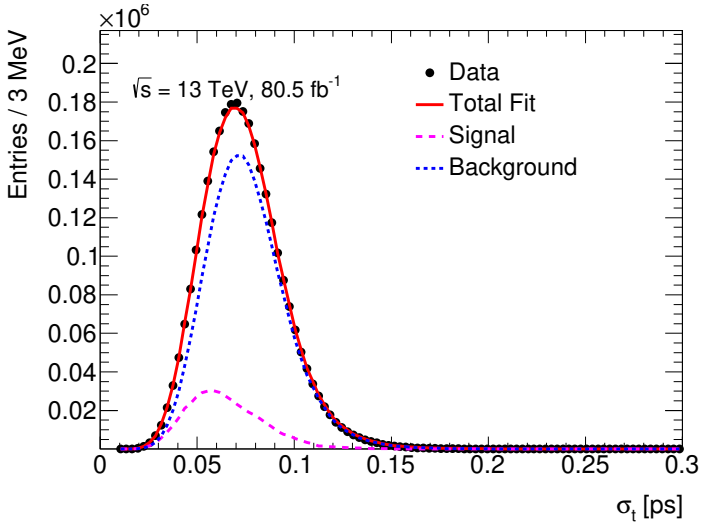

Figure 8.3: The proper decay time uncertainty distribution for the data (black), and the fits to the background (blue) and the signal (purple) contributions. The total fit is shown as a red curve.

fit. The overall mass error distribution for signal and background component is depicted in Figure 8.4.

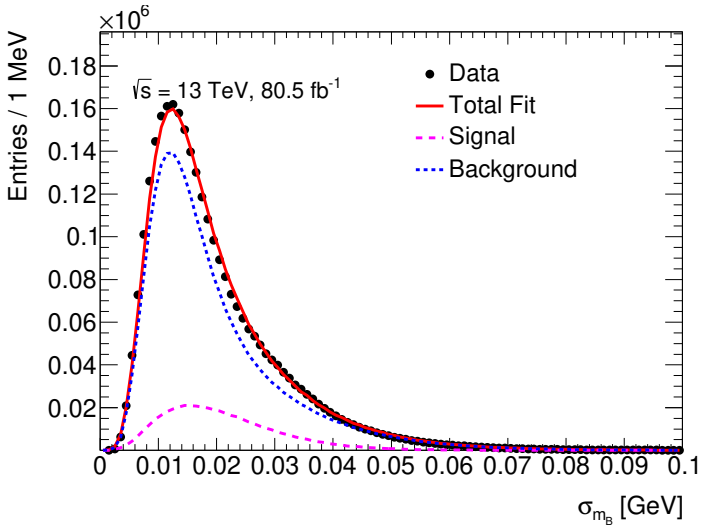

Figure 8.4: The invariant mass uncertainty distribution for the data (black), and the fits to the background (blue) and the signal (purple) contributions. The total fit is shown as a red curve.

Detector Acceptance

The angular acceptance of the detector and kinematic cuts on the angular distributions are included in the likelihood function through $A(\Omega_i, p_{Ti})$. This is calculated using a 4D binned acceptance method, applying an event-by-event efficiency according to the transversity angles $(\theta_T, \psi_T, \phi_T)$ and the p_{T} of the candidate. The p_{T} binning is necessary, because the angular acceptance is influenced by the p_{T} of the B_s^0 candidate. The default p_{T} binning was chosen as follows: 10–15 GeV, 15–18 GeV, 18–22 GeV, 22–26 GeV, 26–30 GeV, 30–35 GeV, 35–45 GeV and > 45 GeV. The acceptance is calculated from the $B_s^0 \to J/\psi\phi$ MC events which take into account triggers and their prescales, reconstruction and selection cuts. To account for the differing trigger menus and pre-scales during the data taking, the total luminosity is calculated for each unique trigger menu relevant to our analysis and the generated MC sample is then split in proportion to the size of each unique trigger menu collected. Applying this re-weighting technique, the MC sample gives a description in a very good agreement with collected data and the small differences in the modeling have negligible effect on the fit results.

In the likelihood function, the acceptance is treated as an angular acceptance PDF, which is multiplied with the time- and angle-dependent PDF describing the $B_s^0 \to J/\psi\phi$ decays. As both the acceptance and time- and angle-dependent decay PDFs depend on the transversity angles, they must be normalized together. This normalization is done numerically during the likelihood fit. The PDF is normalized over the entire B_s^0 mass range of 5.150–5.650 GeV. The histograms showing 2D and 1D projections of the 4-dimensional acceptance maps in one selected bin produced by this method can be seen in Figure 8.5.

8.3.4 Combinatorial Background PDF

The background PDF has the following composition:

$$\begin{aligned}\mathcal{F}_{\mathrm{bkg}}(m_i, t_i, \sigma_{t_i}, \Omega_i, P_i(B|Q_x), p_{\mathrm{T}_i}) =& P_{\mathrm{b}}(m_i) \cdot P_{\mathrm{b}}(t_i|\sigma_{t_i}) \cdot P_{\mathrm{b}}(P_i(B|Q_x)) \\ & \cdot P_{\mathrm{b}}(\Omega_i) \cdot P_{\mathrm{b}}(\sigma_{m_i}|p_{\mathrm{T}_i}) \cdot P_{\mathrm{b}}(\sigma_{t_i}|p_{\mathrm{T}_i}) \cdot P_{\mathrm{b}}(p_{\mathrm{T}_i}).\end{aligned} \tag{8.8}$$

The background PDF accounts for the mass, time and angle distributions and similarly to the signal, the probability terms $P_{\mathrm{b}}(\sigma_{m_i}|p_{\mathrm{T}_i})$, $P_{\mathrm{b}}(\sigma_{t_i}|p_{\mathrm{T}_i})$, $P_{\mathrm{b}}(p_{\mathrm{T}i})$ and tagging probability term for background $P_{\mathrm{b}}(P(B|Q_x))$.

The combinatorial background mass model, $P_{\mathrm{b}}(m_i)$, is an exponential function with a constant term added.

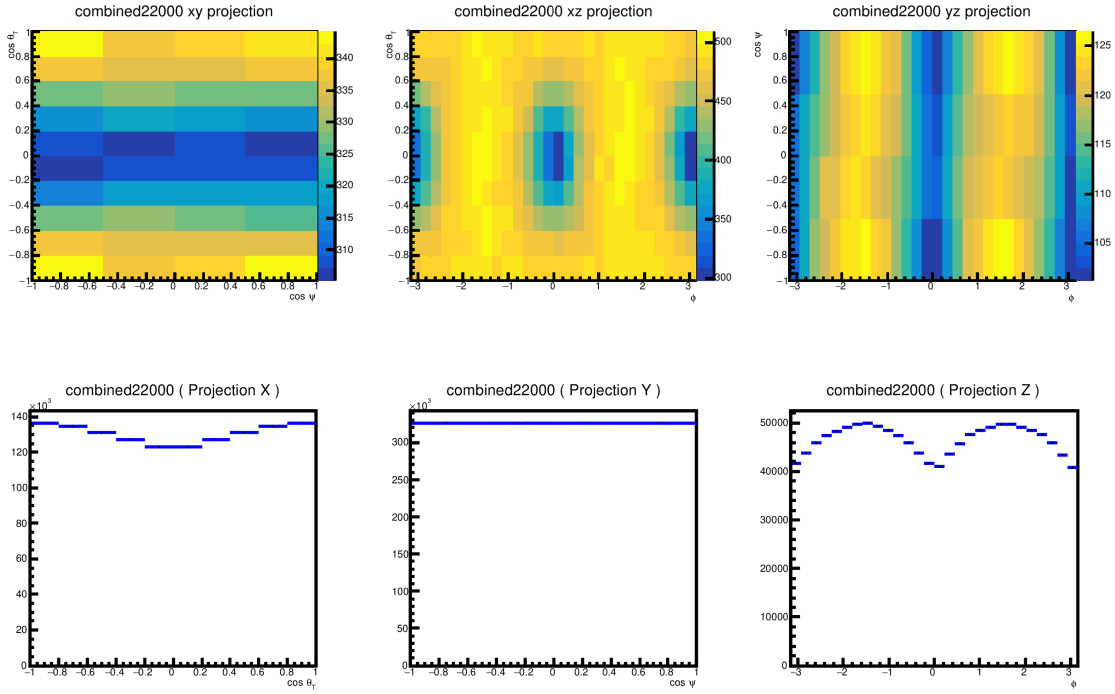

Figure 8.5: 2D projections (top) and 1D projections (bottom) of the 4-dimensional signal acceptance maps for the p_{T} bin (22–26 GeV).

Background Decay Time PDF

The proper decay time function $P_{\mathrm{b}}(t_i|\sigma_{t_i})$ is parameterized as a prompt peak modeled by a Gaussian distribution, two positive exponential functions and a negative exponential function. These functions are smeared with the same resolution function as the signal decay time-dependence, R_s (equation 8.6). The prompt peak models the combinatorial background events, which are expected to have reconstructed lifetimes distributed close to zero. The two positive exponential functions represent a fraction of longer-lived backgrounds with non-prompt J/ψ, combined with hadrons from the primary vertex or from a B/D meson in the same event. The negative exponential function takes into account events with poor vertex resolution.

Background Angular PDF

The shape of the combinatorial background angular distribution, $P_{\mathrm{b}}(\Omega_i)$ arises primarily from detector and kinematic sculpting. These angular distributions are described by

Legendre polynomial functions:

$$
\begin{aligned}
Y_l^m(\theta_T) &= \sqrt{(2l+1)/(4\pi)}\sqrt{(l-m)!/(l+m)!}P_l^{|m|}(\cos\theta_T), \\
P_k(x) &= \frac{1}{2^k k!}\frac{\mathrm{d}^k}{\mathrm{d}x^k}(x^2-1)^k, \\
P_{\mathrm{b}}(\theta_T,\psi_T,\phi_T) &= \sum_{k=0}^{6}\sum_{l=0}^{6}\sum_{m=-l}^{l}
\begin{cases}
a_{k,l,m}\sqrt{2}Y_l^m(\theta_T)\cos(m\phi_T)P_k(\cos\psi_T) & \text{where } m>0, \\
a_{k,l,m}\sqrt{2}Y_l^{-m}(\theta_T)\sin(m\phi_T)P_k(\cos\psi_T) & \text{where } m<0, \\
a_{k,l,m}\sqrt{2}Y_l^0(\theta_T)P_k(\cos\psi_T) & \text{where } m=0.
\end{cases}
\end{aligned}
\tag{8.9}
$$

The coefficients $a_{k,l,m}$ are adjusted to give the best fit to the angular distributions for events in the B_s^0 mass sidebands. The B_s^0 mass interval used for the background fit is between 5.150 and 5.650 GeV excluding the signal mass region $|(m(B_s^0) - 5.366\,\mathrm{GeV}| < 0.110\,\mathrm{GeV}$. In the nominal fit, the background angles are fitted by the Legendre polynomial of the 14^{th} order where the parameters $l = 14$ and $m = 14$. The combinatorial background angular distribution is sensitive to p_{T} of B_s^0 meson candidate. Hence the parameterization by Legendre polynomial functions is done for several p_{T} intervals: 10–15 GeV, 15–20 GeV, 20–25 GeV, 25–30 GeV, 30–35 GeV and $>$ 35 GeV. The most complicated shape of background angles is in the low p_{T} region below 15 GeV and is shown in the Figure 8.6.

8.3.5 Dedicated Backgrounds

The $B_s^0 \to J/\psi\phi$ events are contaminated by the $B_d \to J/\psi K^{0*}(K^{\pm}\pi^{\mp})$ and $\Lambda_b \to J/\psi p K^-$ decays misidentified as $B_s^0 \to J/\psi\phi$. Since the muons from J/ψ decay have a clean signature, the misidentification arises from the track reconstruction where the $\pi^{\pm}$ or p are misidentified as $K^{\pm}$. In the likelihood function, these contributions are accounted for through the $\mathcal{F}_{B_s^0}$ and $\mathcal{F}_{\Lambda_b}$ terms as described in equation 8.4. The shapes and parameters of the dedicated backgrounds are extracted from the fully-reconstructed MC samples with the intentionally misidentified tracks.

Fraction Evaluation

The fractions of these contributions, relative to the $B_s^0 \to J/\psi\phi$, are evaluated from a MC simulation using production and branching fractions from Refs. [4, 79, 80, 81, 82, 83]. The calculation of the relative fraction proceeds through following relations

$$
\begin{aligned}
f_{B_s^0} &= \frac{f_{B_d^0}}{f_{B_s^0}}\frac{\mathrm{Br}(B_d^0 \to J/\psi K^{0*})\cdot\mathrm{Br}(K^{0*}\to K^+\pi^-)}{\mathrm{Br}(B_s^0 \to J/\psi\phi)\cdot\mathrm{Br}(\phi\to K^+K^-)}\cdot\frac{\epsilon_{K^0}}{\epsilon_{B_s^0}}, \\
f_{\Lambda_b} &= \frac{f_{\Lambda_b}}{f_{B_s^0}}\frac{\mathrm{Br}(\Lambda_b \to J/\psi p K^-)}{\mathrm{Br}(B_s^0 \to J/\psi\phi)\cdot\mathrm{Br}(\phi\to K^+K^-)}\cdot\frac{\epsilon_{\Lambda_b}}{\epsilon_{B_s^0}},
\end{aligned}
\tag{8.10}
$$

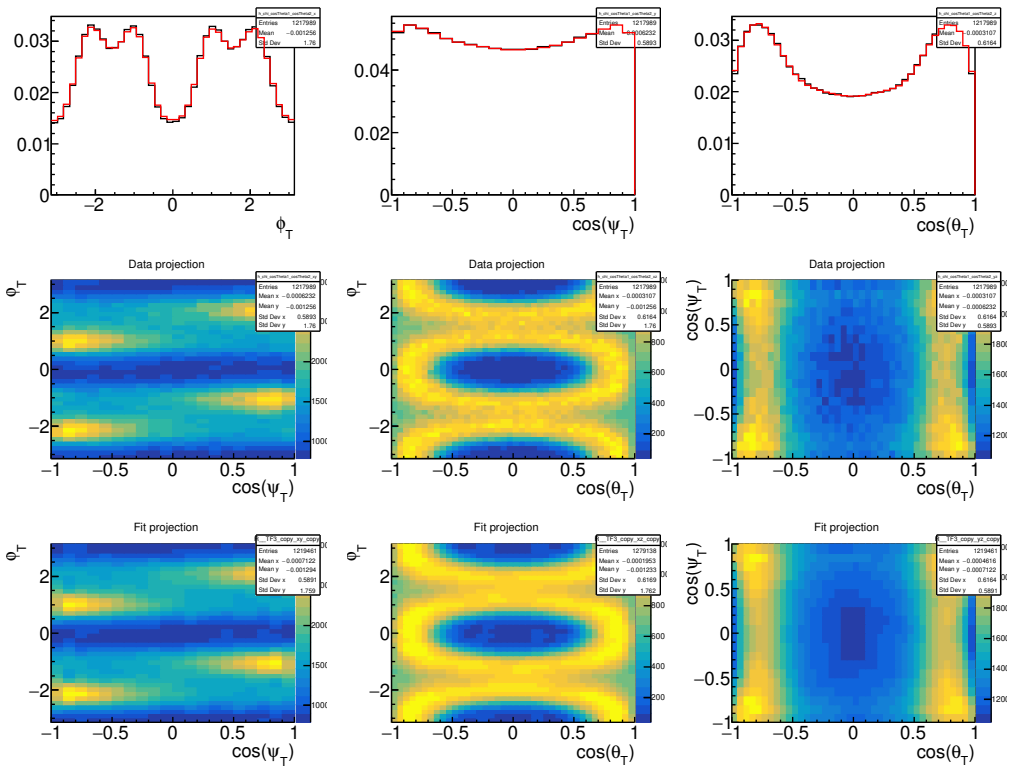

Figure 8.6: 1D projections (top) and 2D projections (middle and bottom) of the combinatorial background angular distribution in low p_{T} region below 15 GeV for events extracted from the B_s^0 mass sidebands.

where $f_{B_d^0}/f_{B_s^0}$ and $f_{\Lambda_b}/f_{B_s^0}$ are the ratio of fragmentation fractions of B_d^0, B_s^0 and Λ_b hadrons taken from the LHCb measurements [79, 80], the branching ratios $\mathrm{Br}(B_s^0 \to J/\psi\phi)$ and $\mathrm{Br}(\phi \to K^+K^-)$ use world average values [4], the product $\mathrm{Br}(B_d^0 \to J/\psi K^{0*}) \cdot \mathrm{Br}(K^{0*} \to K^+\pi^-)$ is evaluated from the total branching ratio for the $\mathrm{Br}(B_d^0 \to J/\psi K^+\pi^-)$ scaled by the p-wave contribution where both of these values are taken from the BaBar measurement [83], the $\mathrm{Br}(\Lambda_b \to J/\psi p K^-)$ is taken from other LHCb measurements [81, 82] and $\epsilon_{B_s^0}$, ϵ_{Λ_b} and ϵ_{K^0} are the selection efficiencies for background and signal decays multiplied by the acceptance. In total, the evaluated relative fractions are $f_{B_d^0} = (4.4 \pm 0.5)\%$ and $f_{\Lambda_b} = (2.1 \pm 0.6)\%$.

Mass Shape Contribution

The masses of the B_d^0 and Λ_b contributions are evaluated from the MC simulation. Due to wrong mass assignment of the tracks, the shapes of mass distribution passing fiducial, trigger and B_s^0 selection cuts are distorted from the generated distributions.

The B_d^0 mass shape is fitted by the sum of three independent Gaussian functions as

can be seen in Figure 8.7.

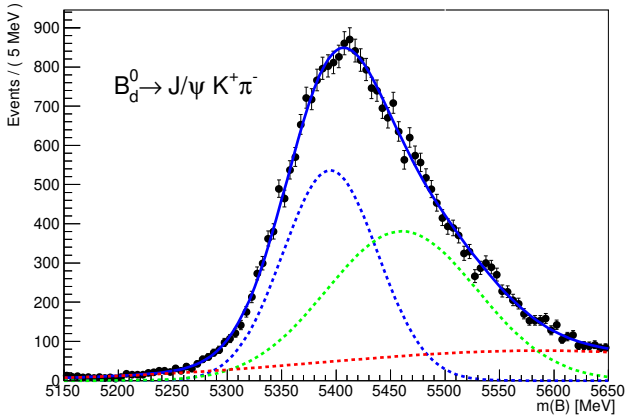

Figure 8.7: The $B_d^0 \to J/\psi K^+\pi^-$ mass distribution used in the maximum likelihood fit with three Gaussian components.

The mass shape of Λ_b is more complex than the B_d^0 and this is the reason why the simulated events were re-weighted at the generator level to match the expected $m(pK^-)$ distributions measured by the LHCb experiment [84]. After the wrong mass assignment, the Λ_b mass distributions are used to populate a histogram of 40 equal width bins over the mass range of the B_s^0 fit. Due to limited sample size, the smoothing procedure was used to remove statistical fluctuations. The resulting histogram shown in Figure 8.8 is than used as the probability function in the overall fit.

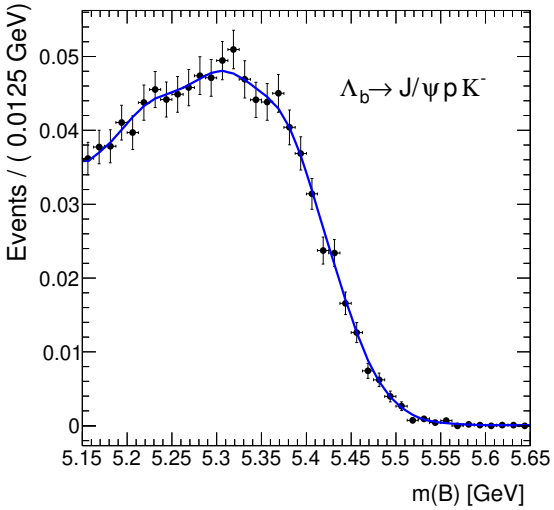

Figure 8.8: The $\Lambda_b \to J/\psi pK^-$ mass distribution used in the maximum likelihood fit.

Angular Shape Distribution

MC simulated events are also used to determine the shape of the mass and transversity angle distributions. The 3D angular distributions of $B_d^0 \to J/\psi K^{*0}$ and of the conjugate decay are modelled using input from Ref. [85], while angular distributions for $\Lambda_b \to J/\psi p K^-$ and the conjugate decay are modelled as flat. The charge-conjugate decay is simulated by swapping the changes on the pK^- pair on the half of the statistics obtained from MC simulation. These distributions are sculpted for detector acceptance effects and then described by Legendre polynomial functions of 10^{th} order, see equation 8.9. Obtained shapes of the angular distributions are depicted in Figures 8.9 and 8.10 and are fixed in the total fit.

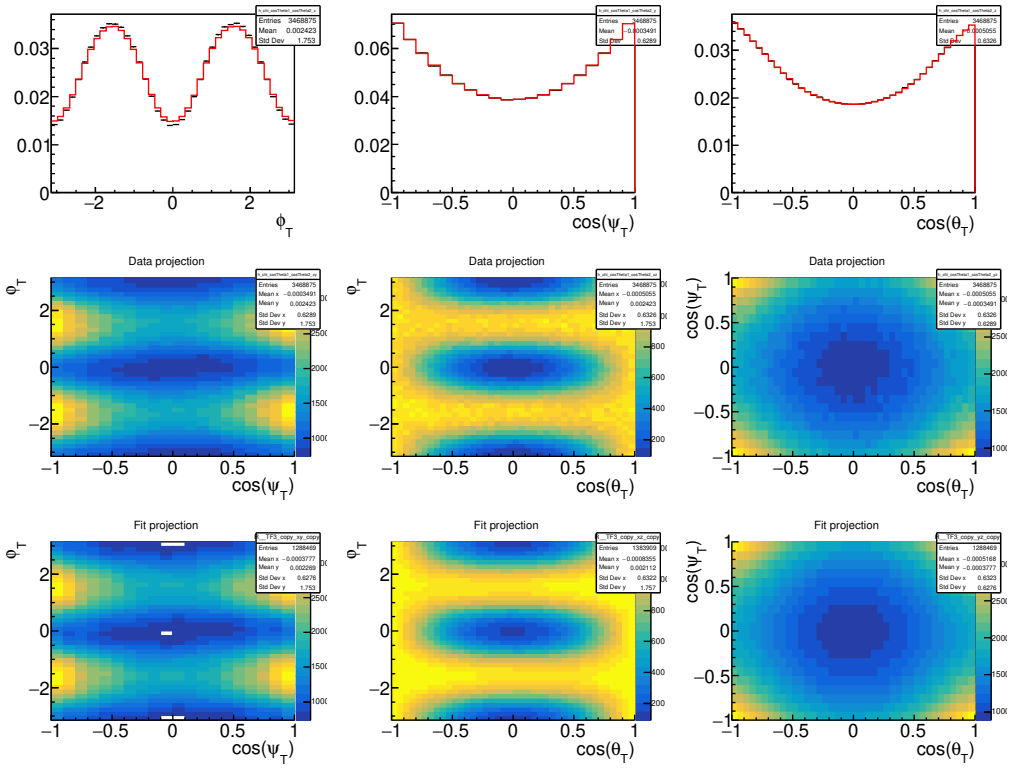

Figure 8.9: 1D projections (top) and 2D projections (middle and bottom) of the fitted transversity angular distributions for $B_d^0 \to J/\psi K^{0*}$.

Pseudo Lifetime Estimation

The B_d and Λ_b lifetimes are accounted for in the fit by adding additional exponential terms convoluted by the Gaussian resolution, same as for signal and background defined in equation 8.6. The slope of the exponential is given by the lifetime of B_d and Λ_b scaled

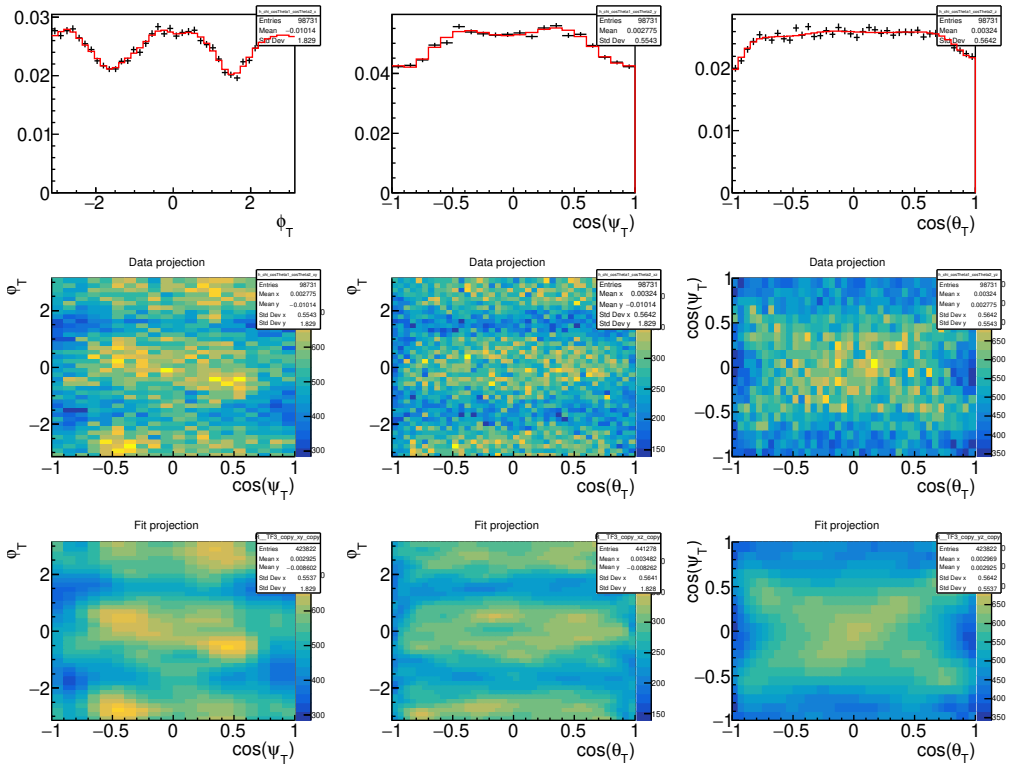

Figure 8.10: 1D projections (top) and 2D projections (middle and bottom) of the fitted transversity angular distributions for $\Lambda_b \to J/\psi p K^-$.

by the ratio of $m(B_d)/m(B_s^0)$ or $m(\Lambda_b)/m(B_s^0)$ masses to account for the misidentification, where the parameters are taken from the world average values [4].

8.3.6 Muon Trigger Proper Decay Time-Dependent Efficiency

It has been observed that the muon trigger biases the transverse impact parameter of muons toward larger values, resulting in minor inefficiency at large values of proper decay times. In the early 2016 data, some of the triggers were affected by the larger bias due to trigger inefficiency. This inefficiencies are measured using a large sample of 10^8M MC simulated events, by comparing the B_s^0 proper decay time distribution of an unbiased sample with the distribution obtained after including the trigger. The time efficiency was fitted by a function defined as:

$$w(t) = p_0 \cdot [1 - p_1 \cdot (Erf((t - p_3)/p_2) + 1)], \tag{8.11}$$

where t is proper decay time and p_0, p_1, p_2 and p_3 are parameters of the fit to MC events. In addition, the fit function w is normalized in the way that $w(0) = 1$. The fit was done

to the most significant triggers used in the analysis for each data period with different conditions separately. The data from years 2015 and 2017 did not indicate triggers with extra lifetime bias and are grouped into two separate groups. However, the 2016 data contain the group of triggers with higher lifetime bias at the beginning of the data taking, which was corrected after the run number 302737. The 2016 triggers are than divided into three groups: biased triggers before correction, unbiased triggers before correction labeled 2016A and triggers after correction labeled 2016B. The lifetime correction for each group can be seen in Figure 8.11.

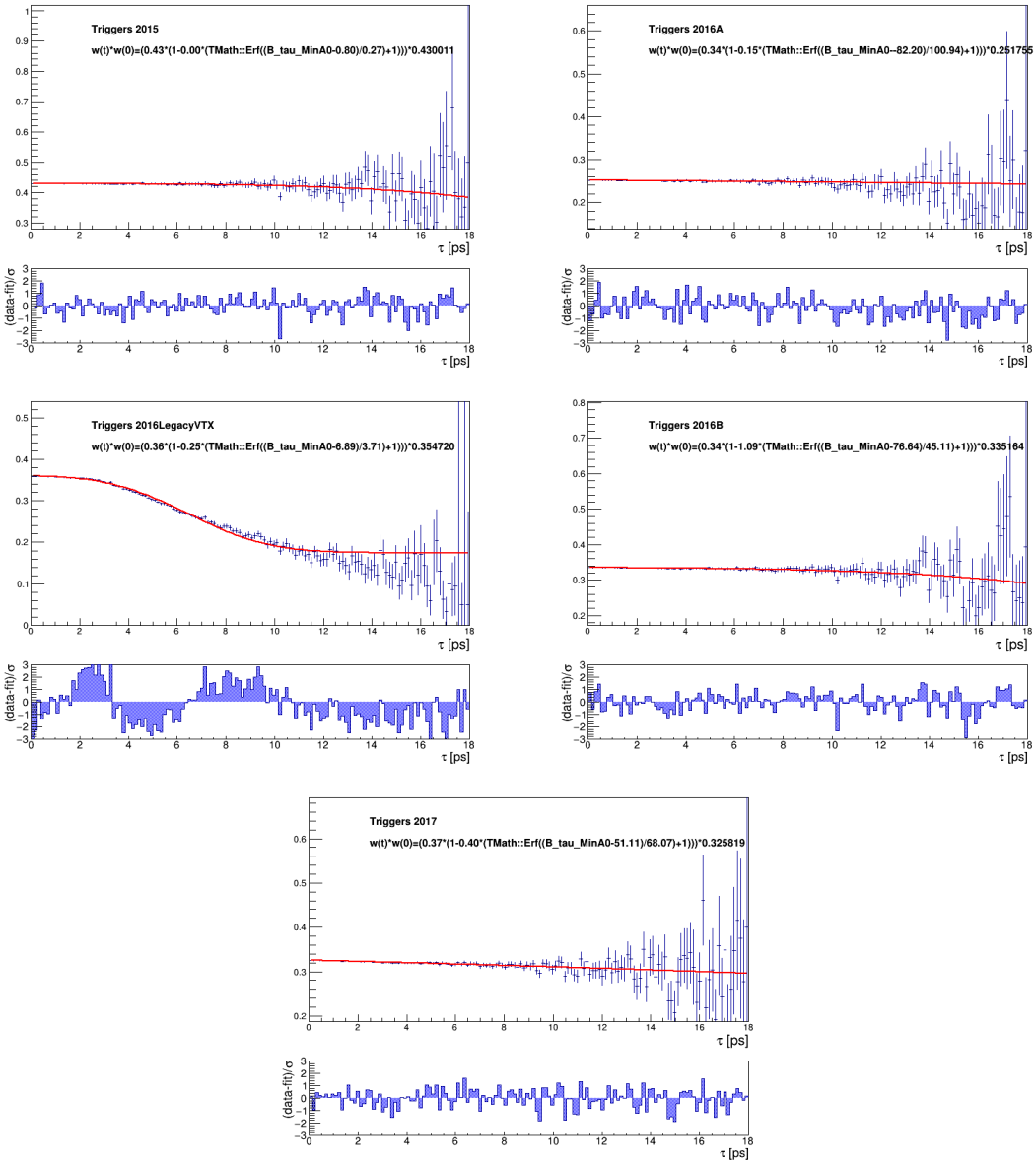

Figure 8.11: The overview of the lifetime corrections for each trigger group is shown.

This was then used in the B_s^0 fit, where in order to account for this inefficiency, the events are re-weighted by a factor w defined in equation 8.11.

8.3.7 Conditional Probability Distributions

As discussed above, the conditional probability distributions, the Punzi terms, are included in the Likelihood function to account for the probability distributions of the conditional observables that can not be factorized out of the likelihood function. The likelihood used in this analysis, is dependent on mass error σ_{m_i}, lifetime error σ_{t_i}, transverse momentum p_{T_i} and tag probability $P(B|Q_x)$ of B_s^0 candidates. The distributions of the first three variables are explained in this section while the last variable $P(B|Q_x)$ is described in the dedicated flavour tagging section 8.4.

Since the mass and time uncertainty distributions are dependent on the p_{T} of the B_s^0 candidates, the Punzi distributions are made in p_{T} bins defined as follows: 10–14.5 GeV, 14.5–17 GeV, 17–21 GeV, 21–35 GeV, 35–45 GeV and $>$ 45 GeV. For each of these bis, distributions of signal and background component are extracted from the data using the sideband subtraction, where the signal fraction is calculated from the simple B_s^0 mass fit. In the simple B_s^0 mass fit, the mass distribution is described by the sum of three Gaussian functions with a common mean for the signal and the exponential plus a constant for the background. The signal window is defined as $|m(B_s^0) - 5.366| > 0.11$ GeV while the rest is assumed to be background.

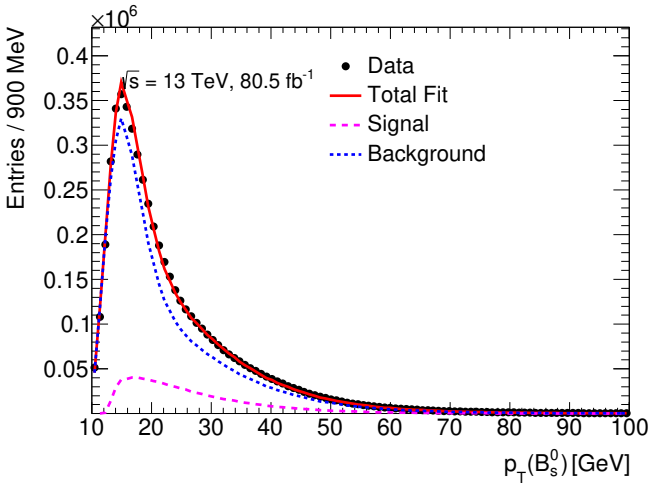

Figure 8.12: The probability distribution function of the transverse momentum.

To extract probability distributions from signal and sideband regions, two approaches are used. The first method is based on fitting the distributions by the sum of two or three Gamma functions. However, this approach is time consuming since the sum of three

Gamma functions has 11 free parameters. The second approach is based on the histogram extraction from the region of interest which is time efficient. However, this method needs sufficient data sample size in each bin to get well described distributions close to to smooth curves. The extracted Punzi distributions can be seen in Figures 8.12, 8.13 and 8.14.

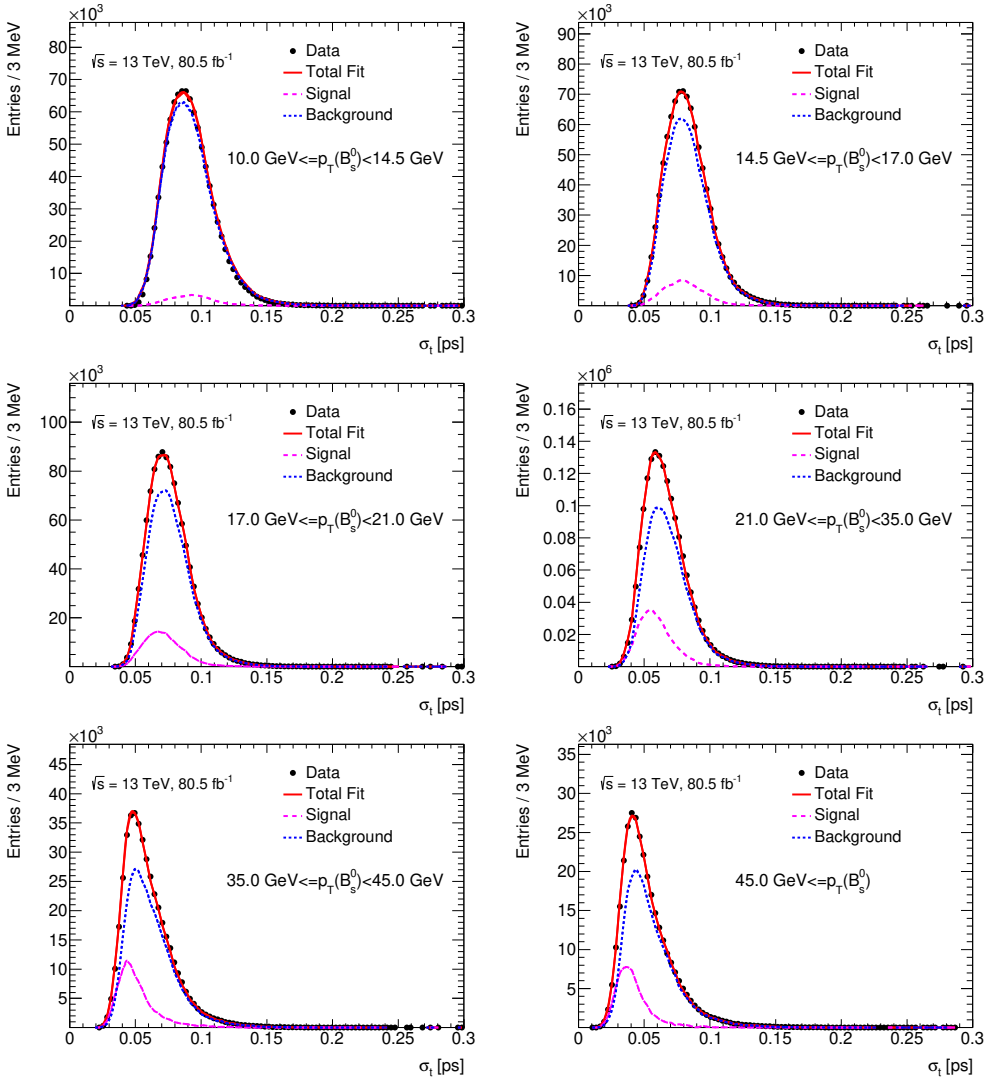

Figure 8.13: The probability distribution function of the time uncertainty plotted in bins of transverse momentum.

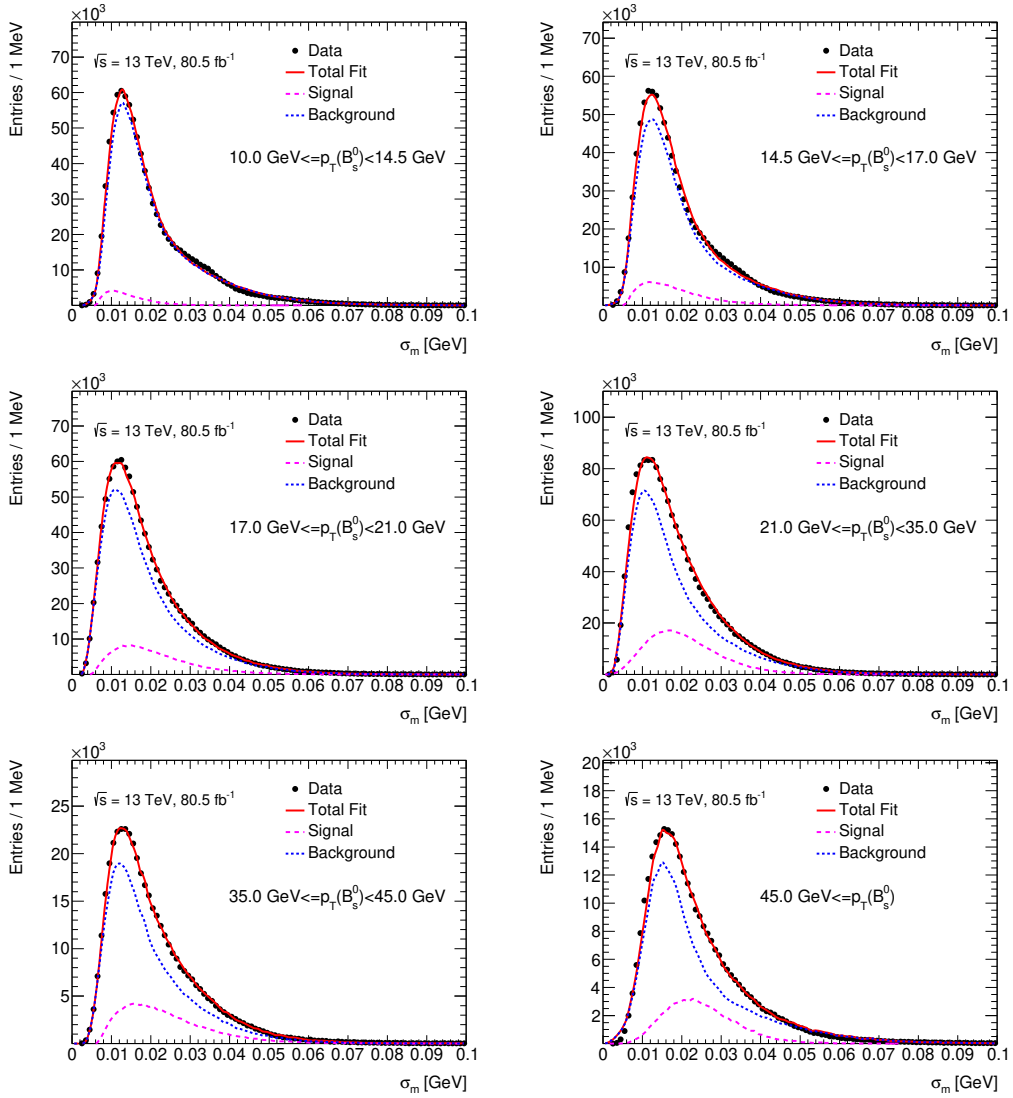

Figure 8.14: The probability distribution function of the mass uncertainty plotted in bins of transverse momentum.

8.4 Flavour Tagging

The initial flavour of a neutral B-meson can be inferred using information from a method called flavour tagging. The flavour tagging methods can be categorized into two groups: Same-Side tagging (SST) and Opposite-Side tagging (OST). The OST method is based on the fact that at the LHC b-quarks are produced in pairs with opposite charge. It uses the information from the opposite-side B-meson decay that contains the other pair-

produced b-quark in the event. If one can identify the opposite side b-quark flavour, it is possible to identify the initial flavour of the quark in the B_s^0 meson at the time of the production. The SST methods exploit the correlation with particles produced in the hadronization process of the signal B-meson to find associated fragment tracks that could identify the flavour of the produced B_s^0 meson.

The flavour tagging used in this analysis is based on the OST methods and it is calibrated using events containing $B^{\pm} \to J/\psi K^{\pm}$ decays as described in section 8.4.3. In order to extract the tag probability of the B_s^0 meson, the procedure described in following sections has to be performed.

8.4.1 Flavour Tagging Parameters

In order to quantify the quality of each tagging method the following variables need to be defined: tag efficiency ϵ_{tag}, the tag dilution $\mathcal{D}_{tag}$ and the tagging power P_{tag}. The tag efficiency is defined as ratio

$$\epsilon_{tag} = \frac{N_{tag}}{N_{tot}}, \tag{8.12}$$

where N_{tag} is the number the B events which are able to be tagged by the selected tagging method and N_{tot} is the total number of B events in the sample.

The dilution is a variable that describes the purity of the selected tagging method as follows:

$$\mathcal{D}_{tag} = \frac{N_r - N_w}{N_r + N_w} = 1 - 2w_{tag}, \tag{8.13}$$

where the N_r is the number of correctly tagged events, N_w is the number of wrong tagged events and w_{tag} is called the wrong tag fraction defined as

$$w_{tag} = \frac{N_w}{N_r + N_w}. \tag{8.14}$$

The tagging power is defined as

$$P_{tag} = \epsilon_{tag}\mathcal{D}_{tag}^2. \tag{8.15}$$

The tag power is a figure of merit to compare the different tagging methods between experiments and it is not directly used in the calibration to B_s^0 sample.

8.4.2 Flavour Tagging Methods

This analysis uses four types of the OST methods. Three of them are based on the $b \to l$ transitions and one is using the information from the reconstructed b-tagged jets. The lepton based tagging is performed by the muon and electron taggers, where two categories

of muons are identified, *Low-*p_{T} and *Tight* muons. The lepton tagging is a clean tagging method; however, it is diluted by the $b \to c \to l$ transition and occurs in a small fraction of the reconstructed B_s^0 events. On the other hand, the b-tagged jets method is present in many reconstructed B_s^0 events; however, the precision of this method is coarser than the lepton tagging. In case of more identified taggers in one reconstructed event, the tag method with better precision is used, as can be shown in diagram 8.15. If the reconstructed event does not contain tag information, the tag probability is set to 0.5.

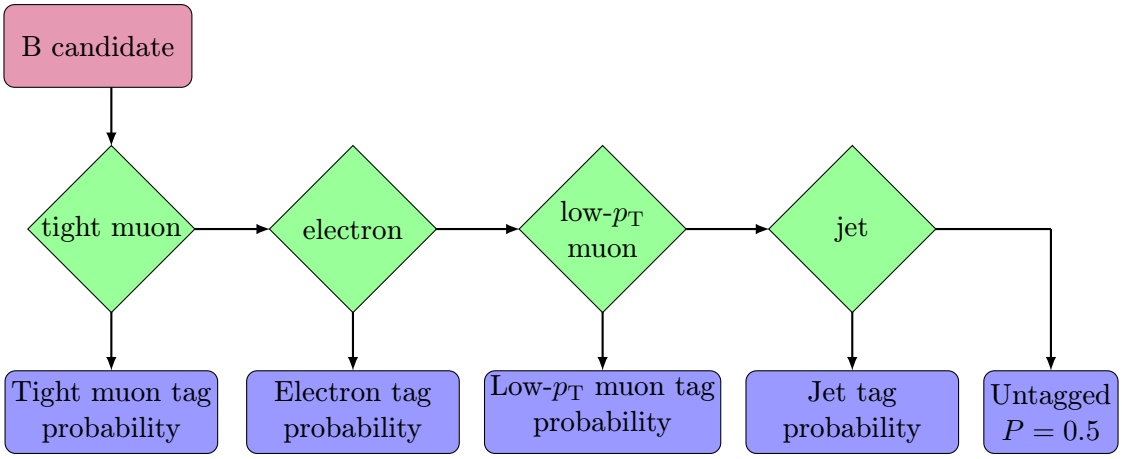

Figure 8.15: Diagram of the tag method selection.

Cone Charge

In order to optimize the tagging performance, the cone charge variable Q_x is used as discriminating variable for events passing the selection criteria. The cone charge is calculated as follows

$$Q_x = \frac{\sum_i^{N_{trk}} q_i (p_{\mathrm{T}_i})^\kappa}{\sum_i^{N_{trk}} (p_{\mathrm{T}_i})^\kappa}, \tag{8.16}$$

where N_{trk} is the number of tracks in the cone $\Delta R = \sqrt{(\Delta\eta)^2 + (\Delta\phi)^2}$ around the lepton or jet direction, the p_{T} and q_i are the transverse momentum and charge of each track in the cone and κ is the constant used to maximize the tag power.

Looking at the distribution of the cone charge variable, two subcategories are considered: the first discrete category and second continuous category. The discrete category is used in the case where the cone charge is formed either from only one track or from more than one track of the same charge. This results in a cone charge of $Q = \pm 1$. The second continuous category is used when more than one track is in the cone, and the sum contains tracks of both negative and positive charge.

Tag Calibration and Tag Probability

To study and calibrate the OST methods, events containing $B^{\pm} \to J/\psi K^{\pm}$ decays are used. The $B^{\pm} \to J/\psi K^{\pm}$ decay was selected as the calibration sample because it is a non-oscillating channel with high statistics and the initial flavour of the $B^{\pm}$ meson is given by the kaon charge. The $B^{\pm}$ reconstruction and candidate selection is described in section 8.4.3. Using the $B^{\pm}$ data sample, the cone charge probability distributions $P(Q|B^{+})$ and $P(Q|B^{-})$ can be extracted.

In order to transfer the tag information provided by the $B^{\pm}$ calibration sample to the B_s^0 events, the tag probability variable is used. The tag probability $P(B|Q_x)$ gives a probability to find the B-meson containing a $\bar{b}$-quark in the initial state for a given cone charge Q. The tag probability is defined to be

$$P(B|Q_x) = \frac{P(Q|B^{+})}{P(Q|B^{+}) + P(Q|B^{-})}, \tag{8.17}$$

and a related probability to find b-quark is $P(\bar{B}|Q) = 1 - P(B|Q_x)$. This value is than incorporated into the likelihood function. The summary of tagging performances for the different flavour tagging methods on the sample of $B^{\pm}$ signal candidates can be seen in Table 8.1.

Tag method	ϵ_x [%]	D_x [%]	T_x [%]
Tight muon	4.50 ± 0.01	43.8 ± 0.2	0.862 ± 0.009
Electron	1.57 ± 0.01	41.8 ± 0.2	0.274 ± 0.004
Low-p_{T} muon	3.12 ± 0.01	29.9 ± 0.2	0.278 ± 0.006
Jet	12.04 ± 0.02	16.6 ± 0.1	0.334 ± 0.006
Total	21.23 ± 0.03	28.7 ± 0.1	1.75 ± 0.01

Table 8.1: Summary of tagging performances for the different flavour tagging methods used in the $B_s^0 \to J/\psi\phi$ analysis calibrated on the sample of $B^{\pm}$ signal candidates shown with statistical uncertainty only.

Muon Tagging

For muon-based tagging, at least one additional muon is required in the event, with $p_{\mathrm{T}} > 2.5$ GeV, $|\eta| < 2.5$ and with $|\Delta z| < 5$ mm, where $|\Delta z|$ is the difference in z between the primary vertex and the longitudinal impact parameter of the ID track associated with the muon. Muons are classified and kept if their identification quality selection working point is either *Tight* or *Low-*p_{T}; these categories are subsequently treated as distinct flavour tagging methods. For muons with $p_{\mathrm{T}} > 4$ GeV, *Tight* muons are the dominant

category, with the *Low-*p_{T} requirement typically identifying muons of $p_{\mathrm{T}} < 4$ GeV. In the case of multiple muons satisfying selection criteria in one event, *Tight* muons are chosen over *Low-*p_{T} muons. Within the same muon category, the muon with the highest p_{T} that passes the selection is used.

A muon cone charge variable, Q_μ, is constructed according to equation 8.16, with $\kappa = 1.1$ and the sum over the reconstructed ID tracks within a cone of size $\Delta R = 0.5$ around the muon direction. These tracks must have $p_{\mathrm{T}} > 0.5$ GeV, $|\eta| < 2.5$, and $|\Delta z| < 5$ mm. Tracks associated with the decay of a B-meson signal candidate are excluded from the sum. In each interval of Q_μ, a fit to the $J/\psi K^{\pm}$ invariant mass spectrum is performed and the number of signal events is extracted. The fit model used is described in section 8.4.3. Figure 8.16 shows the distributions of the muon cone charge using $B^{\pm}$ signal candidates for *Tight* muons, and includes the tagging probability as a function of the cone charge variable. The corresponding distributions for *Low-*p_{T} muons are shown in Figure 8.17.

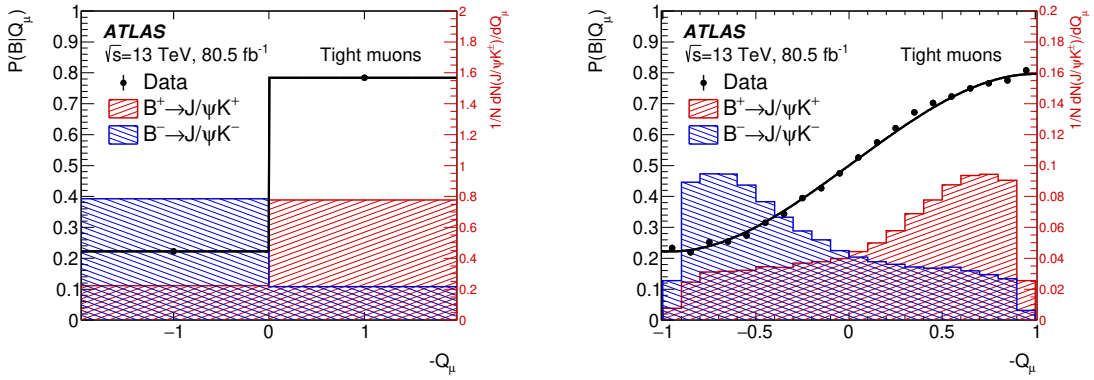

Figure 8.16: Normalized cone charge distributions (shown against the right axis scale), $-Q_\mu$, for B^+ (B^-) events shown in red (blue) for *Tight* muons, for cases of discrete charge (left), and for the continuous distribution (right). Superimposed is the distribution of the tagging probability, $P(B|Q_\mu)$.

Electron Tagging

Electrons are identified using ID and calorimeter information, and must satisfy the *Medium* electron quality criteria [86]. The ID track associated with the electron is required to have $p_{\mathrm{T}} > 0.5$ GeV, $|\eta| < 2.5$, and $|\Delta z| < 5$ mm. To reject electrons from the signal-side of the decay, electrons with $\cos(\zeta_b) > 0.93$, where ζ_b is the opening angle between the momentum of the signal B-meson candidate and the electron momentum, are not considered. In the case of more than one electron passing the selection, the electron with

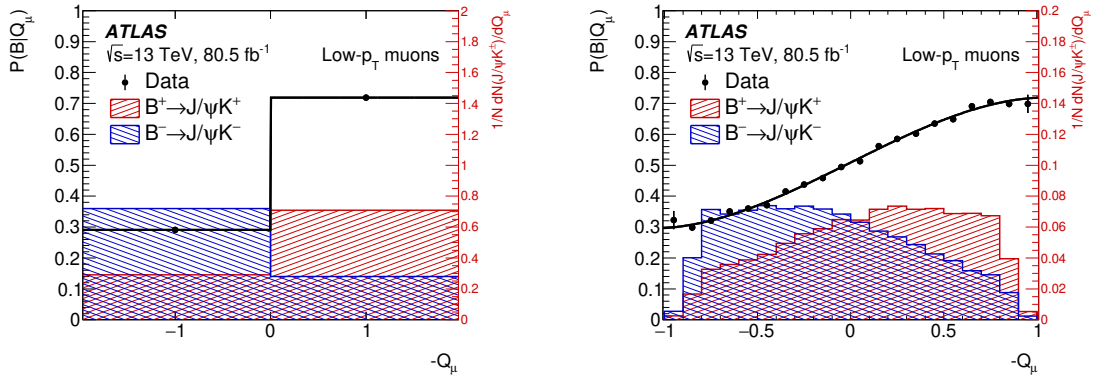

Figure 8.17: Normalized cone charge distributions (shown against the right axis scale), $-Q_\mu$, for B^+ (B^-) events shown in red (blue) for *Low-*p_{T} muons, for cases of discrete charge (left), and for the continuous distribution (right). Superimposed is the distribution of the tagging probability, $P(B|Q_\mu)$.

the highest p_{T} is chosen. Charged-particle tracks within a cone of size $\Delta R = 0.5$ are used to form the electron cone charge Q_e, constructed according to equation 8.16, with $\kappa = 1.0$. The resulting electron cone charge distributions are shown in Figure 8.18, together with the corresponding tagging probability.

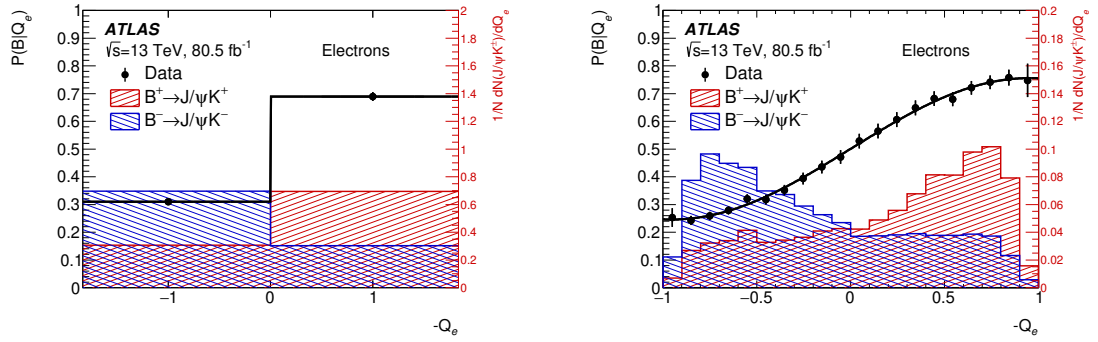

Figure 8.18: Normalized cone charge distributions (shown against the right axis scale), $-Q_e$, for B^+ (B^-) events shown in red (blue) for electrons, for cases of discrete charge (left), and the continuous distribution (right). Superimposed is the distribution of the tagging probabilities, $P(B|Q_e)$.

Jet Tagging

In the absence of a muon or an electron, a jet identified as containing a B-hadron is required. Jets are reconstructed from calorimetric information [87] using the anti-k_t algorithm [88, 89] with a radius parameter $R = 0.4$. The identification of a b-tagged jet

uses a multivariate algorithm *MV2c10* [90], utilizing boosted decision trees (BDT), which output a classifier value. Jets are selected if this value exceeds 0.56. This value is chosen to maximise the tagging power of the calibration sample. In the case of multiple selected jets, the jet with the highest value of the BDT output classifier is used. Jets associated with the signal decay are not considered in this selection.

Tracks within a cone of size $\Delta R = 0.5$ around the jet axis are used to define a jet cone charge, Q_{jet}, constructed according to equation 8.16, where $\kappa = 1.1$ and the sum is over the tracks associated with the jet, with $|\Delta z| < 5$ mm, and excluding tracks from the decay of the signal B-meson candidate. Figure 8.19 shows the distribution of the opposite-side jet cone charge for $B^{\pm}$ signal candidates.

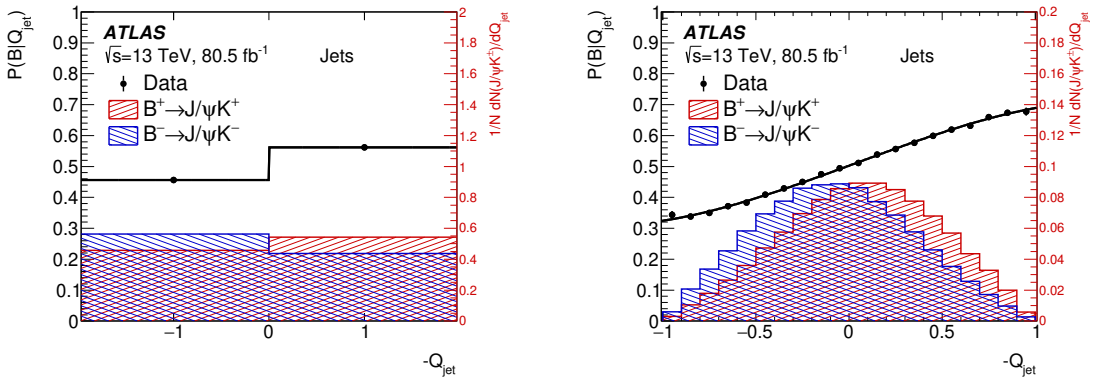

Figure 8.19: Normalised cone charge distributions (shown against the right axis scale), $-Q_{\text{jet}}$, for B^+ (B^-) events shown in red (blue) for jets, for cases of discrete charge (left), and the continuous distribution (right). Superimposed is the distribution of the tag probability, $P(B|Q_{\text{jet}})$.

8.4.3 The $B^{\pm} \to J/\psi K^{\pm}$ Event Selection

Candidate $B^{\pm} \to J/\psi K^{\pm}$ decays are identified in a series of steps. First, J/ψ candidates are selected from oppositely charged muon pairs forming a good vertex, as described in section 8.2. Each muon is required to have $p_{\text{T}} > 4\,\text{GeV}$ and $|\eta| < 2.5$. Dimuon candidates with invariant mass $2.8 < m(\mu^+\mu^-) < 3.4$ GeV, as determined from the re-fitted track parameters of the vertex, are retained for further analysis. To form the $B^{\pm}$ candidate, an additional track is required, which is not identified as an electron or muon. The track is assigned the charged-kaon mass hypothesis and combined with the dimuon candidate using a vertex fit, performed with the mass of the dimuon pair constrained to the J/ψ mass. Prompt background contributions are suppressed by a requirement on the proper decay time of the $B^{\pm}$ candidate of $t > 0.2$ ps.

The tagging probabilities are determined from B^+ and B^- signal events. These signal yields are derived from fits to the invariant mass distribution, $m(J/\psi K^\pm)$, and performed in intervals of the discriminating variables. To describe the $B^\pm \to J/\psi K^\pm$ signal, two Gaussian functions with a common mean are used. An exponential function is used to describe the combinatorial background and a hyperbolic tangent function to parameterise the low-mass contribution from incorrectly or partially reconstructed B-hadron decays. A Gaussian function is used to describe the $B^\pm \to J/\psi\pi^\pm$ contribution, with fixed parameters taken from simulation except for the normalisation, which is a free parameter. A fit to the overall mass distribution is used to define the shapes of signal and backgrounds. Subsequent fits are performed in the intervals of the tagging discriminating variables, separately for B^+ and B^- candidate events, with the normalisations and also the slope of the exponential function left free. The B^+ and B^- signal yields are extracted from these fits. Figure 8.20 shows the invariant mass distribution of $B^\pm$ candidates overlaid with a fit to all selected candidates, including the individual fit components for the signal and backgrounds.

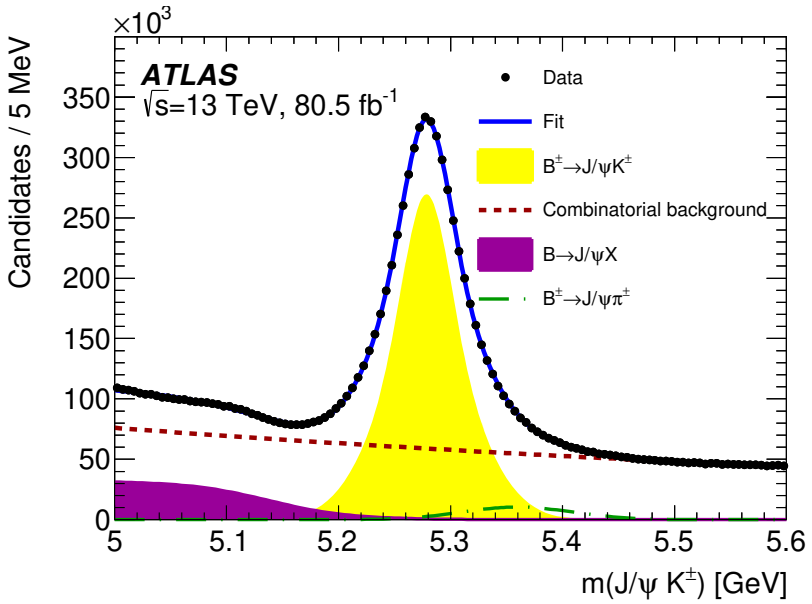

Figure 8.20: The invariant mass distribution for selected $B^\pm \to J/\psi K^\pm$ candidates. Data are shown as points, and the overall result of the fit is given by the blue curve. The contributions from the combinatorial background component are indicated by the red dotted line, partially reconstructed B-hadron decays by the purple shaded area, and decays of $B^\pm \to J/\psi\pi^\pm$, where a pion is misidentified as a kaon, by the green dashed line.

8.4.4 Tag Punzi Distributions

Since the distributions of $P(B|Q_x)$ from signal B_s^0 mesons and backgrounds can be expected to be different, separate PDFs are necessary to describe these distributions in the likelihood function as described in section 8.3.7. These PDFs are defined as $P_{\rm s}(P(B|Q_x))$ and $P_{\rm b}(P(B|Q_x))$, describing the probability distributions for signal and background, respectively, and are derived from the sample of B_s^0 candidates. As described in section 8.4.2, cone charge distribution can be categorized into the discrete and continuous part. Thus the tag Punzi distributions must be evaluated for both of these categories as well.

The discrete part, also called spikes, is using simple event counting where the number of signal and background events is evaluated using sideband subtraction. The fraction of events f_{+1} and f_{-1} with cone charges $+1$ and -1 are evaluated for each tagging method. Obtained results can be seen in Table 8.2.

Tag method	Signal		Background	
	f_{+1} [%]	f_{-1} [%]	f_{+1} [%]	f_{-1} [%]
Tight muon	6.9 ± 0.3	7.5 ± 0.3	4.7 ± 0.1	4.9 ± 0.1
Electron	20 ± 1	19 ± 1	16.8 ± 0.2	17.3 ± 0.2
Low-$p_{\rm T}$ muon	10.9 ± 0.5	11.6 ± 0.5	7.0 ± 0.1	7.5 ± 0.1
Jet	3.60 ± 0.15	3.54 ± 0.15	3.05 ± 0.03	3.17 ± 0.03

Table 8.2: Fractions f_{+1} and f_{-1} of events with cone charges of $+1$ and -1, respectively, for signal and background events and for the different tagging methods. Only statistical uncertainties are given.

The remaining fraction of events $1 - f_{+1} - f_{-1}$ corresponds to the continuous part of the distribution. In order to describe continuous part of the tag Punzi distributions, the sideband-subtraction method was used. The background component was fitted by a function in the sideband region, while the signal component is fitted in the signal region with a fixed shape and a fraction of background component. The functions describing the continuous part of the tag Punzi distributions for each of the four tagging methods are presented in Figure 8.21.

8.5 Systematic Uncertainty Studies

The likelihood function includes not only physical parameters, but also other parameters referred to as "nuisance parameters", such as: the B_s^0 signal fraction f_s, parameters describing the invariant mass and decay time-angular distributions of combinatorial background events and scale factors of mass and decay time uncertainties. In addition, there are also other nuisance parameters describing acceptance functions, parameterizations of

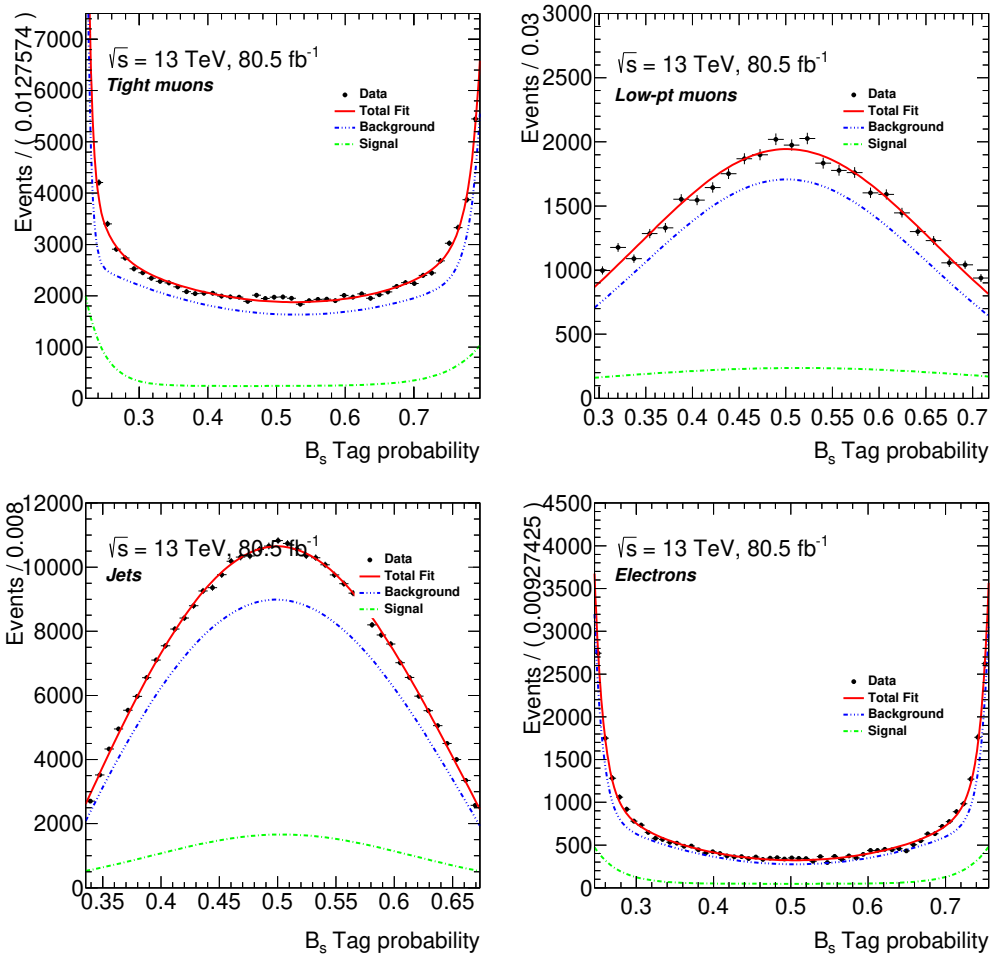

Figure 8.21: Tag Punzi PDF for the continuous part of the cone charge distribution for *Tight* muons (top, left), *Low-*p_{T} muons (top, right), jets (bottom, left) and electrons (bottom, right).

the angles of dedicated backgrounds $B_d \to J/\psi K^{0*}$ and $\Lambda_b \to J/\psi p K^-$ and their fractions f_{B^0} and f_{Λ_b}, the probability density functions of time error distributions $P(\sigma_{t_i}|p_{\mathrm{T}_i})$, mass error distributions $P(\sigma_{m_i}|p_{\mathrm{T}_i})$, p_{T} distributions $P(p_{\mathrm{T}_i})$ and tagging parameters and calibrations. These parameter values are mainly fixed in the fit to the values extracted from the B_s^0 mass signal and sideband regions or from MC simulations.

To each source of the nuisance parameters, the systematic effect on the physical parameters is evaluated. Other sources of possible systematic deviations arise from the PDF modeling, event reconstruction or MC limitation. The extracted systematic uncertainties for each tested effect that is not negligible are described below.

- **Flavour tagging:** The effects on the main physics parameters from the fit, due to

uncertainties introduced by the flavour tagging procedure are assessed as follows. The statistical uncertainty due to the size of the sample of $B^\pm \to J/\psi K^\pm$ decays is included in the overall statistical uncertainty. The systematic uncertainty arising from the precision of the OST calibration, described in section 8.4, is estimated by changing the models used to parameterize the probability distribution, $P(B|Q_x)$, as a function of the cone charge from the function used by default (a third-order polynomial for muons and a sinusoid for electrons) to one of several alternative functions: a linear function; a fifth-order polynomial; or two third-order polynomials that describe the positive and negative regions and have common constant and linear terms, but independent quadratic and cubic terms. The B_s^0 fit is repeated using the alternative models and the largest deviation from the nominal fit is assigned as the systematic uncertainty. To validate the calibration procedure, calibration curves are derived from simulated samples of $B^\pm$ and B_s^0 signals. The variations between the curves from these two samples are propagated to the calibration curves derived from data. The differences in the parameter values between the nominal fit and that with the varied calibration curves are included in the systematic uncertainty.

An additional systematic uncertainty is assigned to account for potential dependencies on the pile-up distribution. The calibration data are split into subsets of approximately equal size, separated according to the estimated pile-up of the event, and separate calibrations are made for each subset. For the B_s^0 fit, the fit is repeated using the calibrations corresponding to the estimated pile-up of that event. Differences between the nominal and the modified fit for the parameters of interest are taken as the systematic uncertainty. For the terms $P_{\mathrm{b}}(P(B|Q_x))$ and $P_{\mathrm{s}}(P(B|Q_x))$, variations of the parameterization are considered (including using histograms in place of parameterization). The resulting changes in the parameter values of the B_s^0 fit are similarly included in the systematic uncertainties.

- **Angular acceptance method:** The angular acceptance of the detector and the kinematic cuts, $A(\Omega_i, p_{\mathrm{T}_i})$, described in section 8.3.3, is calculated from a binned fit to MC simulated data. In order to estimate the systematic uncertainty introduced by the choice of binning, different acceptance functions are calculated using different bin widths and central values.

- **ID alignment:** The effect of a radial expansion on the measured d_0 is determined from data collected at 13 TeV, with a trigger requirement of at least one muon with a transverse momentum greater than or equal to 4 GeV. The radial expansion uncertainties determined this way are 0.14% for $|\eta| < 1.5$ and 0.55% for $1.5 < |\eta| < 2.5$. These values are used to estimate the effect on the fitted B_s^0 parameter values.

Small deviations are seen in some parameters, and these are included as systematic uncertainties.

- **Trigger efficiency:** To correct for the proper decay time dependence of trigger inefficiencies, the events are re-weighted according to equation. 8.11. An alternative fit is performed using different sets of binning as well as the range of the lifetimes in the MC sample used to determine the efficiency. The systematic effects are found to be negligible.

- **Best candidate selection:** In the fit, there exist $\approx 5\%$ of events that are found to contain multiple candidates after selection cuts. By default, the candidate with the lowest χ^2/ndof is selected. The systematic uncertainty of the B_s^0 fit from the selection of the lowest χ^2/ndof candidates is tested by creating an equivalent sample where the candidate with the highest p_{T} is selected instead. Deviations from the default fit are included in the systematic uncertainties of the measurement.

- **Background angles model:** The shape of the background angular distribution, $P_{\mathrm{b}}(\theta_T, \varphi_T, \psi_T)$, is described by the fourteenth-order Legendre polynomial functions, given in equation 8.9. Alternatively, higher-order Legendre polynomial functions were tested, and the changes in the fit parameter values relative to the default fit are taken as systematic uncertainties.

  The shapes are primarily determined by detector and kinematic acceptance effects and are sensitive to the p_{T} of the B_s^0 meson candidate. For this reason, the parameterization using the Legendre polynomial functions is performed in six p_{T} intervals: 10–15 GeV, 15–20 GeV, 20–25 GeV, 25–30 GeV, 30–35 GeV and > 35 GeV.

  The systematic uncertainties due to the choice of p_{T} intervals are estimated by repeating the fit, with these intervals enlarged and reduced by 1 GeV and by 2 GeV. The largest changes in the fit results are taken to represent the systematic uncertainties.

  The parameters of the Legendre polynomial functions given in equation 8.9 are adjusted to give the best fit to the angular distributions for events in the B_s^0 mass sidebands. To test the sensitivity of the fit results to the choice of sideband regions, the fit is repeated with alternative choices for the excluded signal mass regions: $|(m(B_s^0) - 5.366| > 0.085\,\mathrm{GeV}$ and $|(m(B_s^0) - 5.366| > 0.160\,\mathrm{GeV}$ (instead of the default $|(m(B_s^0) - 5.366| > 0.110\,\mathrm{GeV}$). The changes in the fit results are assigned as systematic uncertainties.

- $\boldsymbol{B_d}$ **contribution:** The contamination from $B_d \rightarrow J/\psi\ K^{0*}$ events misreconstructed as $B_s^0 \rightarrow J/\psi\phi$ is accounted for in the final fit. Studies were performed to

evaluate the effect of the uncertainties in the $B_d \to J/\psi K^{0*}$ fraction and the shapes of distributions of mass, transversity angles and lifetime. In the MC events, the angular distribution of the $B_d \to J/\psi K^{0*}$ decay is modeled using parameters taken from Ref. [85]. The contribution of the S-wave $B_d \to J/\psi K\pi$ decays as well as its interference with the P-wave $B_d \to J/\psi K^{0*}$ decays is also included in the PDF of the fit, following the parameters measured in Ref. [85]. The uncertainties of these parameters are taken into account in the estimation of the systematic uncertainty. After applying the B_s^0 signal selection cuts, the angular distributions are fitted using Legendre polynomial functions. The uncertainties of this fit are included in the systematic uncertainty.

- **Λ_b contribution:** The contamination from $\Lambda_b \to J/\psi p K^-$ events misreconstructed as $B_s^0 \to J/\psi\phi$ is accounted for in the final fit. Studies are performed to evaluate the effect of the uncertainties in the $\Lambda_b \to J/\psi p K^-$ fraction f_{Λ_b}, and the shapes of the distributions of the mass, transversity angles and lifetime. Additional studies are performed to determine the effect of the uncertainties in the $\Lambda_b \to J/\psi\Lambda^*$ branching ratios used to reweight the generated MC sample.

- **Fit model mass and lifetime:** To estimate the systematic uncertainties due to the signal B_s^0 mass model, the default model was altered by adding a second Gaussian function to the equation 8.7, which has the same structure as the first Gaussian function but a different scale factor, S_m^1, which is an additional free parameter of the fit. The resulting changes to other fit parameter values are found to be negligible.

  To test the sensitivity of the part of the fit model describing the lifetime, two systematic tests are performed. Determination of signal and background lifetime errors is sensitive to the choice of p_{T} bins, in which the relative contributions of these two components are evaluated. To estimate the systematic uncertainty, the fit is repeated for various intervals of the default p_{T} binning. The determination of signal and background lifetime errors is also sensitive to the determination of the signal fraction. The fit is repeated by varying this fraction within one standard deviation of its uncertainty and differences are included in the systematic uncertainty.

- **Fit model S-wave phase**: As explained in section 8.3.3, the model for the interference between the $B_s^0 \to J/\psi\phi(K^+K^-)$ and the S-wave $B_s^0 \to J/\psi\, K^+K^-$ is corrected by a factor $\alpha = 0.51 \pm 0.02$ to account for the mass-dependent differences in absolute amplitude and phase between the resonant and S-wave amplitudes. To account for the uncertainty in α, the fit was repeated with $\alpha = 0.51 + 0.02$ and $\alpha = 0.51 - 0.02$ values. The variations of the parameter values relative to those

from the default fit using the central value $\alpha = 0.51$ are included in the systematic uncertainties.

- **Fit bias:** Due to its complexity, the fit model can be sensitive to some nuisance parameters. This limited sensitivity could potentially lead to bias in the measured physics parameters, even when the model describes the fitted data well. To test the stability of the results obtained from the chosen default fit model, a set of pseudo-experiments is conducted using the default model for both generation and fit. The systematic uncertainties are determined from the mean of the pull distributions of the pseudo-experiments scaled by the statistical uncertainty of that parameter in the fit to data. Pull distributions of these variations are shown in Figure 8.22. The observed deviations are included in the systematic uncertainties.

The systematic uncertainties are listed in Table 8.3. For each parameter, the total systematic uncertainty is obtained by adding all of the contributions in quadrature.

	ϕ_s [mrad]	$\Delta\Gamma_s$ [ns^{-1}]	Γ_s [ns^{-1}]	$\lvert A_\parallel(0)\rvert^2$ [10^{-3}]	$\lvert A_0(0)\rvert^2$ [10^{-3}]	$\lvert A_S(0)\rvert^2$ [10^{-3}]	$\delta_\perp$ [mrad]	$\delta_\parallel$ [mrad]	$\delta_\perp - \delta_S$ [mrad]
Tagging	19	0.4	0.3	0.2	0.2	1.1	17	19	2.3
Acceptance	0.5	< 0.1	< 0.1	1.0	0.8	2.6	30	50	11
ID alignment	0.8	0.2	0.5	< 0.1	< 0.1	< 0.1	11	7.2	< 0.1
Best candidate selection	0.5	0.4	0.7	0.5	0.2	0.2	12	17	7.5
Background angles model:									
Choice of fit function	2.5	< 0.1	0.3	1.1	< 0.1	0.6	12	0.9	1.1
Choice of p_{T} bins	1.3	0.5	< 0.1	0.4	0.5	1.2	1.5	7.2	1.0
Choice of mass interval	0.4	0.1	0.1	0.3	0.3	1.3	4.4	7.4	2.3
Dedicated backgrounds:									
B_d	2.3	1.1	< 0.1	0.2	3.0	1.5	10	23	2.1
Λ_b	1.6	0.3	0.2	0.5	1.2	1.8	14	30	0.8
Fit model:									
Time res. sig frac	1.4	1.1	0.5	0.5	0.6	0.8	12	30	0.4
Time res. p_{T} bins	0.7	0.5	0.8	0.1	0.1	0.1	2.2	14	0.7
S-wave phase	0.2	< 0.1	< 0.1	0.3	< 0.1	0.3	11	21	8.4
Fit bias	4.1	1.7	0.9	1.4	< 0.1	1.5	19	0.9	7.0
Total	20	2.5	1.6	2.3	3.5	4.5	50	79	18

Table 8.3: Summary of systematic uncertainties assigned to the physical parameters of interest.

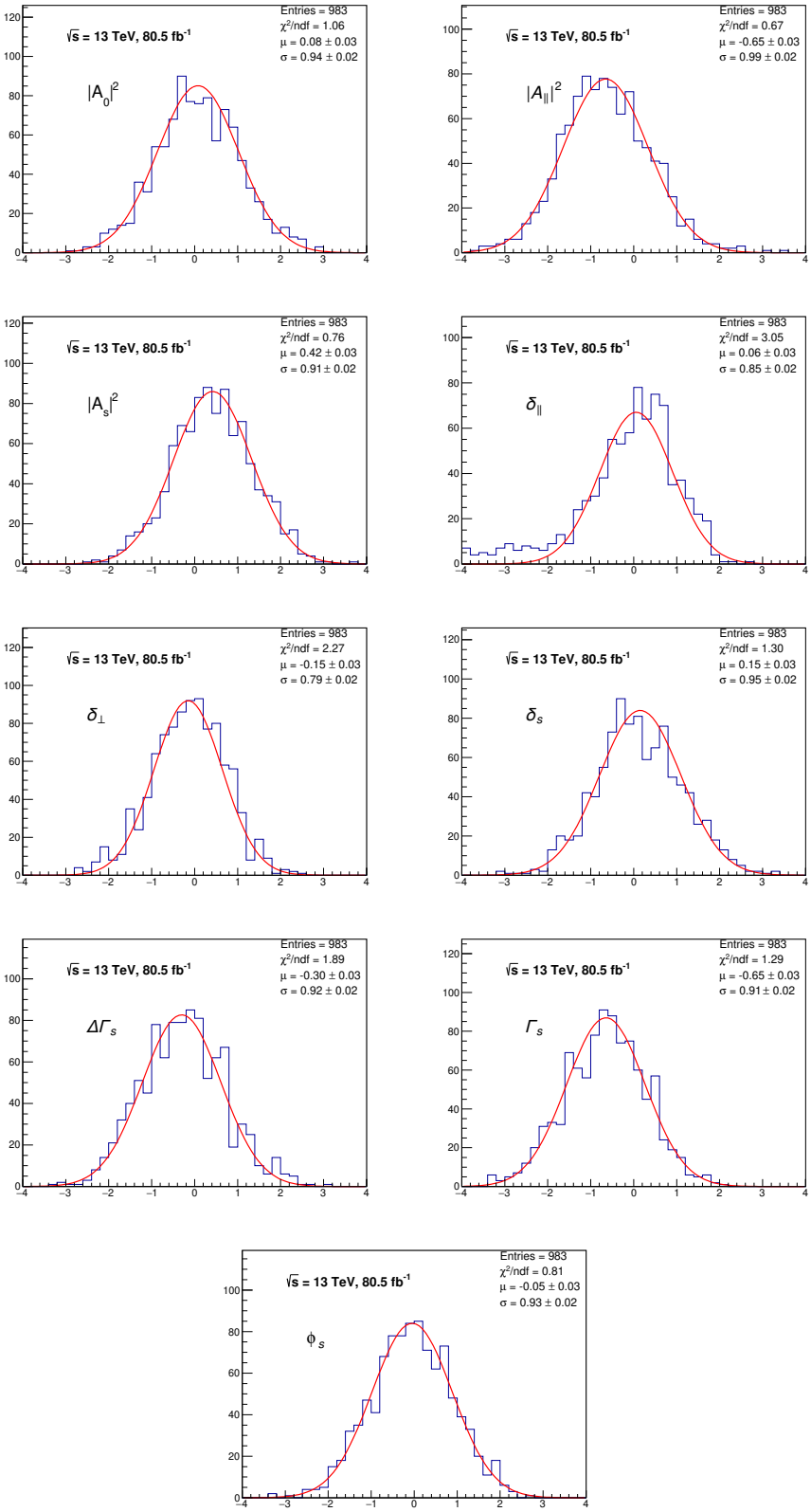

Figure 8.22: Systematic uncertainty of the default fit model evaluated by repeatedly generating pseudo-experiments, fitted by the default model. Pull distributions show variations of the fit results.

8.6 Results

The simultaneous unbinned maximum-likelihood fit to $B_s^0 \to J/\psi(\mu^+\mu^-)\phi(K^+K^-)$ contains nine physical parameters: $\Delta\Gamma_s$, ϕ_s, Γ_s, $|A_0(0)|^2$, $|A_{||}(0)|^2$, $\delta_{||}$, $\delta_\perp$, $|A_S(0)|^2$ and δ_S. The fitted values with statistical and systematic uncertainties are given in Table 8.4, while the correlations of the physics parameters obtained from the fit are given in Table 8.5. Multiplying the total number of events supplied to the fit with the extracted signal fraction and its statistical uncertainty provides an estimate for the total number of B_s^0 meson candidates of 453570 ± 740.

Parameter	Value	Statistical uncertainty	Systematic uncertainty
ϕ_s[rad]	-0.081	0.041	0.020
$\Delta\Gamma_s$[ps^{-1}]	0.0607	0.0046	0.0025
Γ_s[ps^{-1}]	0.6687	0.0015	0.0017
$\lvert A_{\|\|}(0)\rvert^2$	0.2213	0.0020	0.0022
$\lvert A_0(0)\rvert^2$	0.5131	0.0013	0.0034
$\lvert A_S(0)\rvert^2$	0.0321	0.0034	0.0044
$\delta_\perp$ [rad]	3.12	0.11	0.05
$\delta_{\|\|}$ [rad]	3.35	0.05	0.06
$\delta_\perp - \delta_S$ [rad]	-0.25	0.05	0.01

Table 8.4: Values extracted from the fit for the physical parameters of interest with their statistical and systematic uncertainties.

	$\Delta\Gamma$	Γ_s	$\lvert A_{\|\|}(0)\rvert^2$	$\lvert A_0(0)\rvert^2$	$\lvert A_S(0)\rvert^2$	$\delta_{\|\|}$	$\delta_\perp$	$\delta_\perp - \delta_S$
ϕ_s	-0.080	0.016	-0.003	-0.004	-0.008	0.007	0.004	-0.007
$\Delta\Gamma$	1	-0.580	0.089	0.094	0.051	0.032	0.005	0.020
Γ_s		1	-0.127	-0.043	0.083	-0.089	-0.024	0.016
$\lvert A_{\|\|}(0)\rvert^2$			1	-0.341	-0.187	0.541	0.144	-0.056
$\lvert A_0(0)\rvert^2$				1	0.278	-0.108	-0.037	0.071
$\lvert A_S(0)\rvert^2$					1	-0.378	-0.126	0.245
$\delta_{\|\|}$						1	0.265	-0.089
$\delta_\perp$							1	-0.001

Table 8.5: Fit correlations between the physical parameters of interest.

Fit projections of the mass, proper decay time and angles are given in Figures 8.23 and 8.24, respectively. Due the complexness of the likelihood function, the projections are based on the pseudo-experiment generation, also called ToyMC. The ToyMC generation method is based on random number generation according to the probability density func-

tion with parameters fixed to the values given by the unbinned maximum likelihood fit. To generate distributions according to given probability density functions, the accept-reject method is commonly used. Since the $B_d^0 \to J/\psi K^{*0}$ and $\Lambda_b \to J/\psi p K^-$ contributions are small, the mass plot contributions corresponding to this backgrounds are scaled by a factor of 10. Below each figure is a ratio plot that shows the difference between each data point and the total fit line divided by the statistical and systematic uncertainties summed in quadrature (σ) of that point.

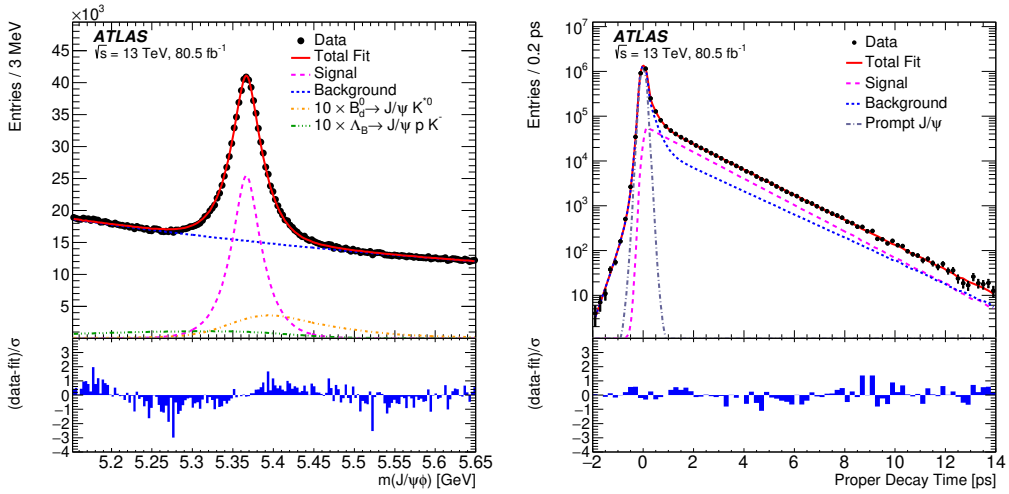

Figure 8.23: (Left) Mass fit projection for the $B_s^0 \to J/\psi\phi$ sample. The red line shows the total fit, the short-dashed magenta line shows the $B_s^0 \to J/\psi\phi$ signal component, the combinatorial background is shown as a blue dotted line, the orange dash-dotted line shows the $B_d \to J/\psi K^{0*}$ component, and the green dash-dot-dot line shows the contribution from $\Lambda_b \to J/\psi p K^-$ events. (Right) Proper decay time fit projection for the $B_s^0 \to J/\psi\phi$ sample. The red line shows the total fit while the short-dashed magenta line shows the total signal. The total background is shown as a blue dotted line, and a long-dashed grey line shows the prompt J/ψ background component.

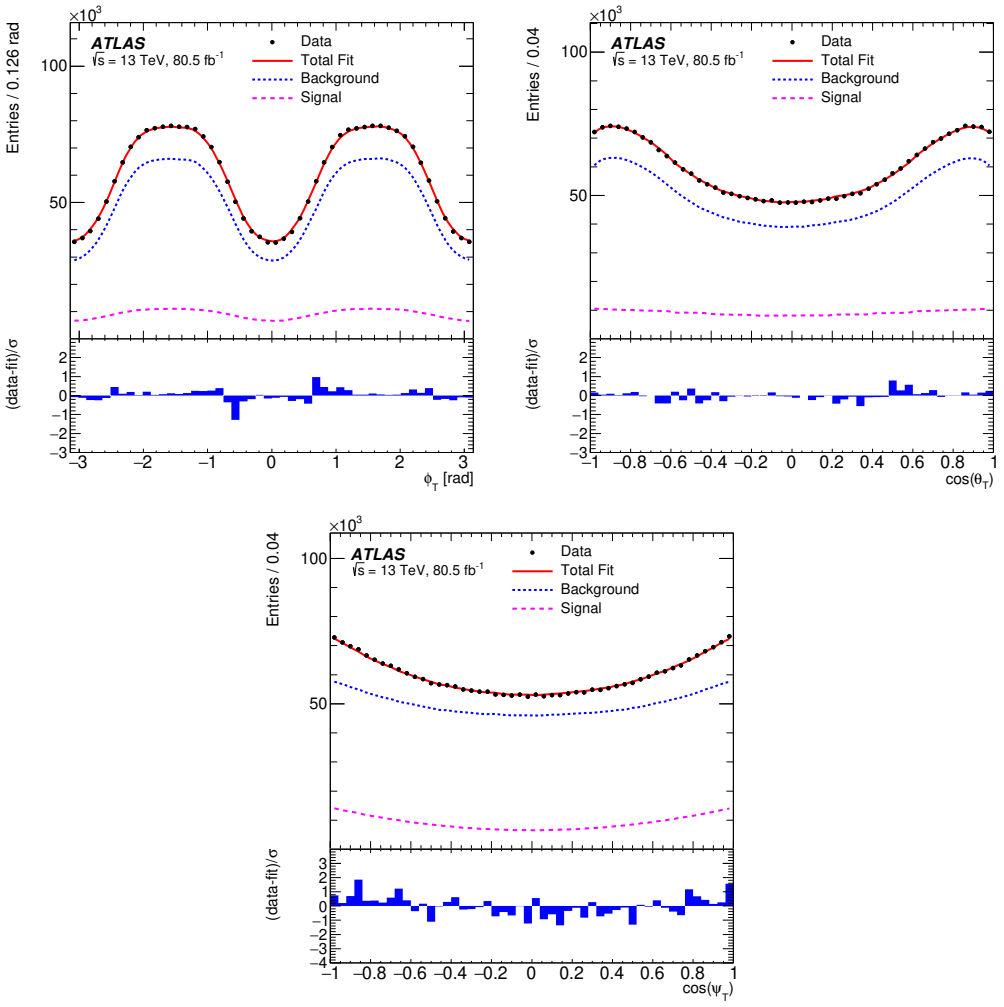

Figure 8.24: Fit projections for the transversity angles ϕ_T (top left), $\cos(\theta_T)$ (top right), and $\cos(\psi_T)$ (bottom). In all three plots the red solid line shows the total fit, the $B_s^0 \to J/\psi\phi$ signal component is shown by the magenta dashed line and the blue dotted line shows the contribution of all background components.

To test the stability of the Likelihood function, 1D profile log-likelihood scans were performed on the physics parameters of interest. The 1D profile log-likelihood scan is performing the maximum likelihood fit, where one of the parameters of interest is fixed and varied in the range of several sigmas around the central value given by the default fit. The rest of the parameters are free in the test. The 1D scans of the nine parameters of interest can be seen in Figure 8.25. This test is performed to confirm the statistical error calculated by the MINUIT minimizer and to verify that the fit converged to the global minimum, in case that the double minimum occurs. As can be seen in Figure 8.25, all parameters except $\delta_{\|}$ have symmetrical error with single minimum. In the 1D scan of $\delta_{\|}$,

double minimum symmetrical around π can be found. The secondary minimum identified at $\delta_{\parallel} = 2.936$ is more shallow than the primary minimum which is at $\delta_{\parallel} = 3.356$. The impact on fit parameters converging to the secondary minimum was studied. The only variable affected is $\delta_{\perp}$ converging to the value of $\delta_{\perp} = 2.906$. The rest of parameters are consistent within statistical uncertainty. For the purpose of this thesis, the global minimum was selected as a default fit value; however, this symmetry is still a matter of discussion in the paper submitted to the journal.

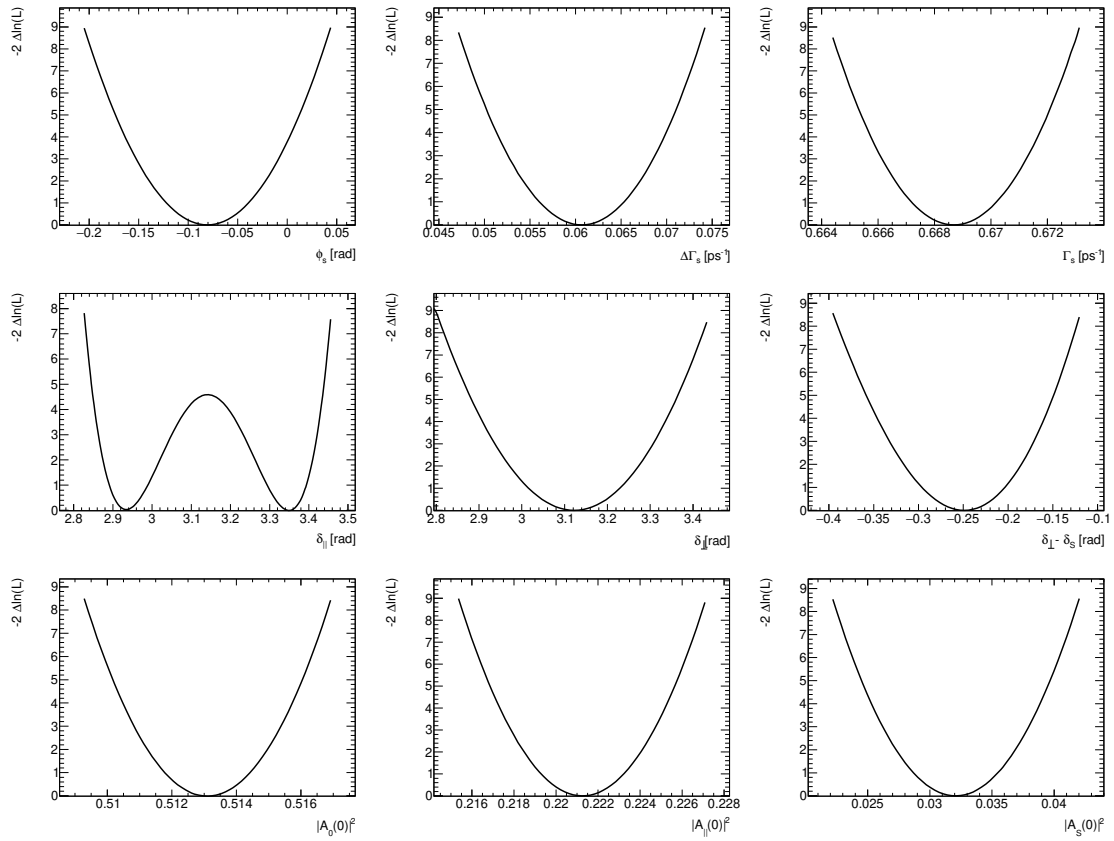

Figure 8.25: The 1D profile likelihood scan for the parameters of interest.

8.7 Combination with ATLAS Run 1 Results

Since the ATLAS measured the CP-violation parameters in Run 1 [91] using $19.2\,\text{fb}^{-1}$ of data collected at $\sqrt{s} = 7\,\text{TeV}$ and $8\,\text{TeV}$, which are consistent with those obtained from this analysis, the statistical combination of these three measurements can be performed. In order to combine the current measurements with those from the previous analysis, the best linear unbiased estimator (BLUE) [92, 93] is used. The BLUE combination

uses the measured values, uncertainties and correlations between parameters for each measurement separately.

Since the collected events through years are different each other, the statistical correlation between these three measurements is set to zero. Because most systematic effects in these three measurements are common, correlations of the systematic uncertainties were estimated. The correlations between systematic effects were categorized in several groups depending of whether the given systematic effect changed significantly between the measurements. The combined results for the fit parameters and their uncertainties are given in Table 8.6.

Parameter	Value	Statistical uncertainty	Systematic uncertainty
ϕ_s [rad]	-0.087	0.037	0.019
$\Delta\Gamma_s$ [ps^{-1}]	0.064	0.004	0.002
Γ_s [ps^{-1}]	0.670	0.001	0.002
$\lvert A_\parallel(0)\rvert^2$	0.222	0.002	0.002
$\lvert A_0(0)\rvert^2$	0.515	0.001	0.003
$\lvert A_S\rvert^2$	0.034	0.003	0.004
$\delta_\perp$ [rad]	3.213	0.102	0.049
$\delta_\parallel$ [rad]	3.356	0.050	0.079
$\delta_\perp - \delta_S$ [rad]	-0.244	0.046	0.018

Table 8.6: Values of the physical parameters extracted from the combination of 13 TeV results with those obtained from 7 TeV and 8 TeV data.

.

The two-dimensional likelihood contours in the ϕ_s–$\Delta\Gamma_s$ plane for the ATLAS results based on the 7 TeV and 8 TeV data, the result from the 13 TeV data, and the combined result are shown in Figure 8.26. The statistical and systematic uncertainties are combined in quadrature and correlations are taken into account in the construction of Gaussian contours. Two-dimensional likelihood contours in the ϕ_s–$\Delta\Gamma_s$ plane are shown in Figure 8.27 for this ATLAS result, the result from CMS [34] using the $B_s^0 \to J/\psi\phi$ decay, and the result from LHCb [36] using the $B_s^0 \to J/\psi K^+K^-$ decay. The contours are obtained by interpreting each result as a two-dimensional Gaussian probability distribution in the ϕ_s–$\Delta\Gamma_s$ plane. All results are consistent with each other and with the SM [94, 95].

8.8 Outlook for Full Run 2 Measurement

Since the LHC Run 2 already finished, the additional data from pp collisions at $\sqrt{s}$ = 13 TeV with integrated luminosity of 58.5 fb^{-1} collected in year 2018 can be included

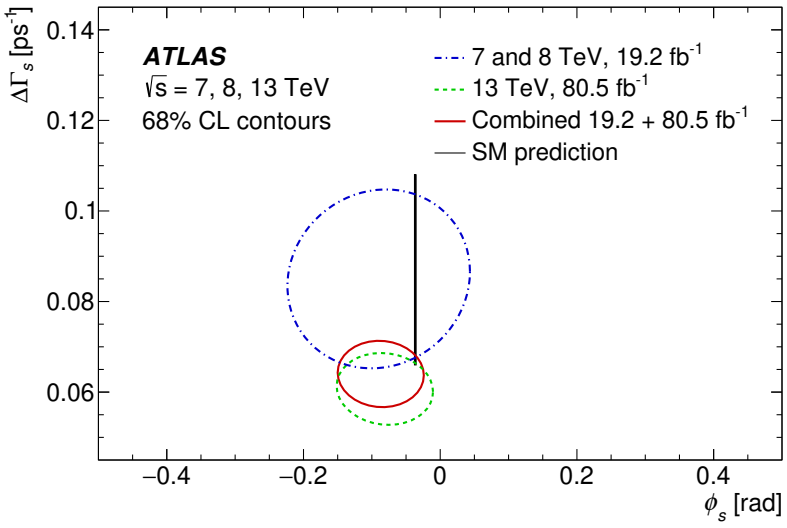

Figure 8.26: Contours of the 68% confidence level in the ϕ_s–$\Delta\Gamma_s$ plane, showing ATLAS results for 7 TeV and 8 TeV data (blue dashed-dotted curve), for 13 TeV data (green dashed curve) and for 13 TeV data combined with 7 TeV and 8 TeV (red solid curve) data. The Standard Model prediction [94, 95] is shown as a very thin black rectangle. In all contours the statistical and systematic uncertainties are combined in quadrature and correlations are taken into account.

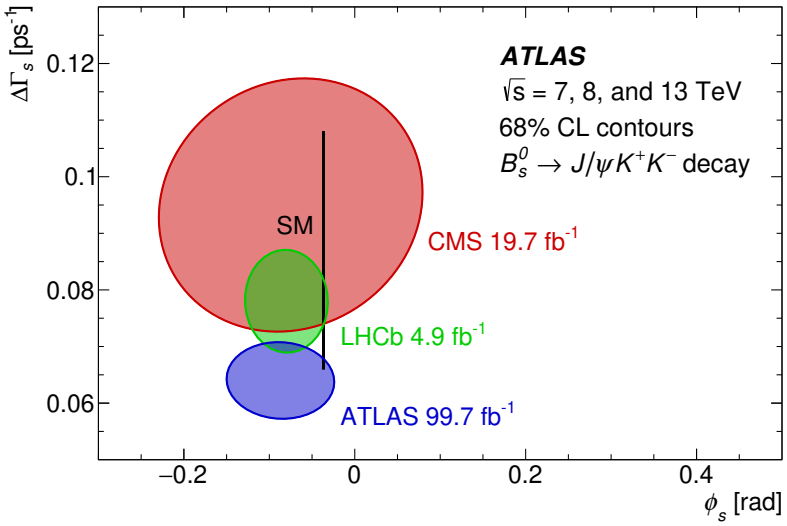

Figure 8.27: Contours of the 68% confidence level in the ϕ_s–$\Delta\Gamma_s$ plane, including results from CMS (red) and LHCb (green) using the $B_s^0 \to J/\psi K^+K^-$ decay only. The blue contour shows the ATLAS result for 13 TeV combined with 7 TeV and 8 TeV data. The Standard Model prediction [94, 95] is shown as a very thin black rectangle. In all contours the statistical and systematic uncertainties are combined in quadrature.

in the measurement. Because previous measurement already revealed some difficulties with data modeling connected to the large statistics of collected B_s^0 sample, the updated model will be applied to the full Run 2 dataset. However, at first step of the analysis, the combined dataset of 2015-2018 data with integrated luminosity of 139 fb^{-1} is fitted by the current data model. Already at this stage, this analysis can benefit from the increased statistics and provide better precision on the ϕ_s measurement. In addition, the Δm_s can be released in the fit as a free parameter and provide the first measurement of B_s^0 oscillation frequency at the ATLAS experiment.

There is one additional update to the fit model. All previous measurements at the ATLAS assumed that there is no direct CP-violation in the B_s^0 mixing, which is expected by the theory. If there is no direct CP-violation, the absolute value of parameter lambda given by equation 2.5 is $|\lambda| = 1$. The fit model for a full Run 2 measurement was adjusted to include this parameter $|\lambda|$ to confirm the predictions and in order to properly combine all LHC experimental results.

The preliminary fit results on the full Run 2 dataset are consistent with those obtained in the previous analysis and are presented in Table 8.7. As can be seen from the results, the $|\lambda|$ is compatible with unity.

Parameter	Value	Statistical uncertainty	Systematic uncertainty
ϕ_s [rad]	-0.066	0.029	0.018
$\Delta\Gamma_s$ [ps^{-1}]	0.0619	0.0034	0.0023
Γ_s [ps^{-1}]	0.6696	0.0011	0.0012
Δm_s [ps^{-1}]	17.879	0.059	0.056
$\lvert\lambda\rvert$	0.995	0.011	0.004
$\lvert A_\parallel(0)\rvert^2$	0.2248	0.0015	0.0016
$\lvert A_0(0)\rvert^2$	0.5078	0.0010	0.0016
$\lvert A_S(0)\rvert^2$	0.0226	0.0025	0.0038
$\delta_\perp$ [rad]	3.23	0.12	0.11
$\delta_\parallel$ [rad]	3.37	0.03	0.04
$\delta_\perp - \delta_S$ [rad]	-0.29	0.04	0.03

Table 8.7: Fitted values for the physical parameters of interest with their statistical and systematic uncertainties.

The comparison of the first measurement of Δm_s parameter with other experiments is shown in Figure 8.28. The two-dimensional likelihood contours in the $\phi_s - \Delta\Gamma_s$ plane comparing ATLAS full Run 2 preliminary results, previous ATLAS measurements based on 2015-2017 data, CMS result [96], and the results from LHCb [36] is shown in Figure 8.29.

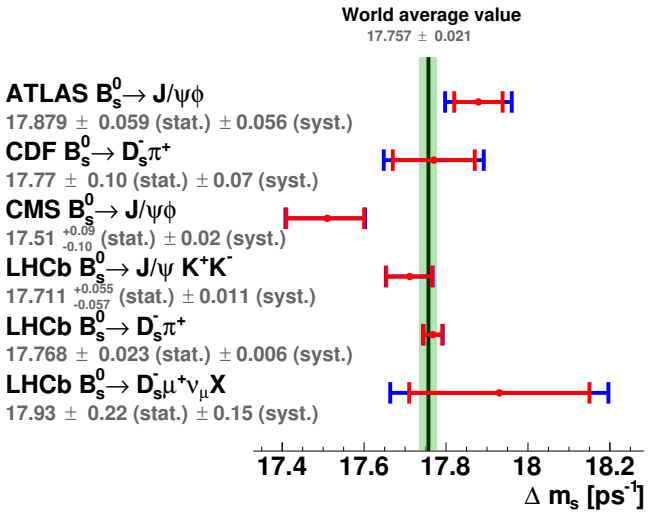

Figure 8.28: Comparison of ATLAS Run 2 results with LHCb [97, 98], CDF [99] results and the world average value (PDG value) [4]. Red are statistical errors and blue are sum of statistical and systematic uncertainties. The green area is the uncertainty of the world average value.

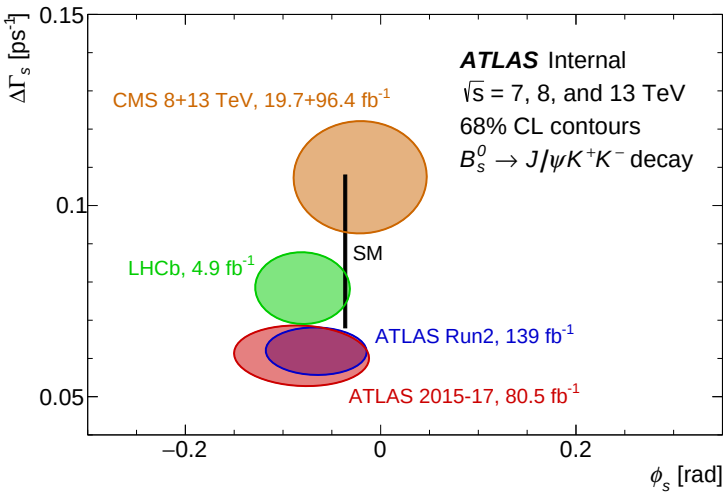

Figure 8.29: Contours of the 68% confidence level in the ϕ_s–$\Delta\Gamma_s$ plane showing current ATLAS result (blue), the previous ATLAS result [100] (red), the CMS result [96] (orange), and LHCb results [36] (green and purple). The Standard Model prediction [94, 30] is shown as a very thin black rectangle. In all contours, the statistical and systematic uncertainties are combined in a quadrature.

CHAPTER 9

$B^{\pm}$ and B_d^0 Lifetime Measurement

Since the CP-violation in $B_s^0 \to J/\psi(\mu^+\mu^-)\phi(K^+K^-)$ relies on the precise vertexing and efficient lifetime estimation, the measurement from the reference channel would provide a useful information about the recorded data sample. For this purpose, two reference channels were selected, the $B^{\pm} \to J/\psi K^{\pm}$ and the $B_d^0 \to J/\psi K^{*0}(K\pi)$.

The knowledge of fundamental properties of $B^{\pm} \to J/\psi K^{\pm}$ decay is very important not only as a supporting measurement for the CP-violation measurement, but, due to its high branching ratio, it also serves as a control channel for the lifetime efficiency estimation and trigger rate for all B-Physics measurements.

However, the $B^{\pm}$ mass spectra contain a significant contribution from the $J/\psi + X$ decays, which complicates the precise lifetime estimation. For this reason, the second reference channel $B_d^0 \to J/\psi K^{*0}(K\pi)$ was selected. The $B_d^0 \to J/\psi K^{*0}(K\pi)$ branching ratio is not as large as for the $B^{\pm} \to J/\psi K^{\pm}$ decay; however, it still provides a sufficient statistical sample for the lifetime measurement.

This chapter will provide the detailed description of the lifetime measurement.

9.1 Data Samples, Reconstruction and Candidate Selection

This measurement uses several data samples: $3.2\,\text{fb}^{-1}$ of 13 TeV data from pp collisions taken in 2015, $32.5\,\text{fb}^{-1}$ of 13 TeV data from pp collisions taken in 2016 and $46.9\,\text{fb}^{-1}$ of 13 TeV data from pp collisions taken in 2017. There are also several MC simulations used for support studies.

In order to reconstruct the $B^{\pm}$ and B_d^0, a J/ψ candidate is first constructed by refitting a pair of oppositely charged muon candidates with $p_{\text{T}} > 4\,\text{GeV}$ to a common vertex, where the quality of the fit meets the requirement $\chi^2/\text{d.o.f.} < 10$. The muons are identified

using information from both the MS and the ID. The invariant mass of the muon pair is calculated from the refitted track parameters, and pairs with a mass in the range of $2.6 - 3.6\,\text{GeV}$ are accepted for further analysis.

9.1.1 $B^{\pm}$ Candidate Reconstruction

The $B^{\pm}$ candidates are formed by adding another track (a kaon candidate) with $p_{\text{T}} > 1.5\,\text{GeV}$ and absolute rapidity $|y| < 2.5$. This track must not be identified as a muon. Candidates for $B^{\pm} \to J/\psi K^{\pm}$ decays are selected by fitting the tracks from each $J/\psi \to \mu^+\mu^-$ candidate in the event with each kaon candidate to a common vertex. Each of the three tracks is required to have at least one hit in the pixel detector and at least four hits in the silicon microstrip detector. The fit is further constrained by fixing the invariant mass calculated from the two muon tracks to the world average J/ψ mass. No constraint for the $B^{\pm}$ momentum to point from the secondary to a primary vertex is applied in the fit. A triplet of tracks is accepted for further analysis if the vertex fit has a $\chi^2/\text{d.o.f.} < 3$. If there is more than one accepted candidate in the event, the candidate with the lowest $\chi^2/\text{d.o.f.}$ is selected. The final candidate must fit within a mass range of $4.95 - 5.80\,\text{GeV}$.

9.1.2 B^0_d Candidate Reconstruction

The B^0_d candidates are formed by combining two additional tracks with the J/ψ candidate to form a common vertex, under B^0_d and $\overline{B^0_d}$ hypothesis. The two additional tracks must originate from the absolute rapidity range of $|y| < 2.5$. The transverse momentum of $K^{\pm}$ track is required to be greater than $1\,\text{GeV}$, while the $\pi^{\pm}$ track transverse momentum threshold is set to $500\,\text{MeV}$. Both tracks must not have been identified as a muon. Each of the four tracks is required to have at least one hit in the pixel detector and at least four hits in the silicon microstrip detector. The fit is further constrained by fixing the invariant mass calculated from the two muon tracks to the world average J/ψ mass. No constraint for the B^0_d momentum to point from the secondary to a primary vertex is applied in the fit. A quadruplet of tracks is accepted for further analysis if the vertex fit has a $\chi^2/\text{d.o.f.} < 2.5$. If there is more than one accepted candidate in the event, the candidate with the lowest $\chi^2/\text{d.o.f.}$ is selected. The final candidate must fit within a mass range of $5.00 - 5.55\,\text{GeV}$.

9.2 Fitting Procedure

To extract mass and lifetime of the candidates, several steps are needed. At first, an unbinned maximum-likelihood fit is performed on the selected events in the B mass region to extract the fractions of signal and background contributions. The evaluated fractions

are used to produce the lifetime error distributions for each of the signal and background component. Using these lifetime error distributions, the simultaneous unbinned maximum-likelihood fit is performed in the B mass-lifetime region using the information from lifetime error distributions as conditional variables.

9.2.1 Mass Distribution

$B^{\pm}$ Mass Distribution

The likelihood function, $\mathcal{L}$, is defined as a combination of the signal and background probability density functions as follows:

$$\ln \mathcal{L} = \sum_{i=1}^{N} \ln(f_s \cdot ((1 - f_{B_\pi}) \cdot \mathcal{F}_s(m_i) + f_{B_\pi} \cdot \mathcal{F}_{B_\pi}(m_i)) + f_{B_x} \cdot \mathcal{F}_{B_x}(m_i) + (1 - f_{B_x} - f_s) \cdot \mathcal{F}_{bkg}(m_i)), \tag{9.1}$$

where N is the number of selected candidates, f_s is the fraction of signal candidates, f_{B_x} is the fraction of partially reconstructed B-hadrons and f_{B_π} is the fraction of $B^{\pm} \to J/\psi\pi^{\pm}$ decays mis-identified as $B^{\pm} \to J/\psi K^{\pm}$ candidates, calculated relative to the number of signal events. The fraction f_{B_π} is fixed to a value derived from MC simulations and accounts for the measured branching fraction. The mass m_i is measured from the data for each event i. $\mathcal{F}_s$, $\mathcal{F}_{B_x}$, $\mathcal{F}_{B_\pi}$ and $\mathcal{F}_{bkg}$ are the probability density functions (PDF) modeling the signal, the specific B_x and $B^{\pm} \to J/\psi\pi^{\pm}$ backgrounds and the remaining combinatorial background. The signal PDF $\mathcal{F}_s$ is modeled as a sum of three Gaussian distributions with a common mean. The $\mathcal{F}_{B_x}$ background is modeled as a hyperbolic tangent function. Combinatorial background is approximated in the fit by an exponential function of mass. The $\mathcal{F}_{B_\pi}$ is modeled by a double-sided CrystalBall function and its parameters are extracted from the MC simulation. The fit to invariant mass distribution of the $B^{\pm}$ candidates can be seen in Figure 9.1.

B_d^0 Mass Distribution

Since the B_d^0 mass distribution does not contain a large amount of the partially reconstructed events and the contamination with mis-reconstructed events is negligible, the mass likelihood function, $\mathcal{L}$, takes simplified form as follows:

$$\ln \mathcal{L} = \sum_{i=1}^{N} \ln(f_s \cdot \mathcal{F}_s(m_i) + (1 - f_s) \cdot \mathcal{F}_{bkg}(m_i)), \tag{9.2}$$

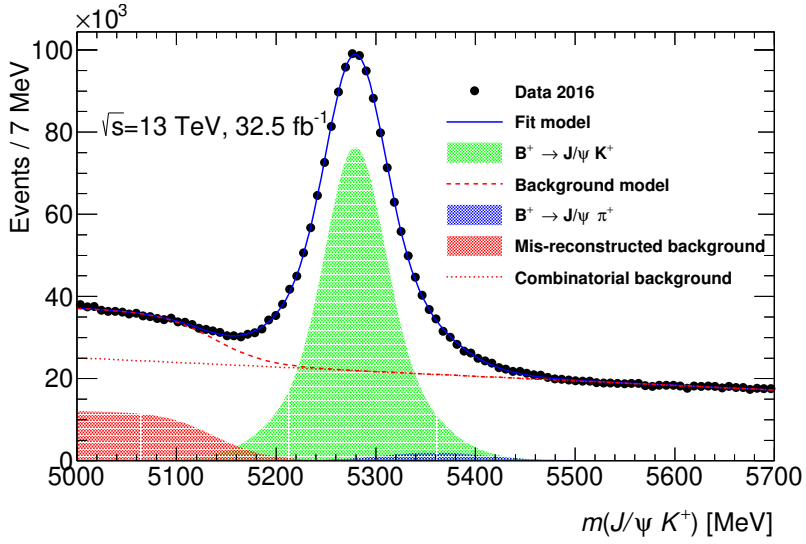

Figure 9.1: Fit of invariant mass spectrum of $B^{\pm}$ candidates for data collected in year 2016. The black dots represent the data, the red dotted line is combinatorial background, the red area is partially reconstructed B-hadrons background, green area is signal distribution and blue line represents the total fit model.

where N is the number of selected candidates and f_s is the fraction of signal candidates described by the PDF $\mathcal{F}_s$, and $\mathcal{F}_{bkg}$ is the background PDF. The mass m_i is measured from the data for each event i. The signal PDF $\mathcal{F}_s$ is modeled as a sum of three Gaussian distributions with a common mean and combinatorial background is approximated in the fit by an exponential function of mass. The fit to invariant mass distribution of the B^0_d candidates can be seen in Figure 9.2.

9.2.2 Time Error Probability Fit

Using the PDF distributions from unbinned maximum-likelihood to fit the invariant mass of B candidates, the fraction of each signal and background component is evaluated for signal and sideband regions, respectively. The fraction estimation is based on the numerical integral method. The time error estimation proceeds in following steps:

- The combinatorial background time error distribution is evaluated from sideband regions. The B^0_d candidates combinatorial background time uncertainty distribution is extracted from both left and right sideband simultaneously, where the sideband regions are defined as follows: $5100\,\text{MeV} < m(B^0_d) < 5150\,\text{MeV}$ and $5450\,\text{MeV} < m(B^0_d) < 5500\,\text{MeV}$. Since the left sideband of $B^{\pm}$ invariant mass distribution contain the contribution from partially reconstructed events, the combinatorial background time uncertainty distribution is extracted from the right sideband only de-

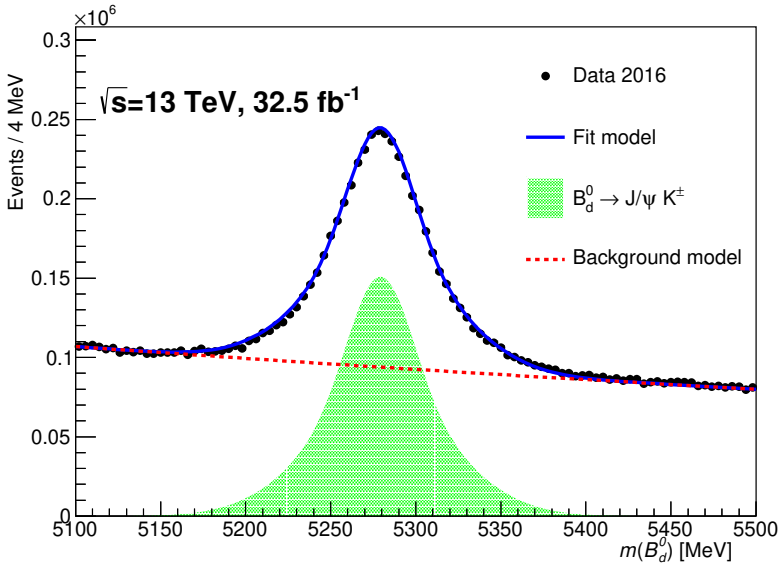

Figure 9.2: Fit of invariant mass spectrum of B_d^0 candidates for data collected in year 2016. The black dots represent the data, red dotted line is combinatorial background, the green area is signal distribution and the blue line represents the total fit model.

fined as $5500\,\text{MeV} < m(B^\pm) < 5700\,\text{MeV}$.

- The time error distribution of partially reconstructed events in $B^\pm$ invariant mass distribution is extracted from the left sideband defined as $5000\,\text{MeV} < m(B^\pm) < 5150\,\text{MeV}$. The fraction and shape of combinatorial background is fixed in this fit.

- Finally, the signal time error distribution is evaluated from the overall invariant mass region, where the fractions and shapes of background components are fixed.

To describe the PDF of each signal and background time error component, the sum of two log-normal distributions is used. In the Figures 9.3 and 9.4, the time error PDF of $B^\pm$ and B_d^0 signal and background components for signal and sideband regions are depicted.

9.2.3 Simultaneous Mass-Lifetime Fit

The final step of the lifetime measurement is to perform unbinned maximum-likelihood fit in the B-hadron mass-lifetime region using the information from lifetime error distributions as conditional variables. The likelihood function, $\mathcal{L}$, of $B^\pm$ candidates is defined as a

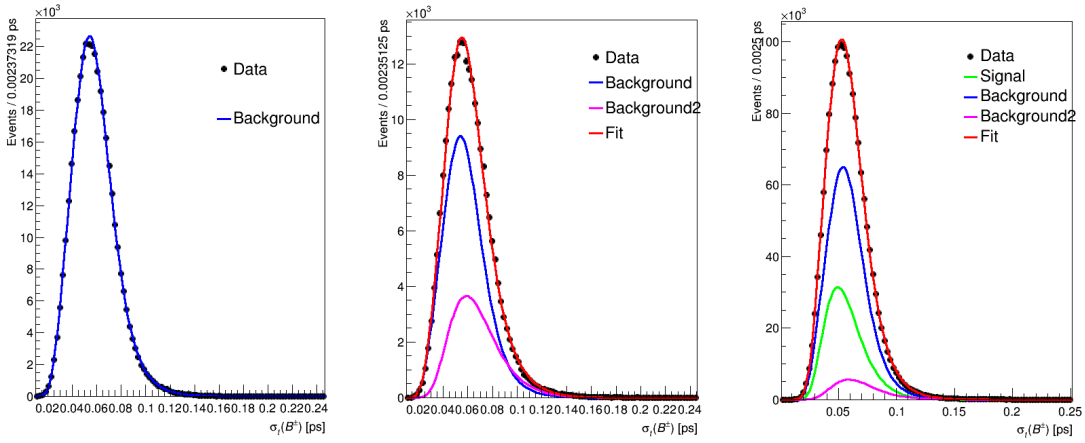

Figure 9.3: The $B^{\pm}$ lifetime error distributions fit in the right mass sideband (left), left sideband (middle) and full lifetime distribution (right). The combinatorial lifetime error distribution is represented by the blue line, partially reconstructed B-hadrons lifetime error distribution by the purple line, signal lifetime error distribution by the green line and the total distribution by the red line.

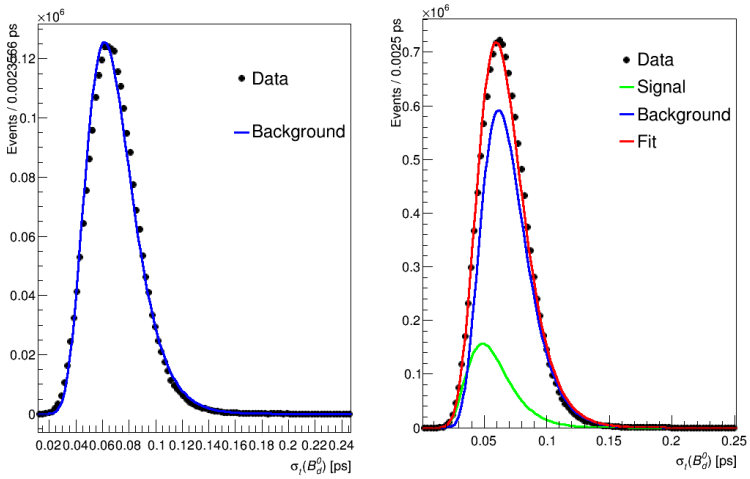

Figure 9.4: The B^0_d lifetime error distributions fit in the mass sideband region (left) and full lifetime distribution (right). The combinatorial lifetime error distribution is represented by the blue line, signal lifetime error distribution by the green line and the total distribution by the red line.

combination of the signal and background probability density functions as follows:

$$\begin{aligned}\ln \mathcal{L} = \sum_{i=1}^{N} w_i \cdot \ln(f_s \cdot (\mathcal{F}_s(m_i) + f_{B_\pi} \cdot \mathcal{F}_{B_\pi}(m_i)) \cdot \mathcal{F}_s(\tau_i|\sigma_{\tau_i}) \cdot \mathcal{F}_s(\sigma_{\tau_i}) + \\ f_{B_x} \cdot \mathcal{F}_{B_x}(m_i) \cdot \mathcal{F}_{B_X}(\tau_i|\sigma_{\tau_i}) \cdot \mathcal{F}_{B_X}(\sigma_{\tau_i}) + \\ (1 - f_s - f_{B_x}) \cdot \mathcal{F}_{bkg}(m_i) \cdot \mathcal{F}_{bkg}(\tau_i|\sigma_{\tau_i}) \cdot \mathcal{F}_{bkg}(\sigma_{\tau_i})),\end{aligned} \tag{9.3}$$

where the distributions for mass probability are discussed in subsection 9.2.1 and the shapes of lifetime error distributions are fixed according to subsection 9.2.2. For description of signal lifetime component $\mathcal{F}_s(\tau_i|\sigma_{\tau_i})$, the exponential convolved with detector resolution function is used. To describe the mis-reconstructed background contribution $\mathcal{F}_{B_X}(\tau_i|\sigma_{\tau_i})$, the single sided exponential convolved with detector resolution function is used as in the previous case. The combinatorial background $\mathcal{F}_{bkg}(\tau_i|\sigma_{\tau_i})$ is described using a sum of two positive exponentials and one negative exponential convolved with detector resolution. These shapes were tested on MC simulations and in data sidebands. The weight w_i accounts for the lifetime correction discussed in 9.2.3. The lifetime distribution extracted from the fit can be seen in Figure 9.5.

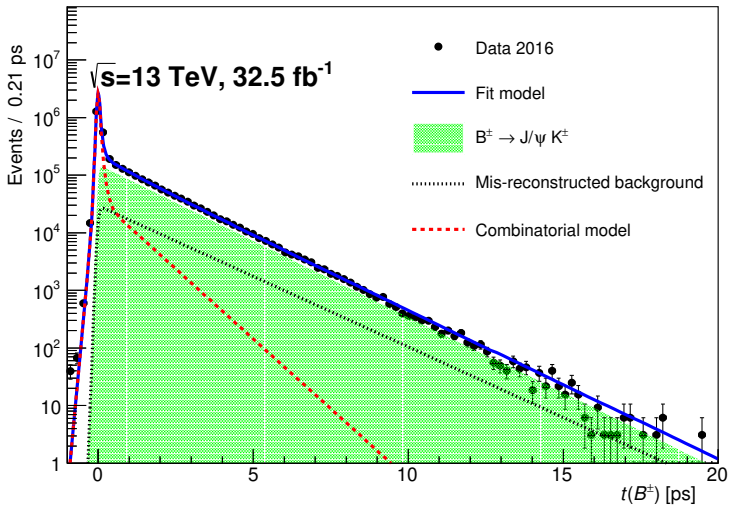

Figure 9.5: The lifetime projection of $B^{\pm}$ events extracted from the simultaneous mass-lifetime fit. The combinatorial background is represented by the red dashed line, partially reconstructed B-hadrons background by the black dotted line, signal component by the green area and total distribution is represented by the blue line.

Because of simpler mass structure of B_d^0 candidates, the likelihood function given in equation 9.3 does not contain the $\mathcal{F}_{B_\pi}$ and $\mathcal{F}_{B_X}$ components. However, the rest of the likelihood function is the same. The lifetime projection of the simultaneous mass-lifetime fit for the B_d^0 candidates is shown in Figure 9.6.

Trigger Lifetime Correction

Due to the trigger inefficiencies at larger lifetime values and other systematic biases, the per-candidate correction w_i was introduced. Lifetime correction was estimated using

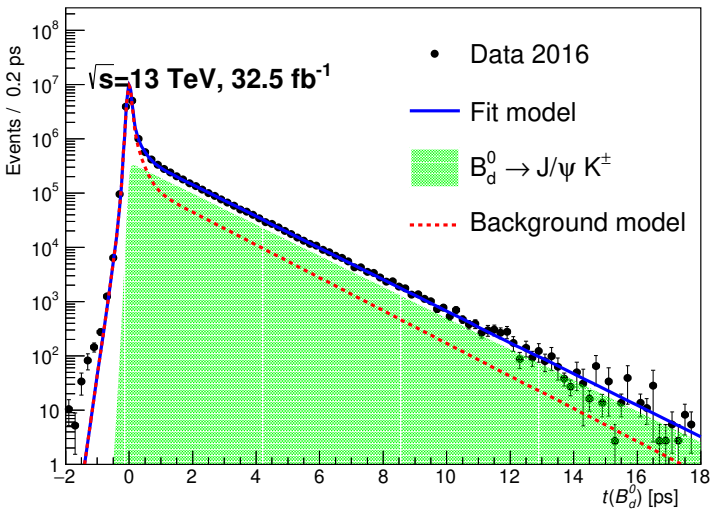

Figure 9.6: The lifetime distribution of B^0_d events extracted from the simultaneous mass-lifetime fit with per candidate lifetime error distributions. The combinatorial background is represented by the red dashed line, signal by the green area and total distribution is the blue line.

MC simulations with the same reconstruction and trigger algorithms as for data events. The distribution of events selected by specific trigger was divided by all generated events. In the ideal case, the distribution is flat; however, in case of any systematic bias it takes the form described in equation 8.11. This lifetime correction is applied in the precise lifetime measurement produced for data collected in longer periods such as years. However, for the lifetime monitoring based on sub-periods data sample, where the data sample statistics is lower, this correction might introduce additional uncertainty. For this reason, the lifetime monitoring fits are made without lifetime correction and only relative comparison between tested triggers and data periods were produced.

9.3 Mass-Lifetime Monitoring

The mass-lifetime monitoring plots were produced directly after data taking at the time when the events were fully reconstructed and recorded to the storage. The monitored properties were invariant mass and lifetime distribution of the $B^{\pm}$ mesons. The plots were produced for selected triggers for each data period separately. Figure 9.7 shows an example of the monitoring plot for the data collected in year 2017 produced for one selected trigger over the data taking periods.

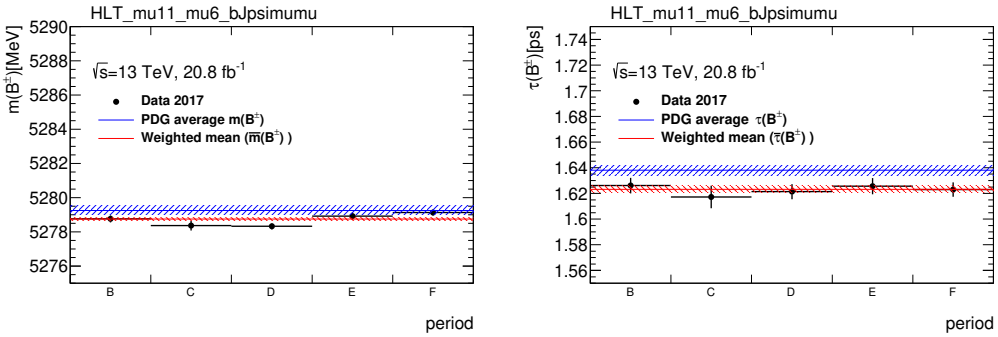

Figure 9.7: The mass (left) and lifetime stability (right) over monitoring periods from data taken in 2017. The blue line is the PDG value of measured quantities and the red line is the weighted average of the measurements.

9.4 Precise Lifetime Measurement

The precise lifetime measurement in both $B^{\pm}$ and B_d^0 channels is required to support CP-violation measurement in the B_s^0 channel. The lifetime measurement was produced using the same trigger selection as the B_s^0 measurement to verify the quality of the collected data. Since this measurement is only supporting measurement to the CP-violation in $B_s^0 \to J/\psi(\mu^+\mu^-)\phi(K^+K^-)$ analysis, the presented results are shown with statistical error only. The proper systematic error evaluation need to be done in the future in case that these results will be published. The lifetime measured in the $B^{\pm}$ channel suffers from higher instability due to additional partially reconstructed component and the systematic effects will be dominant over the statistical error.

The extracted values of $B^{\pm}$ lifetime from datasets organized in years can be seen in Figure 9.8. This encouraging result shows good stability over time and in addition the statistical precision reaches the world average result.

In order to compare results with other experiments, the statistical combination of three partial results were performed. Using simple BLUE method, the combined value of $B^{\pm}$ lifetime is $\tau = (1.639 \pm 0.001)\,\text{ps}$. The extracted result is fully compatible with the LHCb [75] and CDF [101] measurements as can be seen in Figure 9.9.

The measured lifetimes extracted from the $B_d^0 \to J/\psi K^{*0}$ channel are presented in Figure 9.10. There are small differences between the lifetimes; however, the results are still fully compatible with the world average value. The statistical error of the 2017 data sample is higher due to selected trigger strategy. The introduction of topological triggers was optimized for the B_s^0 measurement and gives high rates for B_s^0 and $B^{\pm}$ events; however, the B_d^0 sample suffers from this decision.

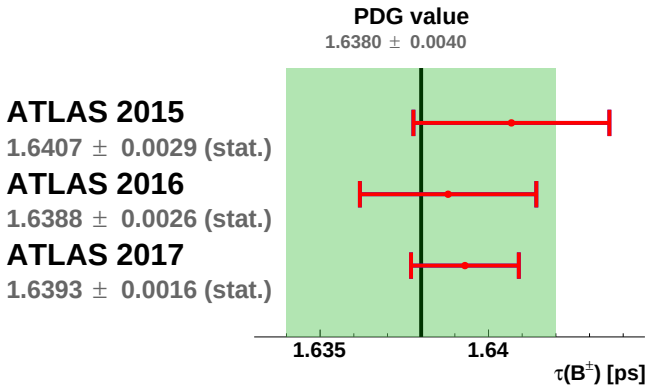

Figure 9.8: Comparison of extracted lifetime from the $B^{\pm} \to J/\psi K^{\pm}$ decay channel for years from 2015 to 2017. The green band represents the uncertainty of the world average value [4].

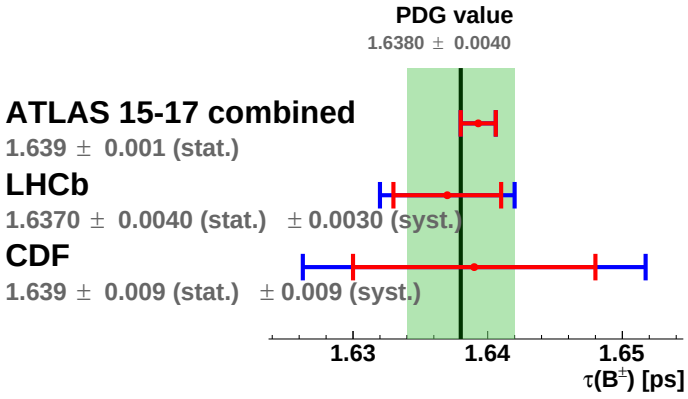

Figure 9.9: Comparison of combined $B^{\pm} \to J/\psi K^{\pm}$ lifetime with LHCb [75] and CDF [101] results. The green band represents the uncertainty of the world average value [4].

The combined fit was performed on the data from all three years in order to compare the B^{0}_{d} lifetime with other experiments. This comparison can be seen in the Figure 9.11, where the other LHC measurements [102, 75, 103] were included together with ATLAS Run 1 result [104]. In this figure can be seen that the results are consistent within statistical precision of this result.

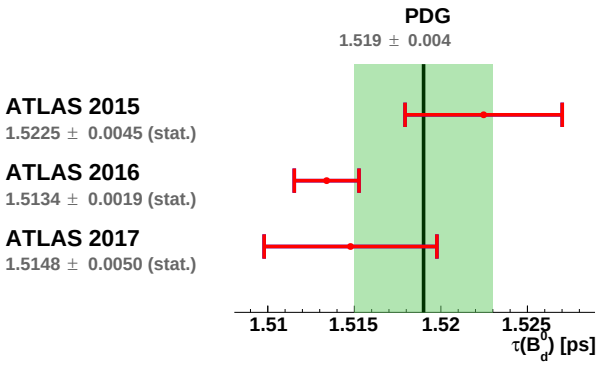

Figure 9.10: Comparison of extracted lifetime from the $B_d^0 \to J/\psi K^{*0}$ decay channel for years 2015 to 2017. The green band represents the uncertainty of the world average value [4].

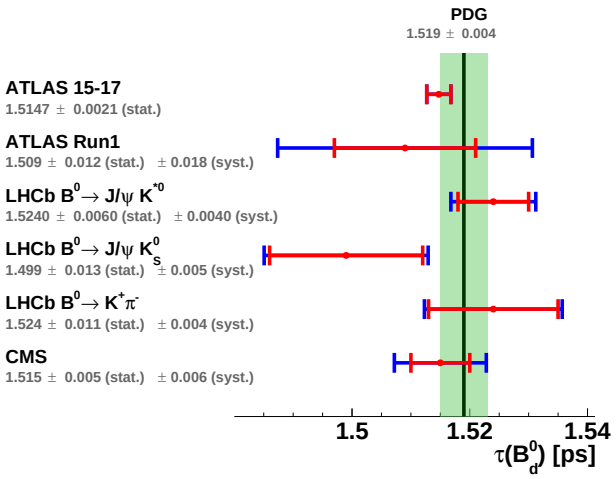

Figure 9.11: The combined $B_d^0 \to J/\psi K^{*0}$ lifetime from 2015 to 2017 data compared with previous ATLAS [104], CMS [102], and LHCb [75, 103] measurements. The green band represents the uncertainty of the world average value [4].

9.5 Summary

The benchmark measurement of $B^\pm \to J/\psi K^\pm$ and $B_d^0 \to J/\psi K^{*0}$ lifetime was performed on the data collected between years 2015 and 2017 of pp collisions at $\sqrt{s} = 13\,\text{TeV}$. The code was originally developed for the lifetime monitoring; however, it was further improved to measure precise lifetime of $B^\pm \to J/\psi K^\pm$ and $B_d^0 \to J/\psi K^{*0}$ events. The preliminary results shows the excellent precision of the ATLAS detector and measured quan-

tities are very close to the PDG values. This results are used to support CP-violation measurement in $B_s^0 \to J/\psi(\mu^+\mu^-)\phi(K^+K^-)$ decay, where the simplistic lifetime approach can not be applied. The effect of the lifetime weights applied to correct minor lifetime inefficiencies was tested and it provides useful feedback for the CP-violation measurement. The preliminary results are presented with statistical error only and the systematic effects on the lifetime value are yet to be evaluated.

CHAPTER 10

Search for a Structure in the $B_s^0\pi^\pm$ Invariant Mass Spectrum

In early 2016, the DØ collaboration [105] announced an evidence of a narrow structure referred to as X(5568), in $B_s^0\pi^\pm$ spectrum in $p\bar{p}$ collisions at $\sqrt{s} = 1.96\,\text{TeV}$ center-of-mass energy, as can be seen in Figure 10.1. The most probable explanation of such as an exotic state would be a hadron composed of four quarks (b, s, u, d). This exotic state would be very important for understanding of the production mechanism of multiquark objects. In the case of the tightly bound di-quark anti-diquark pair, this may provide an additional information about strong interaction potential.

The DØ collaboration reported the signal with $5.1\,\sigma$ significance with invariant mass $\text{m} = 5567.8 \pm 2.9(\text{stat})^{+0.9}_{-1.9}(\text{syst})\,\text{MeV}$ and its width $\Gamma = 21.9 \pm 6.4(\text{stat})^{+5.0}_{-2.5}(\text{syst})\,\text{MeV}$. The ratio ρ_X of the yield of X(5568) to the yield of the B_s^0 meson for a transverse momentum range of $10 < p_\text{T}(B_s^0) < 30\,\text{GeV}$ was measured to be $0.086 \pm 0.019(\text{stat}) \pm 0.014(\text{syst})$.

This result from the DØ collaboration was further investigated by the LHCb [106], CMS [107] and CDF [108] collaborations. As none of these experiments saw any evidence of the reported state X(5568), each published an upper limit on the 95% CL of the relative production rate ρ_X. Recently, the DØ collaboration published further evidence for the X(5568) resonance in the decay sequence $X \to B_s^0\pi^\pm$, $B_s^0 \to \mu^\mp\,\nu\,D_s^\pm$, $D_s^\pm \to \phi\pi^\pm$ [109], which is consistent with their previous measurement.

In parallel to the above mentioned measurements, search for $\text{X}(5568) \to B_s^0\pi^\pm$ was performed with the ATLAS detector [110]. This measurement can serve as benchmark analysis for B-Physics working group which is mainly focusing on the CP-violation in $B_s^0 \to J/\psi(\mu^+\mu^-)\phi(K^+K^-)$. The results of the analysis are presented in more detail in

the following section.

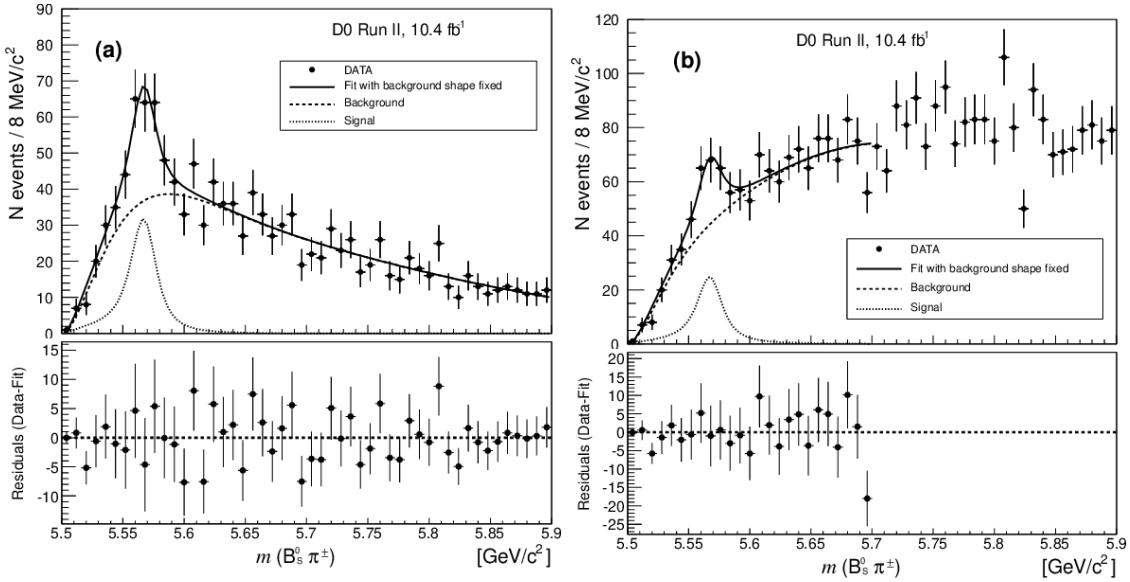

Figure 10.1: The $m(B_s^0\pi^\pm)$ distribution together with the background distribution and the fit results (a) after applying the $\Delta R < 0.3$ cone cut and (b) without the cone cut obtained by DØ experiment [105].

10.1 Data and Candidate Selection

The studies were made on a data sample recorded with the ATLAS detector [2] at Large Hadron Collider corresponding to the 4.9 fb^{-1} of pp collision data at $\sqrt{s} = 7$ TeV and 19.5 fb^{-1} at $\sqrt{s} = 8$ TeV. In order to study the detector response, estimate backgrounds and to model systematic effects several MC simulations were used. The grand sample of $12 \cdot 10^6$ $B_s^0 \to J/\psi\phi$ and $1 \cdot 10^6$ of $B_s^0\pi^\pm$ events were generated using Pythia 8.18 tuned with ATLAS data.

In order to select $B_s^0\pi^\pm$ candidate, events collected with di-muon triggers were used, which are based on the $J/\psi \to \mu^+\mu^-$ identification with p_{T} threshold of either 4 or 6 GeV.

10.1.1 The $B_s^0 \to J/\psi\phi$ Candidate Selection

The reconstruction of $B_s^0 \to J/\psi\phi$ candidates is adapted from the CP-violation measurement and was previously described in section 8.2. In addition to the selection cuts described in section 8.2, the B_s^0 candidate is required to pass following criteria:

- the event must contain at least one reconstructed PV formed from at least six ID tracks.

- $t > 0.2\,\text{ps}$, to reduce the background from the events with a J/ψ produced directly in pp collision

Only the best χ^2 candidates are taken for further analysis. The invariant mass of selected $B_s^0 \to J/\psi\phi$ candidates can be seen in Figure 10.2.

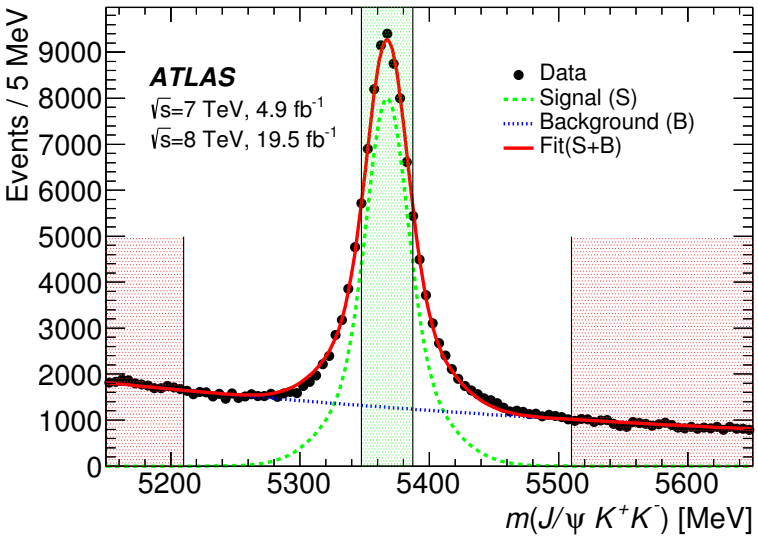

Figure 10.2: The invariant mass distribution for $B_s^0 \to J/\psi\phi$ candidates satisfying the selection criteria. Data are shown as points and results of fits to signal (dashed), background (dotted), and the total fit (solid) are shown as lines. The two outer (red) shaded bands and the central (green) shaded band represent the mass sidebands and the signal region of B_s^0 meson candidates, respectively.

10.1.2 The $B_s^0\pi^\pm$ Candidate Selection

To form the $B_s^0\pi^\pm$ candidate, only B_s^0 events with a reconstructed mass in the signal region of 5346.6–5386.6 MeV are used as can be seen in Figure 10.2. The $B_s^0\pi^\pm$ candidate is constructed by combining each of the tracks forming the PV with the selected B_s^0 candidate. Tracks that were already used to reconstruct the B_s^0 candidate and tracks identified as leptons (e or μ) are excluded. To maximize the $B_s^0\pi^\pm$ signal-to-background ratio, only tracks with transverse momentum $p_\text{T} > 500\,\text{MeV}$ are selected. All candidates are selected for the analysis, where the average number of combinations per event is about 1.8. The effect of so called self-background was tested on the MC sample.

10.2 Fit to Data

In order to reduce the systematic shifts in the invariant mass spectrum, the per-candidate observable $m(B_s^0\pi^\pm)$ is defined as follows:

$$m(B_s^0\pi^\pm) = m(J/\psi K^+K^-\pi^\pm) - m(J/\psi K^+K^-) + m_{\rm fit}(B_s^0), \tag{10.1}$$

where $m_{\rm fit}(B_s^0) = 5366.6\,{\rm MeV}$.

10.2.1 Background PDF

The first step in the analysis was to perform the background study in a similar way that the D$\emptyset$ collaboration did and to establish the best background model using real data and MC generated sample. Based on a background study, the following PDF was used as default background model:

$$F_{\rm bck}\left(m(B_s^0\pi^\pm)\right) = \left(\frac{m(B_s^0\pi^\pm) - m_{\rm thr}}{n}\right)^a \cdot \exp\left(\sum_{i=1}^{4} p_i \cdot \left(\frac{m(B_s^0\pi^\pm) - m_{\rm thr}}{n}\right)^i\right), \tag{10.2}$$

where $m_{\rm thr} = m_{\rm fit}(B_s^0) + m_\pi$ and n, a, p_i are free parameters of the fit. The studies of the cone cut, ΔR, on the background shape were performed as can be seen in Figure 10.3; however, it was decided to not use the cone cut in the analysis to avoid fit bias.

10.2.2 Signal PDF

The Signal PDF $F_{sig}(m(B_s^0\pi^\pm))$ is defined as a convolution of the S-wave Breit–Wigner(BW) distribution with a detector resolution function which is represented by a Gaussian function with a width that is calculated individually for each $B_s^0\pi^\pm$ candidate from the tracking and vertexing error matrices. The BW parameterization is appropriate for an S-wave two-body decay near threshold:

$$F_{\rm BW}\left(m(B_s^0\pi^\pm), m_X, \Gamma_X\right) = \frac{m(B_s^0\pi^\pm)\cdot m_X \cdot \Gamma\left(m(B_s^0\pi^\pm), \Gamma_X\right)}{\left(m_X^2 - m^2(B_s^0\pi^\pm)\right)^2 + m_X^2\cdot\Gamma^2\left(m(B_s^0\pi^\pm), \Gamma_X\right)}, \tag{10.3}$$

where m_X and Γ_X are the mass and the natural width of the resonance and the mass-dependent width is defined as follows:

$$\Gamma\left(m(B_s^0\pi^\pm), \Gamma_X\right) = \Gamma_X \cdot (q_1/q_0), \tag{10.4}$$

where q_1 and q_0 are the magnitudes of the three-vector momenta of the B_s^0 meson in the rest frame of the $B_s^0\pi^\pm$ system at the invariant masses equal to $m(B_s^0\pi^\pm)$ and m_X,

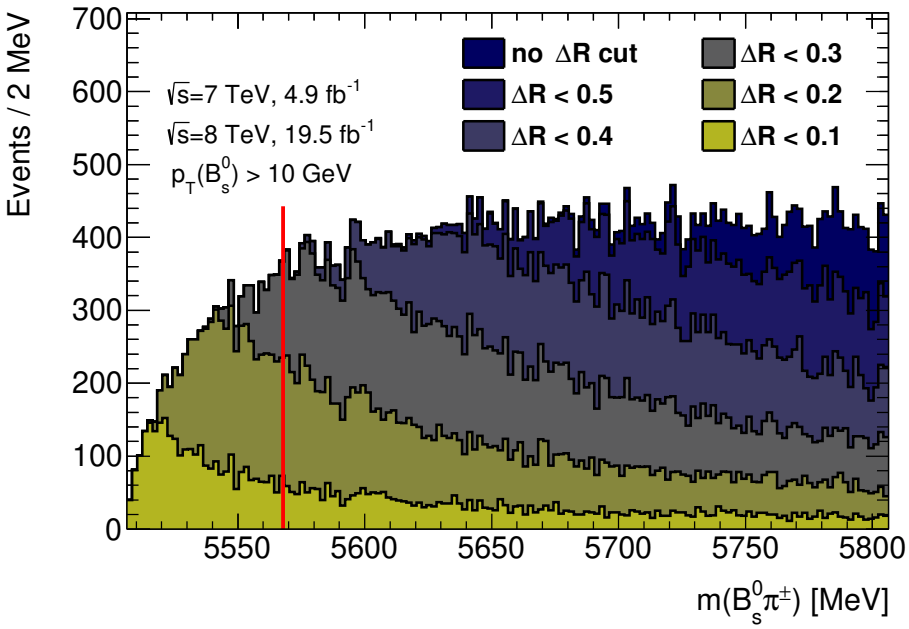

Figure 10.3: The study of the background shape behavior under the cut on ΔR parameter. The red line represents the central invariant mass value of the resonance X(5568) reported by the DØ collaboration.

respectively. The signal mass and width are fixed to the central values reported by the DØ collaboration, $m_X = 5567.8\,\text{MeV}$ and $\Gamma_X = 21.9\,\text{MeV}$.

10.2.3 Unbinned Maximum Likelihood Fit

In order to extract physics parameters, the unbinned maximum-likelihood fit with a per-candidate error was used. The total model is given as

$$F\left(m(B_s^0\pi^\pm)\right) = N(X)\cdot F_{\text{sig}}\left(m(B_s^0\pi^\pm)\right) + (N_{\text{can}} - N(X))\cdot F_{\text{bck}}\left(m(B_s^0\pi^\pm)\right)\ , \quad (10.5)$$

where $N(X)$ is the number of signal events and N_{can} is the number of all selected $B_s^0\pi^\pm$ candidates. The results of the fits are shown in Figure 10.4 for two sets of $B_s^0\pi^\pm$ candidates, the first with $p_{\text{T}} > 10\,\text{GeV}$ and the second with $p_{\text{T}} > 15\,\text{GeV}$.

The extracted values for the number of $B_s^0\pi^\pm$ candidates is $N(X) = 60 \pm 140$ for ($p_{\text{T}} > 10$ GeV) and $N(X) = -30 \pm 150$ for ($p_{\text{T}} > 15$ GeV) and no significant X(5568) signal was observed. Additional selections such as cuts on the angle between the momenta of the B_s^0 and $\pi^\pm$ candidates were investigated and did not produce evidence of a signal.

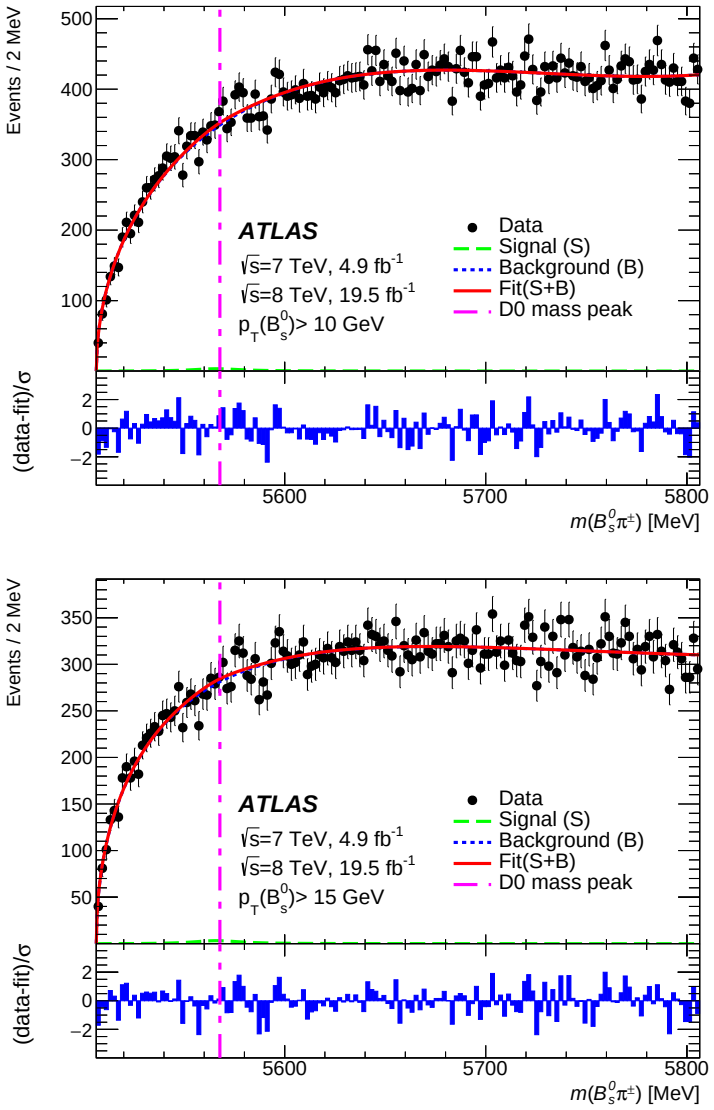

Figure 10.4: Results of the fit to the $B_s^0\pi^\pm$ mass distribution for candidates with $p_{\mathrm{T}}(B_s^0) > 10\,\mathrm{GeV}$ (top) $p_{\mathrm{T}}(B_s^0) > 15\,\mathrm{GeV}$ and (bottom). The bottom panels show the difference between each data point and the fit divided by the statistical uncertainty of that point [110].

10.3 Setting Upper Limits

Since no significant signal corresponding to the stated properties of the X(5568) as reported by Ref.[105] is observed, upper limits are determined for the number of $B_s^0\pi^\pm$ signal events, N(X), and for the relative production rate ρ_X of the $B_s^0\pi^\pm$ and B_s^0. The relative production

rate within the ATLAS acceptance is defined as follows:

$$\rho_X \equiv \frac{\sigma(pp \to X + \text{anything}) \times \mathcal{B}(X \to B_s^0\pi^\pm)}{\sigma(pp \to B_s^0 + \text{anything})} = \frac{N(X)}{N(B_s^0)} \times \frac{1}{\epsilon^{\text{rel}}(X)}, \tag{10.6}$$

where the σ are the cross-sections related to the produced particles (resonance X or meson B_s^0) within the ATLAS acceptance, $N(X)$ and $N(B_s^0)$ are the yields obtained from the fits to invariant mass distributions and $\epsilon^{\text{rel}}(X) = \frac{\epsilon(X)}{\epsilon(B_s^0)}$ is a relative efficiency of the $B_s^0\pi^\pm$ state X and the B_s^0 meson. Since B_s efficiency cancels, the ϵ^{rel} accounts for the reconstruction and selection efficiencies of the companion pion including the soft pion acceptance.

The relative efficiency, ϵ_{rel}, has been determined using MC simulation of $B_s^0\pi^\pm$ and B_s^0 events. The ϵ_{rel} consist of two effects, the detector reconstruction efficiency of a companion pion, ϵ_{det}, and the additional contributing factor, ϵ_0, correcting for pions under the p_{T} reconstruction threshold, 500 MeV. To account for the pions below the threshold, the generator level MC was used. The ϵ_{det} and ϵ_0 has been parametrized as a function of $p_{\text{T}}(B_s^0)$. To account for the dependence on $B_s^0\pi^\pm$ invariant mass, the ϵ_{det} and ϵ_0 was divided in several intervals. For ϵ_0 six intervals are used: 5550–5560 MeV, 5560–5575 MeV , 5575–5620 MeV, 5620–5650 MeV, 5650–5670 MeV and 5670–5750 MeV. For ϵ_{det} four intervals were sufficient: 5550–5560 MeV, 5560–5575 MeV , 5575–5600 MeV and 5600–5750 MeV. Due to rapidity dependence of the ϵ_{rel}, the correction factor were built separately for barrel and end-cap regions. The proper parametrization of the ϵ_{rel} is crucial to calculate the upper limits correctly.

10.3.1 CLs Limits Estimation

The upper limit is calculated using the asymptotic approximation from the profile likelihood formalism based on the CL_s frequentist method. The systematic uncertainties are included in the method and systematics effects on $N(X)$ accounts for:

- uncertainties of D∅ measurement of m_X and Γ_X, since these parameters are fixed in the fit
- the background model, estimated by replacing the default model by a seventh-order Chebyshev polynomial
- the signal model of the X resonance, where the default model that assumes X to have no spin is exchanged by a BW P-wave resonance form
- the detector resolution with the default per-candidate mass resolution model replaced by the sum of three Gaussian functions with a common mean

The extracted upper limits at 95% CL are $N(X) < 382$ for $p_{\mathrm{T}}(B_s^0) > 10\,\mathrm{GeV}$ and $N(X) < 356$ for $p_{\mathrm{T}}(B_s^0) > 15\,\mathrm{GeV}$.

To extract the upper limits on ρ_X, the same systematic effects are included with two additional contributions which account for ϵ^{rel} and $N(B_s^0)$ uncertainties. These are included into CL_s method as additional Gaussian constraints. The resulting upper limits at 95% CL are $\rho_X < 0.015$ for $p_{\mathrm{T}}(B_s^0) > 10\,\mathrm{GeV}$ and $\rho_X < 0.016$ for $p_{\mathrm{T}}(B_s^0) > 15\,\mathrm{GeV}$.

A hypothesis test is performed for the presence of a $B_s^0\pi^\pm$ peak for every 5 MeV step in its mass from 5550 to 5700 MeV, with assumption of resonant state described by S-wave BW distribution with BW width of 21.9 MeV and $p_{\mathrm{T}}(B_s^0) > 10\,\mathrm{GeV}$. The mass dependence of resolution and ϵ^{rel} function is included as well as all systematics effects except X(5568) mass uncertainty. The results are shown in Figure 10.5 and are within $\pm 1\,\sigma$ of the background only model.

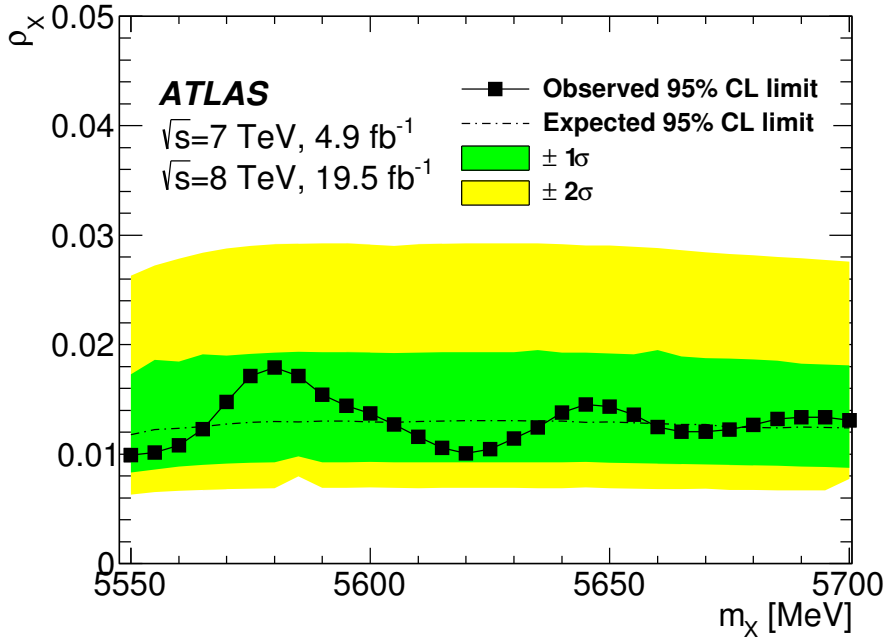

Figure 10.5: Upper limits on ρ_X at 95% CL (black squares connected by line) at different masses of a hypothetical resonant state X decaying to $B_s^0\pi^\pm$, for events with $p_{\mathrm{T}}(B_s^0) > 10\,\mathrm{GeV}$. The values include systematic uncertainties. The expected (central black dot-dashed line) 95% CL upper limits with $\pm 1\,\sigma$ (green) and $\pm 2\,\sigma$ (yellow) uncertainty bands on ρ_X are shown as functions of the $B_s^0\pi^\pm$ mass [110].

10.4 Summary

A search for a new state X(5568) decaying to $B_s^0\pi^\pm$, as reported by the DØ collaboration, was performed by ATLAS, using 4.9 fb^{-1} of pp collision data at 7 TeV and 19.5 fb^{-1} at 8 TeV. No significant signal was found, within the analysis acceptance. The upper limits on the number of signal events $N(X)$ and on its production rate relative to B_s^0 mesons were measured. The published upper limits at 95% CL are $N(X) < 382$ and $\rho_X < 0.015$ for $p_{\text{T}}(B_s^0) > 10\,\text{GeV}$ and $N(X) < 356$ and $\rho_X < 0.016$ for $p_{\text{T}}(B_s^0) > 15\,\text{GeV}$. The hypothesis test for X(5568) state was performed and across the full range is consistent with background only model.

The comparison of measured upper limits on the relative production rate with other LHC experiments can be seen in Table 10.1. The LHCb measured the upper limits using three different cuts on while the CMS used the same binning as ATLAS.

	95 % CL of ρ_X		
	$p_{\text{T}}(B_s^0) > 5\,\text{GeV}$	$p_{\text{T}}(B_s^0) > 10\,\text{GeV}$	$p_{\text{T}}(B_s^0) > 15\,\text{GeV}$
ATLAS		0.015	0.016
CMS		0.011	0.010
LHCb	0.012	0.024	0.020

Table 10.1: Comparison of the 95 % CL Limits on relative production rate ρ_X between LHC experiments.

This measurement was a useful test of the sensitivity of the ATLAS detector, because the other LHC experiments were performing same measurements. The ATLAS proved its capability to preform such search and provide consistent results with other experiments.

CHAPTER 11

Conclusions

This thesis presents the measurement of the time-dependent CP-violation parameters in the $B_s^0 \to J/\psi(\mu^+\mu^-)\phi(K^+K^-)$ decays. The measurement of the CP-violation phase ϕ_s provides the possibility to test the predictions of the Standard Model of particle physics and in case of any deviation it would indicate that there could be other sources of CP-violation beyond the Standard Model. Two additional benchmark analyses were performed in order to validate the quality and precision of the data collected by the B-Physics triggers and the ATLAS detector. These benchmark analyses were performing the lifetime measurement of B_d^0 and $B^\pm$ decays and searching for structure in $B_s^0\pi^\pm$ invariant mass spectrum. All three analyses are based on the pp collisions data collected by the ATLAS detector at the LHC accelerator. Following paragraphs will summarize the results obtained from the performed measurements.

CP-Violation in the $B_s^0 \to J/\psi\phi$ Decay

The measurement of CP-violation parameters in $B_s^0 \to J/\psi(\mu^+\mu^-)\phi(K^+K^-)$ decay was performed on the data sample of pp collisions at 13 TeV with integrated luminosity of $80.5\,\text{fb}^{-1}$. In order to describe the $B_s^0 \to J/\psi(\mu^+\mu^-)\phi(K^+K^-)$ system, a time-dependent angular analysis of the final state particles was performed. The nine physical parameters describing the CP-violation in $B_s^0 \to J/\psi(\mu^+\mu^-)\phi(K^+K^-)$ system are extracted from the unbinned maximum likelihood fit. The large variety of systematic effects was studied and used for the systematic uncertainty evaluation. The obtained results were statistically combined with those from a previous ATLAS analysis based on Run 1 data collected at $\sqrt{s} = 7\,\text{TeV}$ and 8 TeV with integrated luminosity of $19.2\,\text{fb}^{-1}$ [91]. The final values of the combined parameters are:

$$
\begin{aligned}
\phi_s &= -0.087 \pm 0.037\,(\text{stat.}) \pm 0.019\,(\text{syst.})\,\text{rad} \\
\Delta\Gamma_s &= 0.064 \pm 0.004\,(\text{stat.}) \pm 0.002\,(\text{syst.})\,\text{ps}^{-1} \\
\Gamma_s &= 0.670 \pm 0.001\,(\text{stat.}) \pm 0.002\,(\text{syst.})\,\text{ps}^{-1} \\
|A_\parallel(0)|^2 &= 0.222 \pm 0.002\,(\text{stat.}) \pm 0.002\,(\text{syst.}) \\
|A_0(0)|^2 &= 0.515 \pm 0.001\,(\text{stat.}) \pm 0.003\,(\text{syst.}) \\
|A_S(0)|^2 &= 0.034 \pm 0.003\,(\text{stat.}) \pm 0.004\,(\text{syst.}) \\
\delta_\perp &= 3.213 \pm 0.102\,(\text{stat.}) \pm 0.049\,(\text{syst.})\,\text{rad} \\
\delta_\parallel &= 3.356 \pm 0.050\,(\text{stat.}) \pm 0.079\,(\text{syst.})\,\text{rad} \\
\delta_\perp - \delta_S &= -0.244 \pm 0.046\,(\text{stat.}) \pm 0.018\,(\text{syst.})\,\text{rad}
\end{aligned}
$$

and were submitted to the EPJC journal as [35]. These results are consistent with other LHC experiments as well as with the theoretical predictions for the SM. These new ATLAS result provide increased precision of the CP-violating phase ϕ and in combination with other measurements provide tighter constraints for the contribution from any BSM processes. The combined results from all measurements are shown in Figure 11.1.

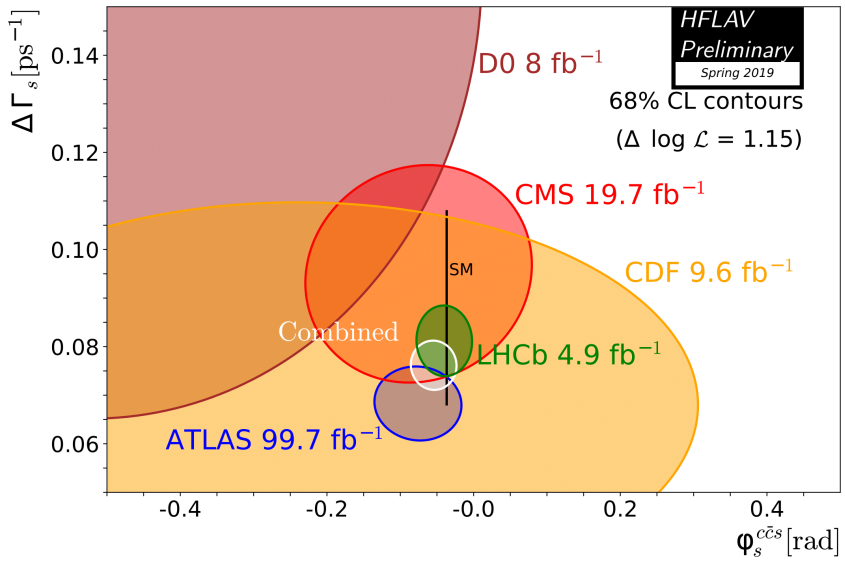

Figure 11.1: 68% CL contours in the (ϕ_s, $\Delta\Gamma_s$) plane, showing the measurements from CDF, DØ, ATLAS, CMS and LHCb along with their combination. The thin black rectangle represents the Standard Model predictions of ϕ_s and $\Delta\Gamma_s$ [37].

The analysis using full the Run 2 dataset with integrated luminosity of 139 fb^{-1} is ongoing and will provide even more precise result on the CP-violating phase ϕ and in addition a more complex model with two additional free physics parameters will be used.

Lifetime Measurement of the B_d^0 and $B^\pm$ Decay

The performance of the B-Physics triggers and reconstruction algorithms was validated by measuring the invariant mass and lifetime in the $B^\pm \to J/\psi K^\pm$ and $B_d^0 \to J/\psi K^{*0}$ channels using data from pp collisions at 13 TeV with integrated luminosity of $80.5\,\text{fb}^{-1}$. The measured properties were extracted using the unbinned maximum likelihood fit using similar approach as for the CP-violation measurement. The obtained results show stability within the data taking periods for a variety of triggers. The effect of lifetime correction was studied using full statistics. The fitted lifetimes can compete with current most precise measurements within statistical uncertainty; however, for the complete measurement, the systematic uncertainty needs to be evaluated. It is expected that systematic uncertainty will be dominant in this measurement. In order to reduce large systematic uncertainties, a more complex model need to be introduced.

Search for a Structure in the $B_s^0\pi^\pm$ Invariant Mass Spectrum

The final benchmark measurement was devoted to the search for resonance $X(5568)$ in the $B_s^0\pi^\pm$ invariant mass spectrum which was reported by the D$\emptyset$ collaboration. The analysis was performed on the pp collisions data from ATLAS Run 1 containing 4.9 fb^{-1} of $\sqrt{s} = 7$ TeV and 19.5 fb^{-1} of $\sqrt{s} = 8$ TeV datasets. No significant evidence for the $X(5568)$ resonance was found within the ATLAS analysis acceptance which is consistent with other LHC experiments.

The 95% CL limits of the number of signal events $N(X)$ and of its production rate relative to B_s^0 mesons ρ_X were measured and are competitive with other LHC measurements. The hypothesis test for $X(5568)$ state was performed across the full invariant mass range and in all measured points it is consistent with background only model within one sigma band.

Bibliography

[1] Lyndon Evans and Philip Bryant, *LHC Machine*, JINST **3** (2008) S08001.

[2] *The ATLAS Experiment at the CERN Large Hadron Collider*, JINST **3** (2008) S08003.

[3] Georges Aad et al., *Observation of a new particle in the search for the Standard Model Higgs boson with the ATLAS detector at the LHC*, Phys. Lett. B **716** (2012) 1, arXiv: 1207.7214 [hep-ex].

[4] M. Tanabashi et al., *Review of Particle Physics*, Phys. Rev. D **98** (2018) 030001.

[5] R.P. Feynman, *QED: The Strange Theory of Light and Matter*, 1986, ISBN: 978-0-691-02417-2.

[6] D. V. Ahluwalia, *Book Review: The Quantum Theory of Fields, Vol. I and II by S. Weinberg*, (1997), arXiv: physics/9704002 [physics.pop-ph].

[7] Murray Gell-Mann, *The Eightfold Way: A Theory of strong interaction symmetry*, (1961).

[8] G. Zweig, "An SU(3) model for strong interaction symmetry and its breaking. Version 2", *DEVELOPMENTS IN THE QUARK THEORY OF HADRONS. VOL. 1. 1964 - 1978*, ed. by D.B. Lichtenberg and Simon Peter Rosen, 1964 22.

[9] Donald H. Perkins, *Introduction to high energy physics*, vol. 2, Addison-Wesley Reading, Massachusetts, 1987.

[10] Elena Giusarma, Roland de Putter, Shirley Ho, and Olga Mena, *Constraints on neutrino masses from Planck and Galaxy Clustering data*, Phys. Rev. D **88** (2013) 063515, arXiv: 1306.5544 [astro-ph.CO].

[11] Ubaldo Dore and Lucia Zanello, *Bruno Pontecorvo and neutrino physics*, (2009), arXiv: 0910.1657 [physics.hist-ph].

[12] Y. Fukuda et al., *Evidence for oscillation of atmospheric neutrinos*, Phys. Rev. Lett. **81** (1998) 1562, arXiv: hep-ex/9807003.

[13] Noether, E, *Invariante Variationsprobleme. Königlich Gesellschaft der Wissenschaften Göttingen Nachrichten Mathematik-Physik Klasse*, 1918.

[14] J. H. Christenson, J. W. Cronin, V. L. Fitch, and R. Turlay, *Evidence for the 2π Decay of the K_2^0 Meson*, Phys. Rev. Lett. **13** (1964) 138.

[15] Samoil M. Bilenky and J. Hosek, *Glashow-Weinberg-Salam Theory of Electroweak Interactions and the Neutral Currents*, Phys. Rept. **90** (1982) 73.

[16] Peter W. Higgs, *Broken Symmetries and the Masses of Gauge Bosons*, Phys. Rev. Lett. **13** (1964) 508, ed. by J.C. Taylor.

[17] F. Englert and R. Brout, *Broken Symmetry and the Mass of Gauge Vector Mesons*, Phys. Rev. Lett. **13** (1964) 321, ed. by J.C. Taylor.

[18] Nicola Cabibbo, *Unitary Symmetry and Leptonic Decays*, Phys. Rev. Lett. **10** (1963) 531.

[19] Makoto Kobayashi and Toshihide Maskawa, *CP Violation in the Renormalizable Theory of Weak Interaction*, Prog. Theor. Phys. **49** (1973) 652.

[20] Lincoln Wolfenstein, *Parametrization of the Kobayashi-Maskawa Matrix*, Phys. Rev. Lett. **51** (1983) 1945.

[21] C. Jarlskog, *Commutator of the Quark Mass Matrices in the Standard Electroweak Model and a Measure of Maximal CP Violation*, Phys. Rev. Lett. **55** (1985) 1039.

[22] *Homepage of the CKMfitter collaboration*, `http://ckmfitter.in2p3.fr`, Accessed: 2020-04-14.

[23] W. Pauli, *Über den Zusammenhang des Abschlusses der Elektronengruppen im Atom mit der Komplexstruktur der Spektren*, Zeitschrift für Physik **31** (1925) 765.

[24] Felix Siebenhühner, *Determination of the QCD coupling constant from charmonium*, `http://theorie.ikp.physik.tu-darmstadt.de/nhc/pages/lectures/rhiseminar07-08/siebenhuehner.pdf`, Accessed: 2020-04-14.

[25] E. Eichten, K. Gottfried, T. Kinoshita, K.D. Lane, and Tung-Mow Yan, *Charmonium: The Model*, Phys. Rev. D **17** (1978) 3090, [Erratum: Phys.Rev.D 21, 313 (1980)].

[26] Taichi Kawanai and Shoichi Sasaki, *Heavy quarkonium potential from Bethe-Salpeter wave function on the lattice*, Phys.Rev. **D89** (2014) 054507, arXiv: `1311.1253 [hep-lat]`.

[27] Ulrich Nierste, "Three Lectures on Meson Mixing and CKM phenomenology", *Helmholz International Summer School on Heavy Quark Physics*, 2009 1, arXiv: `0904.1869 [hep-ph]`.

[28] K. Anikeev et al., "B physics at the Tevatron: Run II and beyond", *Workshop on B Physics at the Tevatron: Run II and Beyond*, 2001, arXiv: hep-ph/0201071.

[29] Joao P. Silva, "Phenomenological aspects of CP violation", *Central European School in Particle Physics*, 2004, arXiv: hep-ph/0410351.

[30] Marina Artuso, Guennadi Borissov, and Alexander Lenz, *CP violation in the B_s^0 system*, Rev. Mod. Phys. **88** (2016) 045002, [Addendum: Rev.Mod.Phys. 91, 049901 (2019)], arXiv: 1511.09466 [hep-ph].

[31] H.T. Edwards, *The Tevatron Energy Doubler: A Superconducting Accelerator*, Ann. Rev. Nucl. Part. Sci. **35** (1985) 605.

[32] T. Aaltonen et al., *Measurement of the Bottom-Strange Meson Mixing Phase in the Full CDF Data Set*, Phys. Rev. Lett. **109** (2012) 171802, arXiv: 1208.2967 [hep-ex].

[33] D0 Collaboration, *Measurement of the CP-violating phase $\phi_s^{J/\psi\phi}$ using the flavor-tagged decay $B_s^0 \to J/\psi\phi$ in 8 fb^{-1} of $p\bar{p}$ collisions*, Phys. Rev. D **85** (2012) 032006, arXiv: 1109.3166 [hep-ex].

[34] CMS Collaboration, *Measurement of the CP-violating weak phase ϕ_s and the decay width difference $\Delta\Gamma_s$ using the $B_s^0 \to J/\psi\phi(1020)$ decay channel in pp collisions at $\sqrt{s} = 8$ TeV*, Phys. Lett. B **757** (2016) 97, arXiv: 1507.07527 [hep-ex].

[35] Georges Aad et al., *Measurement of the CP-violating phase ϕ_s in $B_s^0 \to J/\psi\phi$ decays in ATLAS at 13 TeV*, (2020), arXiv: 2001.07115 [hep-ex].

[36] LHCb Collaboration, *Updated measurement of time-dependent CP-violating observables in $B_s^0 \to J/\psi K^+K^-$ decays*, Eur. Phys. J. **C79** (2019) 706, arXiv: 1906.08356 [hep-ex].

[37] J.B. Zonneveld, *Search for CP violation in B_s^0 mixing at LHCb*, (2019), arXiv: 1905.02559 [hep-ex].

[38] Accelerators and Technology Sector, *The CERN accelerator complex*, https://espace.cern.ch/acc-tec-sector/default.aspx, Accessed: 2020-04-14.

[39] CERN, *The accelerator complex*, http://home.web.cern.ch/about/accelerators, Accessed: 2020-04-14.

[40] ATLAS Collaboration, *ATLAS Luminosity Public Results in Run 2*, https://twiki.cern.ch/twiki/bin/view/AtlasPublic/LuminosityPublicResultsRun2, Accessed: 2020-03-21.

[41] T. Pieloni et al., "Colliding High Brightness Beams in the LHC", *52nd ICFA Advanced Beam Dynamics Workshop on High-Intensity and High-Brightness Hadron Beams*, 2012 MOP250.

[42] Jorg Wenninger, "Approaching the Nominal Performance at the LHC", *8th International Particle Accelerator Conference*, 2017 MOYAA1.

[43] R. Bruce et al., "Baseline LHC machine parameters and configuration of the 2015 proton run", *Proceedings, LHC Performance Workshop (Chamonix 2014)*, 2015 100, arXiv: 1410.5990 [physics.acc-ph].

[44] Rende Steerenberg et al., "Operation and performance of the CERN Large Hadron Collider during proton Run 2", *10th International Particle Accelerator Conference*, 2019 MOPMP031.

[45] A. Yamamoto et al., *The ATLAS central solenoid*, Nucl. Instrum. Meth. A **584** (2008) 53.

[46] Zlobin, A. V. 2014. Superconducting Magnets - Principles, Operation, and Applications. Wiley Encyclopedia of Electrical and Electronics Engineering. 1–19.

[47] M. Aleksa et al., *Measurement of the ATLAS solenoid magnetic field*, JINST **3** (2008) P04003.

[48] Paolo Sabatini, *Operational experience and performance with the ATLAS Pixel detector at the Large Hadron Collider at CERN*, JINST **15** (2020) C02039, ed. by Marzio Nessi.

[49] ATLAS Collaboration, *Impact Parameter Resolution after IBL upgrade*, https://atlas.web.cern.ch/Atlas/GROUPS/PHYSICS/PLOTS/IDTR-2015-007/, Accessed: 2020-03-21.

[50] ATLAS Collaboration, *B_s^0 proper decay time resolution for Run-1, Run-2 and HL-LHC*, https://atlas.web.cern.ch/Atlas/GROUPS/PHYSICS/PLOTS/BPHYS-2016-001/index.html, Accessed: 2020-03-21.

[51] ATLAS Collaboration, *The ATLAS luminosity measurement taskforce*, http://project-atlas-lucid.web.cern.ch/project-atlas-lucid/taskforce/main.html, Accessed: 2020-03-21.

[52] Georges Aad et al., *Luminosity Determination in pp Collisions at $\sqrt{s} = 7$ TeV Using the ATLAS Detector at the LHC*, Eur. Phys. J. C **71** (2011) 1630, arXiv: 1101.2185 [hep-ex].

[53] G. Avoni et al., *The new LUCID-2 detector for luminosity measurement and monitoring in ATLAS*, JINST **13** (2018) P07017.

[54] Marco A.L. Leite, "Performance of the ATLAS Zero Degree Calorimeter", *2013 IEEE Nuclear Science Symposium and Medical Imaging Conference and Workshop on Room-Temperature Semiconductor Detectors*, 2013.

[55] Georges Aad et al., *Measurement of the total cross section from elastic scattering in pp collisions at $\sqrt{s} = 7$ TeV with the ATLAS detector*, Nucl. Phys. **B889** (2014) 486, arXiv: 1408.5778 [hep-ex].

[56] *The ATLAS luminosity measurement taskforce*, http://lunvis.web.cern.ch/lunvis/taskforce/main.html, Accessed: 2020-04-14.

[57] *Athena The ATLAS Common Framework*, http://atlas-computing.web.cern.ch/atlas-computing/documentation/swDoc/AthenaDeveloperGuide-8.0.0-draft.pdf, Accessed: 2020-04-14.

[58] Rene Brun and Fons Rademakers, *An Object Oriented Data Analysis Framework*, ftp://root.cern.ch/root/laussanne.ps.gz, Accessed: 2020-04-14.

[59] Wouter Verkerke and David Kirkby, *The RooFit toolkit for data modeling*, 2003, arXiv: physics/0306116 [physics.data-an].

[60] David Adams et al., *Dual-use tools and systematics-aware analysis workflows in the ATLAS Run-2 analysis model*, J. Phys. Conf. Ser. **664** (2015) 032007.

[61] Torbjorn Sjöstrand, Stephen Mrenna, and Peter Z. Skands, *A Brief Introduction to PYTHIA 8.1*, Comput.Phys.Commun. **178** (2008) 852, arXiv: 0710.3820 [hep-ph].

[62] M Smizanska, *PythiaB an interface to Pythia6 dedicated to simulation of beauty events*, tech. rep. ATL-COM-PHYS-2003-038, CERN, 2003.

[63] S. Agostinelli et al., *GEANT4 – a simulation toolkit*, Nucl. Instrum. Meth. A **506** (2003) 250.

[64] Moritz Backes, *The ATLAS Trigger System: Ready for Run-2*, PoS **LeptonPhoton2015** (2016) 045.

[65] *Trigger Operation Public Results*, https://twiki.cern.ch/twiki/bin/view/AtlasPublic/TriggerOperationPublicResults, Accessed: 2020-04-14.

[66] ATLAS Collaboration, *2015 start-up trigger menu and initial performance assessment of the ATLAS trigger using Run-2 data*, tech. rep. ATL-DAQ-PUB-2016-001, CERN, 2016, URL: https://cds.cern.ch/record/2136007.

[67] *B Physics Trigger Public Results*, https://twiki.cern.ch/twiki/bin/view/AtlasPublic/BPhysicsTriggerPublicResults, Accessed: 2020-04-14.

[68] Georges Aad et al., *Probing lepton flavour violation via neutrinoless $\tau \longrightarrow 3\mu$ decays with the ATLAS detector*, Eur. Phys. J. C **76** (2016) 232, arXiv: 1601.03567 [hep-ex].

[69] Morad Aaboud et al., *Study of the rare decays of B_s^0 and B^0 mesons into muon pairs using data collected during 2015 and 2016 with the ATLAS detector*, JHEP **04** (2019) 098, arXiv: 1812.03017 [hep-ex].

[70] F. Abe et al., *Observation of the B_c meson in $p\bar{p}$ collisions at $\sqrt{s} = 1.8$ TeV*, Phys. Rev. Lett. **81** (1998) 2432, arXiv: hep-ex/9805034 [hep-ex].

[71] Georges Aad et al., *Observation of an Excited $B_c^{\pm}$ Meson State with the ATLAS Detector*, Phys. Rev. Lett. **113** (2014) 212004, arXiv: 1407.1032 [hep-ex].

[72] Albert M Sirunyan et al., *Observation of Two Excited B_c^+ States and Measurement of the $B_c^+(2S)$ Mass in pp Collisions at $\sqrt{s} = 13$ TeV*, Phys. Rev. Lett. **122** (2019) 132001, arXiv: 1902.00571 [hep-ex].

[73] Roel Aaij et al., *Search for excited B_c^+ states*, JHEP **01** (2018) 138, arXiv: 1712.04094 [hep-ex].

[74] R. Aaij et al., *Measurement of the $B^{\pm}$ production cross-section in pp collisions at $\sqrt{s} = 7$ TeV*, JHEP **04** (2012) 093, arXiv: 1202.4812 [hep-ex].

[75] Roel Aaij et al., *Measurements of the B^+, B^0, B_s^0 meson and Λ_b^0 baryon lifetimes*, JHEP **04** (2014) 114, arXiv: 1402.2554 [hep-ex].

[76] Georges Aad et al., *Muon reconstruction performance of the ATLAS detector in proton–proton collision data at $\sqrt{s}$ =13 TeV*, Eur. Phys. J. C **76** (2016) 292, arXiv: 1603.05598 [hep-ex].

[77] *Homepage of the MINUIT*, https://seal.web.cern.ch/seal/snapshot/work-packages/mathlibs/minuit/, Accessed: 2020-04-14.

[78] G. Cowan, *Statistical Data Analysis*, Oxford science publications, Clarendon Press, 1998, ISBN: 9780198501558.

[79] LHCb Collaboration, *Updated average f_s/f_d b-hadron production fraction ratio for 7 TeV pp collisions*, LHCb-CONF-2013-011, 2013, URL: https://cds.cern.ch/record/1559262.

[80] LHCb Collaboration, *Study of the kinematic dependences of Λ_b^0 production in pp collisions and a measurement of the $\Lambda_b^0 \to \Lambda_c^+ \pi^-$ branching fraction*, JHEP **08** (2014) 143, arXiv: 1405.6842 [hep-ex].

[81] LHCb Collaboration, *Study of the production of Λ_b^0 and $\overline{B}^0$ hadrons in pp collisions and first measurement of the $\Lambda_b^0 \to J/\psi p K^-$ branching fraction*, Chin. Phys. C **40** (2016) 011001, arXiv: 1509.00292 [hep-ex].

[82] LHCb Collaboration, *Observation of $J/\psi p$ Resonances Consistent with Pentaquark States in $\Lambda_b^0 \to J/\psi K^- p$ Decays*, Phys. Rev. Lett. **115** (2015) 072001, arXiv: 1507.03414 [hep-ex].

[83] Bernard Aubert et al., *Search for the Z(4430)- at BABAR*, Phys. Rev. D **79** (2009) 112001, arXiv: 0811.0564 [hep-ex].

[84] Roel Aaij et al., *Observation of $J/\psi p$ Resonances Consistent with Pentaquark States in $\Lambda_b^0 \to J/\psi K^- p$ Decays*, Phys. Rev. Lett. **115** (2015) 072001, arXiv: 1507.03414 [hep-ex].

[85] R Aaij et al., *Measurement of the polarization amplitudes in $B^0 \to J/\psi K^*(892)^0$ decays*, Phys. Rev. D **88** (2013) 052002, arXiv: 1307.2782 [hep-ex].

[86] Georges Aad et al., *Electron and photon performance measurements with the ATLAS detector using the 2015–2017 LHC proton-proton collision data*, JINST **14** (2019) P12006, arXiv: 1908.00005 [hep-ex].

[87] ATLAS Collaboration, *Topological cell clustering in the ATLAS calorimeters and its performance in LHC Run 1*, Eur. Phys. J. C **77** (2017) 490, arXiv: 1603.02934 [hep-ex].

[88] Matteo Cacciari, Gavin P. Salam, and Gregory Soyez, *The anti-k_t jet clustering algorithm*, JHEP **04** (2008) 063, arXiv: 0802.1189 [hep-ph].

[89] Matteo Cacciari, Gavin P. Salam, and Gregory Soyez, *FastJet user manual*, Eur. Phys. J. C **72** (2012) 1896, arXiv: 1111.6097 [hep-ph].

[90] Georges Aad et al., *ATLAS b-jet identification performance and efficiency measurement with $t\bar{t}$ events in pp collisions at $\sqrt{s} = 13$ TeV*, Eur. Phys. J. C **79** (2019) 970, arXiv: 1907.05120 [hep-ex].

[91] ATLAS Collaboration, *Measurement of the CP-violating phase ϕ_s and the B_s^0 meson decay width difference with $B_s^0 \to J/\psi\phi$ decays in ATLAS*, JHEP **08** (2016) 147, arXiv: 1601.03297 [hep-ex].

[92] Louis Lyons, Duncan Gibaut, and Peter Clifford, *How to Combine Correlated Estimates of a Single Physical Quantity*, Nucl. Instrum. Meth. A **270** (1988) 110.

[93] A. Valassi, *Combining correlated measurements of several different physical quantities*, Nucl. Instrum. Meth. A **500** (2003) 391.

[94] J. Charles et al., *Current status of the Standard Model CKM fit and constraints on $\Delta F = 2$ New Physics*, Phys. Rev. **D91** (2015) 073007, arXiv: 1501.05013 [hep-ph].

[95] Alexander Lenz and Ulrich Nierste, *Numerical updates of lifetimes and mixing parameters of B mesons*, (2011), arXiv: 1102.4274 [hep-ph].

[96] *Measurement of the CP violating phase ϕ_s in the $\mathrm{B}_s \to \mathrm{J}/\psi\,\phi(1020) \to \mu^+\mu^-\,\mathrm{K}^+\mathrm{K}^-$ channel in proton-proton collisions at $\sqrt{s} = 13$ TeV*, tech. rep. CMS-PAS-BPH-20-001, CERN, 2020, URL: http://cds.cern.ch/record/2714363.

[97] LHCb Collaboration, *Observation of B_s^0-$\bar{B}_s^0$ mixing and measurement of mixing frequencies using semileptonic B decays*, Eur. Phys. J. **C73** (2013) 2655, arXiv: 1308.1302 [hep-ex].

[98] LHCb Collaboration, *Precision measurement of the B_s^0-$\bar{B}_s^0$ oscillation frequency with the decay $B_s^0 \to D_s^-\pi^+$*, New J. Phys. **15** (2013) 053021, arXiv: 1304.4741 [hep-ex].

[99] A. Abulencia et al., *Observation of $B_s^0 - \bar{B}_s^0$ Oscillations*, Phys. Rev. Lett. **97** (2006) 242003, arXiv: hep-ex/0609040.

[100] Georges Aad et al., *Flavor tagged time-dependent angular analysis of the $B_s \to J/\psi\phi$ decay and extraction of $\Delta\Gamma s$ and the weak phase ϕ_s in ATLAS*, Phys. Rev. **D90** (2014) 052007, arXiv: 1407.1796 [hep-ex].

[101] T. Aaltonen et al., *Measurement of b Hadron Lifetimes in Exclusive Decays Containing a J/ψ in p^- pbar Collisions at $\sqrt{s} = 1.96\,TeV$*, Phys. Rev. Lett. **106** (2011) 121804, arXiv: 1012.3138 [hep-ex].

[102] Albert M Sirunyan et al., *Measurement of b hadron lifetimes in pp collisions at $\sqrt{s} = 8$ TeV*, Eur. Phys. J. C **78** (2018) 457, [Erratum: Eur.Phys.J.C 78, 561 (2018)], arXiv: 1710.08949 [hep-ex].

[103] R. Aaij et al., *Effective lifetime measurements in the $B_s^0 \to K^+K^-, B^0 \to K^+\pi^-$ and $B_s^0 \to \pi^+K^-$ decays*, Phys. Lett. **B736** (2014) 446, arXiv: 1406.7204 [hep-ex].

[104] Georges Aad et al., *Measurement of the Λ_b^0 lifetime and mass in the ATLAS experiment*, Phys. Rev. **D87** (2013) 032002, arXiv: 1207.2284 [hep-ex].

[105] V. M. Abazov et al., *Evidence for a $B_s^0\pi^\pm$ state*, Phys. Rev. Lett. **117** (2016) 022003, arXiv: 1602.07588 [hep-ex].

[106] Roel Aaij et al., *Search for Structure in the $B_s^0\pi^\pm$ Invariant Mass Spectrum*, Phys. Rev. Lett. **117** (2016) 152003, [Addendum: Phys. Rev. Lett.118,no.10,109904(2017)], arXiv: 1608.00435 [hep-ex].

[107] A. M. Sirunyan et al., *Search for the X(5568) state decaying into* $\mathrm{B}_\mathrm{s}^0\pi^\pm$ *in proton-proton collisions at* $\sqrt{s} = 8$ *TeV*, Phys. Rev. Lett. **120** (2018) 202005, arXiv: 1712.06144 [hep-ex].

[108] T. Aaltonen et al., *A search for the exotic meson* $X(5568)$ *with the Collider Detector at Fermilab*, Phys. Rev. Lett. **120** (2018) 202006, arXiv: 1712.09620 [hep-ex].

[109] Victor Mukhamedovich Abazov et al., *Study of the* $X^\pm(5568)$ *state with semileptonic decays of the* B_s^0 *meson*, Phys. Rev. **D97** (2018) 092004, arXiv: 1712.10176 [hep-ex].

[110] M. Aaboud et al., *Search for a Structure in the* $B_s^0\pi^\pm$ *Invariant Mass Spectrum with the ATLAS Experiment*, Phys. Rev. Lett. **120** (2018) 202007, arXiv: 1802.01840 [hep-ex].